

**OPTICALLY ADDRESSED ULTRA-WIDEBAND
PHASED ANTENNA ARRAY**

by

Jian Bai

A dissertation submitted to the Faculty of the University of Delaware in partial fulfillment of the requirements for the degree of Doctor of Philosophy in Electrical and Computer Engineering

Summer 2014

© 2014 Jian Bai
All Rights Reserved

UMI Number: 3642295

All rights reserved

INFORMATION TO ALL USERS

The quality of this reproduction is dependent upon the quality of the copy submitted.

In the unlikely event that the author did not send a complete manuscript and there are missing pages, these will be noted. Also, if material had to be removed, a note will indicate the deletion.



UMI 3642295

Published by ProQuest LLC (2014). Copyright in the Dissertation held by the Author.

Microform Edition © ProQuest LLC.

All rights reserved. This work is protected against unauthorized copying under Title 17, United States Code



ProQuest LLC.
789 East Eisenhower Parkway
P.O. Box 1346
Ann Arbor, MI 48106 - 1346

**OPTICALLY ADDRESSED ULTRA-WIDEBAND
PHASED ANTENNA ARRAY**

by

Jian Bai

Approved: _____
Kenneth E. Barner, Ph.D.
Chair of the Department of Electrical and Computer Engineering

Approved: _____
Babatunde Ogunnaike, Ph.D.
Dean of the College of Engineering

Approved: _____
James G. Richards, Ph.D.
Vice Provost for Graduate and Professional Education

I certify that I have read this dissertation and that in my opinion it meets the academic and professional standard required by the University as a dissertation for the degree of Doctor of Philosophy.

Signed:

Dennis W. Prather, Ph.D.
Professor in charge of dissertation

I certify that I have read this dissertation and that in my opinion it meets the academic and professional standard required by the University as a dissertation for the degree of Doctor of Philosophy.

Signed:

Mark S. Mirotznik, Ph.D.
Member of dissertation committee

I certify that I have read this dissertation and that in my opinion it meets the academic and professional standard required by the University as a dissertation for the degree of Doctor of Philosophy.

Signed:

Daniel S. Weile, Ph.D.
Member of dissertation committee

I certify that I have read this dissertation and that in my opinion it meets the academic and professional standard required by the University as a dissertation for the degree of Doctor of Philosophy.

Signed:

Duixian Liu, Ph.D.
Member of dissertation committee

ACKNOWLEDGMENTS

I would like to thank Dr. Dennis Prather and his research group. Without his invaluable support, none of this work would have been possible. I appreciate his offer to join his group which has afforded me with great opportunities and exposure to a lot of cutting-edge research. I also appreciate that he provided a supportive and independent studying environment. In his group, I had a chance to let my ideas be appreciated and can always find help from my colleagues whenever I need.

I would also like to thank my wife. She is always supportive of my work, and encouraged me when I felt depressed or underwent rough times. The support from my parents and family is always one of the biggest motivations driving me to my current position.

I would like to thank separately Dr. Shouyuan Shi. He always kindly shared his great ideas with me and provided guidance in my work. His support and friendship are very much appreciated.

The group members of Dr. Prather's research group have been very supportive of my work. Discussions with them were very helpful. I appreciate their time spent training me with many instruments I had never used before. I experienced many good times with them.

I would also like to thank the members of my dissertation committee. Their comments, discussions, and insight are very important for improving the quality of this dissertation.

TABLE OF CONTENTS

LIST OF TABLES	viii
LIST OF FIGURES	ix
LIST OF ABBREVIATIONS	xviii
ABSTRACT	xix

Chapter

1	INTRODUCTION TO ULTRA-WIDEBAND PHASED ARRAY ANTENNA.....	1
1.1	UWB Active Phased Array Antenna Using Optical Approach.....	2
1.2	Overview of UWB Array Antennas	5
1.2.1	State-of-the-Art in UWB Array Antennas.....	5
1.2.2	Radiation Elements for UWB Array Antennas	7
1.2.2.1	First-Generation Designs.....	7
1.2.2.2	Second-Generation Designs	9
1.3	Original Contributions and Dissertation Outline.....	12
2	2-50-GHZ ULTRA-WIDEBAND MODIFIED VIVALDI ANTENNA	15
2.1	Introduction to Vivaldi Antennas	15
2.2	Antenna Design and Parametric Study.....	16
2.2.1	Circular-Shape-Load Vivaldi Antenna.....	16
2.2.2	Slot-Load Vivaldi Antenna.....	20
2.3	Measured Results and Discussion	22
2.4	1 × 4 Phased Slot-Load Vivaldi Antenna Array.....	28
2.5	Summary.....	31
3	METAMATERIAL-INSPIRED WIDEBAND ELECTRICALLY SMALL ANTENNA.....	32
3.1	Introduction to Electrically Small Antenna.....	32
3.2	Subwavelength Coupled D-Ring Resonators	34

3.3	Operating and Design Principle.....	37
3.3.1	Driving Mechanism.....	37
3.3.2	Embedded Wideband Impedance Matching.....	42
3.3.3	Ground Effect.....	48
3.4	Results and Discussion.....	48
3.5	Summary.....	54
4	OPTICALLY DRIVEN TIGHTLY COUPLED PHASED ANTENNA ARRAY.....	56
4.1	Introduction to Tightly-Coupled-Array Antennas.....	56
4.2	Electrical Excitation of TCA Antennas.....	60
4.2.1	Balanced Feed.....	60
4.2.2	Unbalanced Feed.....	63
4.2.3	Scan Blindness.....	64
4.3	Optical Excitation of TCA Antennas.....	65
4.3.1	Concept of Photodiode-Coupled Antennas.....	65
4.3.2	Analysis of Photodiode-Coupled TCA Antennas.....	67
4.3.2.1	Circuit Model.....	67
4.3.2.2	Performance of Photodiode-Coupled TCA Antennas ..	73
4.3.3	Design of Photodiode-Coupled TCA Antennas.....	76
4.3.3.1	Radiation Bandwidth.....	76
4.3.3.2	Photodiode Biasing Network.....	80
4.3.3.3	Concerns in Integration Process.....	81
4.3.4	A Design Example: 12-GHz-Bandwidth TCA (Connected- Dipole) Antenna.....	81
4.3.4.1	Infinite TCA Antenna.....	81
4.3.4.2	Finite \times Infinite TCA Antenna.....	86
4.4	Summary.....	87
5	ULTRA-WIDEBAND FEED NETWORK FOR OPTICALLY ADDRESSED PHASED ANTENNA ARRAY.....	89
5.1	Introduction to Optical Feed Network.....	89

5.2	UWB Tunable Photonic RF Source	90
5.3	Novel Optical Phased Feed Network	92
5.3.1	Operating Principle.....	92
5.3.2	Analysis of the Optical Feed Network	93
5.4	Excess Noise.....	96
5.5	Experimental Demonstrations	102
5.5.1	Two-Channel Network with Manual SoP Controls.....	102
5.5.2	Four-Channel Network with Adaptive SoP Controls.....	105
5.6	Summary.....	109
6	SYSTEM DEVELOPMENT AND DEMONSTRATION.....	110
6.1	Optically Addressed Phased Array Transmitter Architecture	110
6.2	Ultra-wideband Tunable RF Synthesizer	113
6.3	Optical Feed Network and Phase Control	115
6.4	High-Sensitivity Photonic RF Receiver	116
6.5	Experimental Demonstration: 4 × 4 Ka-Band Patch Antenna Array	120
6.5.1	Patch Antenna Design	120
6.5.2	Experimental Results.....	122
6.6	Experimental Demonstration: 1 × 4 Photodiode-Coupled TCA	127
6.6.1	Development of a 1 × 4 Photodiode-Coupled TCA	127
6.6.2	Integration of Photodiodes with the TCA	128
6.6.3	Far-Field Measurement	130
6.6.4	Near-Field Measurement.....	133
6.7	Summary.....	135
7	CONCLUSIONS AND FUTURE WORK.....	136
7.1	Summary and Conclusions	136
7.2	Future Work.....	138
	REFERENCES	139
	Appendix	
	LIST OF PUBLICATIONS.....	147

LIST OF TABLES

Table 2.1	The geometric parameters for the antenna	19
Table 2.2	The resonant frequency incurred by the slot-load	22
Table 3.1	Parameters of the coupled D-rings driven by the interdigital monopole (unit: mm).....	49
Table 6.1	Measured photodiode responsivities	129

LIST OF FIGURES

Figure 1.1	Architecture of an optically addressed UWB phased array. This architecture employs a widely tunable photonic RF source, optically based feed network, analog phase shifter, high-speed down-conversion module, and UWB antennas. (TTD: true time delay, OA: optical amplifier.)	3
Figure 1.2	Narrow-line widely tunable RF Source based on [3]. The picture is a fully integrated chip-scale system with notional rendering.	4
Figure 1.3	Chart of status of ultra-wideband antenna array technology since 1990s. 6	
Figure 1.4	Major types of radiating elements for wideband antenna array and comparison of their advantages and disadvantages.	7
Figure 1.5	(a) Stripline-fed tapered-slot antennas, (b) 144-element dual-polarized tapered-slot arrays, from [6], © 2000 IEEE.	8
Figure 1.6	Comparison of TSA and bunny-ear antenna arrays. (a) The tapered slot is relatively long, two wavelength or more, and longitudinal surface current tends to produce high cross-pol. (b) The bunny-ear is shorter with negligible longitudinal current and hence produce lower cross-pol. (c) Front side of a 9×9 element dual-pol egg-crate array, from [7], © 2003 IEEE.	9
Figure 1.7	(a) 32-element long-slot array for 150 – 600 MHz operation, from [9], © 2006 IEEE; (b) 5×5 interwoven spiral antenna array for 30 – 300 MHz operation, from [15], © 2011 IEEE; (c) single-polarization CSA breadboard showing the coupled elements (left), entire aperture (middle), and feed network (right) designed for 2 – 18 GHz, from [10], © 2007 IEEE; (d) the fragment element (left) and array aperture (right) for 0.3 – 10 GHz operation, from [12], © 2011 IEEE.	11
Figure 2.1	A conventional antipodal Vivaldi antenna. Red is the bottom layer, yellow is the top layer, and blue is the substrate.	17
Figure 2.2	The circular-shape-load Vivaldi antenna. Red is the bottom layer, yellow is the top layer, and blue is the substrate.	18

Figure 2.3	The simulated return loss of circular-shape-load Vivaldi antenna with $\alpha = 0.1$ and varies d of 0, 10, 20, 25mm.	20
Figure 2.4	The simulated return loss with $d = 20$ mm and varies α of 0.05, 0.08, 0.1, 0.13.	20
Figure 2.5	The slot-load Vivaldi antenna. Red is the bottom layer, yellow is the top layer, and blue is the substrate.	22
Figure 2.6	Fabricated (a) circular-shape-load Vivaldi antenna and (b) slot-load antenna.	23
Figure 2.7	The measured return loss respectively of the conventional, circular-shape-load, and slot-load Vivaldi antenna.	24
Figure 2.8	Simulated and measured radiation patterns of the circular-shape-load and slot-load Vivaldi antenna at (a) 4 GHz, (b) 10 GHz, (c) 20 GHz, and the measured results at (d) 30 GHz, (e) 40 GHz, and (f) 50 GHz.	27
Figure 2.9	Measured H-plane radiation patterns of the slot-load antenna.	27
Figure 2.10	Measured versus simulated gain. (a) Circular-shape-load and (b) slot-load Vivaldi antenna.	28
Figure 2.11	1-to-4 feed network with different fixed true time delays to achieve beam shift of 0° , 18° , and 30° , respectively.	29
Figure 2.12	The fabricated 1×4 slot-load Vivaldi antenna array with the true-time delayed lines.	29
Figure 2.13	The measured normalized radiation patterns of beam steering at frequencies of (a) 4 GHz, (b) 8 GHz, (c) 12 GHz, and (d) 16 GHz.	30
Figure 3.1	Two planar coupled D-ring whose parameter in the figure are $L_x = 20.5$ mm, $L_y = 26$ mm, $w = 1$ mm, $g = 0.05$ mm, $h = 25$ mil, and $t = 0.7$ mil.	34
Figure 3.2	Electric field distribution of two fundamental modes of the CDR resonator: (a) even mode at 2.1 GHz and (b) odd mode at 4.5 GHz.	35
Figure 3.3	The Q -factor and resonant frequency f_r versus the slit width g of the D-ring under the even mode.	36
Figure 3.4	Excitation mechanism of the D-ring resonator: (a) physical mechanism (dashed lines represents electric field and solid lines represent current distribution) and (b) simulated current distribution.	38

Figure 3.5	Equivalent circuit model of the D-ring is extracted from the HFSS simulation results.....	39
Figure 3.6	Circuit model of the CDRs and the monopole driven CDRs.	40
Figure 3.7	The input impedance Z_{in} of the monopole driven D-ring with the various coupling distance of g_c : (a) real part and (b) imaginary part.....	41
Figure 3.8	Antenna impedance matching techniques: (a) <i>LCL</i> T-network, (b) <i>CLC</i> T-network, and (c) transmission line.....	43
Figure 3.9	Smith chart of the impedance of the monopole driven D-ring antenna with g_c equal to 0.05 mm, 1 mm, and 2 mm, respectively, referenced to 50 Ω . In the figure, $f_L = 0.5$ GHz and $f_H = 2.0$ GHz.....	44
Figure 3.10	The mixed simulation model of the driven D-rings with a matching network.....	45
Figure 3.11	The simulated reflection coefficient of the interdigital coupler fed D-ring antenna with embedded matching network: (a) $L_m = 32$ mm, $Z_m = 70 \Omega$, 90 Ω , and 110 Ω ; (b) $Z_m = 110 \Omega$, $L_m = 10$ mm, 20 mm, and 30 mm.	46
Figure 3.12	The reflection coefficient of the D-rings driven by the interdigital coupler compared with that of the monopole-coupler.....	47
Figure 3.13	The interdigital monopole-driven D-ring antenna with meander line.....	47
Figure 3.14	The reflection coefficient with different ground size: (a) varied ground widths of 24 mm, 32 mm, and 40 mm, while maintaining the length of 4.4 mm; (b) varied ground lengths of 4.4 mm, 10 mm, and 70 mm, while maintaining the width of 24 mm.	48
Figure 3.15	The fabricated interdigital monopole-driven D-ring ESA.....	49
Figure 3.16	The comparison of the simulated and measured reflection coefficient. ...	50
Figure 3.17	The simulated radiation patterns of E-plane and H-plane at frequencies of 1.1 GHz, 1.3 GHz, 1.5 GHz, and 1.7 GHz.....	51
Figure 3.18	The simulated current distribution at the two resonant frequencies: (a) 1.1 GHz; (b) 1.7 GHz.....	52
Figure 3.19	The measured and simulated peak gain.....	53

Figure 3.20	The comparison of the calculated, simulated, and measured antenna efficiency.	54
Figure 4.1	Current Sheet with the current density of \mathbf{J} . The progressive phase can steer the radiation beam to the direction of (θ, ϕ)	57
Figure 4.2	Connected-dipole arrays are a realistic form of conceptual current sheet antennas. Each dipole is spaced in the period of d_x and d_y , which are much smaller than the wavelength in its operational bandwidth.	58
Figure 4.3	The equivalent circuit of connected-dipole arrays: (a) without a ground plane and (b) with a ground plane.	59
Figure 4.4	(a) Tightly coupled dipole arrays with a ground plane, (b) equivalent circuit.	59
Figure 4.5	(a) The electrical feed of a TCA implemented with an external balun, and (b) the result of VSWR, from [61], © 2013 IEEE.	61
Figure 4.6	(a) The electrical feed of a TCA is implemented with a hybrid integrated balun, and (b) results of VSWR, from [16], © 2013 IEEE.	62
Figure 4.7	The wideband balun using microstrip-to-stripline transition with a tapered ground (a) and VSWR (b), from [62], © 2009 IEEE.	62
Figure 4.8	(a) An unbalanced feed (the arrow line represents excited current), (b) TE ₁₀ -mode resonance caused by an unbalanced feed (the solid lines represent excited current, the dotted lines represent electric field).	63
Figure 4.9	Feed organizers for a dual-polarization CSA antenna, from [10], © 2007 IEEE.	65
Figure 4.10	A survey on status of development of high-power photodiodes. The output power of 1 W has been achieved by the MUTC4 photodiodes on diamond substrate with an operational bandwidth of 22 GHz. The output power of 38 mW has been achieved by the MUTC5 photodiodes with an operational bandwidth of 65 GHz. Figure courtesy of Prof. Joe Campbell, University of Virginia.	67
Figure 4.11	A Photodiode-coupled TCA comprising of connected dipoles each of which is driven by a photodiode. A photodiode can be simply equivalent to a current source in parallel with a capacitance.	68

Figure 4.12	The simulation configuration of an infinite connected dipole array. The parameters are chosen as $w_1 = 1.4\text{mm}$, $w_2 = 2.5\text{mm}$, $L_0 = 1.05\text{mm}$, $L_1=1\text{mm}$, $L_2=1\text{mm}$, $g = 1.04\text{mm}$. ABC is located at least a quarter-wavelength of the lowest simulation frequency. (a) Topview, and (b) sideview.	69
Figure 4.13	Simulated impedances of the connected dipole array fed by a lumped port with various port impedances (50Ω , 200Ω , 500Ω , and $1 \text{K}\Omega$), and a current port with infinite impedance. (a) Resistance, and (b) reactance.	70
Figure 4.14	Wideband equivalent circuit model of the TCA in Figure 4.12.	71
Figure 4.15	The impedance of a TCA reduces by N times when the SR ratio of the E-plane to the H-plane increases by N times. dx and dy are the spatial periodicities of the excitation sources along the x and y axis, respectively.	71
Figure 4.16	Simulated input impedances versus SR. The SR in the E-plane is 2, $8/3$, 4, and 8 while the SR of 2 maintains in the H-plane. (a) Resistance, and (b) reactance.	72
Figure 4.17	The equivalent circuit models of a photodiode-coupled TCA. (a) TCA antennas with a low SR, (b) TCA antennas with a high SR. Neither of them takes into account the losses from the photodiode and antenna.	73
Figure 4.18	The circuit representation of a photodiode-coupled antenna includes the bias circuit. A two-tone optical signal is incident on a photodiode producing a RF signal of I_{RF}	74
Figure 4.19	The radiation power density of a TCA when the SR is equal to 2 and 4.	77
Figure 4.20	(a) The HFSS simulation model of a TCA with an external resistor (top) and the driving port (bottom) and (b) the equivalent circuit. The dimensions of this model are given in Figure 4.12.	78
Figure 4.21	(a) Input resistance and (b) radiation power versus the applied external resistance calculated from the full-wave simulation and equivalent circuit model.	79
Figure 4.22	(a) The HFSS model of a photodiode-coupled TCA. (b) Simulated frequency responses of the input resistance and ideal frequency response without the effect of integration.	82

Figure 4.23	(a) HFSS simulation model (b) simulated frequency response of the input resistance before and after inductive peaking (c) equivalent circuit of a TCA integrated with photodiodes with an inductive-peaking circuit.	83
Figure 4.24	(a) HFSS model of the photodiode-coupled TCA incorporating of bias lines and integration components (ferrules and spacers) and (b) illustration of the coupling effect of the bias lines which could cause the radiation blindness.	84
Figure 4.25	Input impedance of the TCA when bias lines are not included: (a) resistance and (b) reactance.	85
Figure 4.26	Input impedance of the TCA when bias lines are present: (a) resistance and (b) reactance. The radiation blindness occurs at about 13 GHz due to the bias lines.	85
Figure 4.27	(a) HFSS model of $4 \times$ infinite TCA and (b) active impedances of four elements labeled in (a). The capacitance of photodiode and the impedance of TCA are accounted in the active impedances in (b).	87
Figure 5.1	Schematic illustration of photonic tunable RF signal generator, from [3], © 2013 Nature Photonics.	90
Figure 5.2	A simple scheme of optical feed network.	91
Figure 5.3	One channel of the proposed optical feed network scheme. PC: polarization combiner, PM: EO phase modulator, RT: 45° rotational key, LP: linear polarizer, PD: photodiode.	94
Figure 5.4	Schematic of polarization misalignment of the linear polarizer and the EO phase modulator. The electric field of TM mode in the cross plane are polarized along the x axis. The two tones of the incident optical signal are polarized along E_1 and E_2 , with the angles of ϕ_1 and ϕ_2 with respect to the x and y axis. The linear polarization is off the 45° and has the angle of γ with respect to the x axis.	97
Figure 5.5	The main and spurious radiation beams formed by the signal and excess noises. The two spurious beams are generated by the noise terms of i_{RFN} and i_{PMN} , respectively.	99
Figure 5.6	The simulation results of output signals with excess noises. (Top: an optical carrier corrupted by the noises incident into a photodiode. Middle: the intensity or envelop of the optical carrier. Bottom: the photodiode output.).....	100

Figure 5.7	Excess noises versus the polarization angle ϕ_2 of an incident optical signal (assumes $\phi_1 = 5^\circ$ and $\gamma = 45^\circ$). The results are obtained from a transmission matrix and an analytical method for comparison.	101
Figure 5.8	Schematic of an improved optical feed network with polarization controls to suppress excess noises.	102
Figure 5.9	The measurement setup consisting of (a) 1×2 optical fiber feed network and (b) a transmitting horn antenna and two receiving horn antennas. .	103
Figure 5.10	The experimental far-field response of the single channel under a periodic saw-tooth voltage signal applied to the phase modulator.	104
Figure 5.11	The measured radiation patterns of the 1×2 phased array under electric beam scanning.	105
Figure 5.12	(a) The four-channel optical feed network, and (b) a 1×2 Vivaldi antenna array and far-field measurement setup.	106
Figure 5.13	The experimental far-field response of a single channel when a periodic saw-tooth voltage signal is applied to the EO phase modulators.	107
Figure 5.14	The output DC current of the photodiode when a periodic saw-tooth voltage signal is the EO phase modulator with and without polarization control.	108
Figure 5.15	The measured radiation patterns at 20 GHz with different bias voltages on the EO phase modulator.	109
Figure 6.1	Functional modules of an optically addressed phased array: RF synthesizer, optical phase control, electronic control, and active frontends.	111
Figure 6.2	Schematic of a four-channel optically addressed phased array transmitter.	112
Figure 6.3	The developed optically tunable RF synthesizer. The devices shown in the figure are two optical lasers, an optical semiconductor amplifier, an EDFA, optical filter, EO phase modulator, and RF local oscillator.	113
Figure 6.4	Measured power of the RF source tunable from 4 – 50 GHz with a step frequency of 0.5 GHz.	114

Figure 6.5	Measured phase noise spectrum of the generated RF source at 35 GHz as function of offset frequency.	115
Figure 6.6	The developed optical phased feed network and phase control module.	116
Figure 6.7	Developed photonic receiver.	117
Figure 6.8	Photonic receiver based on optical up-conversion technique.	118
Figure 6.9	(a) The configuration of a microstrip-fed slot-coupled patch antenna. (b) Fabricated 4x4 patch array antenna, in which every four elements in the vertical direction are fed in-phase with power splitter to form a subarray, and four of such subarrays are fed by the optically addressed feed network to attain a phased array. (c) Simulated and measured S parameters of four subarrays. (d) Simulated radiation patterns at 36 GHz over the active beam scanning angles of $\pm 50^\circ$ in the E-plane.	121
Figure 6.10	(a) Far-field measurement system, in which a progressive phase distribution is applied to the array elements to illustrate the beam scanning capability over an angular range from -90° to 90° . (b) Measured far-field pattern as a function of time over four repeating scans at different frequencies between 34 – 38GHz.	123
Figure 6.11	(a) Far-field radiation pattern measurement setup for a given electrical beam steering direction. (b) Far-field radiation pattern measurements of the 4×4 phased array antenna with fixed phase assignment at each channels at different frequencies of 34, 36, and 38 GHz, respectively.	125
Figure 6.12	The developed 12-GHz TCA board. (a) The dipoles, 221- Ω chip resistors, and 0.1- μ F wideband capacitors reside on the topside. (b) The bias network and photodiodes are on the backside.	127
Figure 6.13	Integration procedure: (a) the photodiode is flip-chip bonded on the ceramic submount, (b) the photodiode is glued with the TCA substrate and is wire bonded with the antenna, (c) an optical fiber is glued with a ferrule and is polished, (d) a quartz chip is attached to the polished ferrule, (e) several quartz spacer are placed around the photodiode, (f) the optical fiber is aligned and bonded with the photodiode.	129
Figure 6.14	Fabricated 1×4 active antennas with integrated optical fibers.	130
Figure 6.15	Far-field measurement in an anechoic chamber. (a) TCA under test as a transmitter, (b) double-ridge horn as a receiver.	130

Figure 6.16	The received radiation power of each element excited individually at a time. The maximum power is off the broadside particularly at the high frequencies.....	131
Figure 6.17	The measured versus the simulated radiation patterns: (a) 4 GHz and 6 GHz, and (b) 10 GHz and 12 GHz.	132
Figure 6.18	Measured beam scanning at the frequency of 12 GHz.....	133
Figure 6.19	Near-field scanning patterns at the frequencies of 4 –12 GHz.	134
Figure 6.20	Normalized radiation power of the TCA versus frequencies.	135

LIST OF ABBREVIATIONS

UWB:	Ultra-Wideband
VCO:	Voltage Controlled Oscillator
RF:	Radio Frequency
EO:	Electro-Optic
TCA:	Tightly Coupled Array
AESA:	Active Electrically Steered Antenna
SWaP:	Size, Weight, and Power
TTD:	True-Time Delay
TSA:	Tapered Slot Antenna
CSA:	Current Sheet Antenna
ESA:	Electrically Small Antenna
CDR:	Coupled D-Ring
Balun:	Balance-to-Unbalance
PC:	Polarization Controller
PM:	Phase Modulator
LP:	Linear Polarizer
PD:	Photodiode
DFB:	Distributed Feedback
EDFA:	Erbium Doped Fiber Amplifier
DWDM:	Dense Wavelength Division Multiplexing
SoP:	State of Polarization

ABSTRACT

Demands for high data rate and multifunctional apertures from both civilian and military users have motivated the development of ultra-wideband (UWB) electrically steered phased arrays. Meanwhile, the need for large contiguous frequency bands is pushing radio systems to operate well into the millimeter-wave (mm-wave) range, fundamentally redefining UWB performance as covering the full spectrum from VHF to mm-wave.

Traditional electronic systems suffer from many difficulties to achieve this end. Several examples of these difficulties include the inability of voltage controlled oscillators (VCO) to provide a tunable range of several octaves, the high loss and dispersion wideband local oscillator (LO) signals undergo when distributed over radio-frequency (RF) transmission lines, and the limited bandwidth or bulky size of antennas that is hard to be integrated. Recently, RF photonics technology has drawn considerable attention because of the advantages it offers over traditional systems such as extreme power efficiency, information capacity, frequency agility, and spatial beam diversity. A hybrid RF photonic communication system, utilizing optical links and a RF transducer, potentially provides high-speed data transmission over ultra-wide tunable carriers from 1 to over 100 GHz.

Successful implementation of such an optically enabled phased array requires addressing several key challenges. The first challenge, developing a photonic RF source with a tuning range of several octaves, has been demonstrated in the last few years. The second challenge is how to convey phased optical signals to down-

conversion modules and antennas. Overcoming this challenge will require the development of optical feed networks with phase sweeping capability and low noise. Another key challenge is the development of ultra-wideband antennas and arrays. Modern frontends require antennas to be compact, planar, and low-profile in addition to possessing a broad bandwidth, while conforming to stringent space, weight, cost, and power constraints.

To meet these challenges, broadband and miniaturization techniques applicable to both single and array antennas are studied. Two ultra-wideband compact Vivaldi antennas are presented. The two antennas use distinct loading structures, a circular-shape-load and a slot-load, and both achieved ultra-wideband performances of more than 46 GHz. Loading structures also allow the antennas to achieve their larger bandwidths in a smaller length and aperture than comparable unloaded antennas, resulting in a compact integrated structure. A wideband, electrically small, planar, coupled D-ring resonator antenna driven by an interdigital monopole with an embedded matching network is also presented. This antenna, with a footprint of $\lambda/10 \times \lambda/14$ (λ is wavelength at 1 GHz), achieves an impedance-matched bandwidth of 1 – 1.7 GHz.

In addition, the design, fabrication, and integration of an optical feeding scheme are investigated to achieve efficient excitation of tightly-coupled-array (TCA) antennas. This optical feeding scheme is superior to conventional electrical feeding schemes in that it preserves the ultra-wide bandwidth and low profile of a TCA antenna. Moreover, light coupling into a photodiode only requires the space to secure a fiber ferrule, which allows the optical feeding scheme to be used in dense antenna arrays, like the TCA antenna, that support high frequencies into the mm-wave regime.

In addition, a novel optical feed network is proposed to distribute two-tone coherent optical signals for mixing in the frontend of an active RF aperture with low phase noise via orthogonal polarizations of an optical fiber. The proposed feed network is comprised of optical components with abundant RF bandwidth. Beam steering is also demonstrated using electro-optic (EO) phase modulators.

Finally, these components are brought together to demonstrate an optically addressed phased array transmitter architecture. The advantages of this architecture include low transmission losses, low phase noise, a light weight and flexible distribution network, a conformal structure, ultra-wideband operation, easy implementation, and large scalability.

Chapter 1

INTRODUCTION TO ULTRA-WIDEBAND PHASED ARRAY ANTENNA

Many modern advanced radio systems require active electrically steered antennas (AESA) which have a number of advantages, e.g., multiple independently steerable beams, polarization flexibility, and high reliability. Multiple trends are simultaneously occurring in AESA development today. First, AESAs are increasingly required to be “multifunctional” [1]. The broadband radio apertures in a multifunctional system are shared between radar, passive electronic support measures, active electronic counter measures, and communications functions. A multifunctional system has greater flexibility for multiple missions and multiple roles, increased effectiveness and improved survivability. To this end, the radio integrated circuit chips in the frontend of an AESA need to support multiple bands and share one antenna aperture.

Second trend is that AESAs are being developed with reduced size, weight, and power plus cost (SWaP+C). In particular, low-profile and conformal frontends are highly desired. These properties allow antennas to be embedded into the skin of a platform (e.g., aircrafts, ships). The benefits of this approach include reduced drag, enhanced electromagnetic performance, reduced electromagnetic signature, and enhanced damage resistance and structural efficiency [2].

Third trend is scaling operating frequencies of AESAs, which migrate into mm-wave range [1]. Ubiquitous access to data via wireless radio-frequency links is of such great value to both civilian and military users that it is safe to say that the demand

for higher data rates is virtually unquenchable. From smart phones delivering real-time video and navigation assistance, to military unmanned aerial vehicles (UAV) collecting high-resolution surveillance imagery around the globe, there is at present a mismatch between the amount of useful information that is acquired or stored at a remote location, and the capacity of wireless networks to deliver it where it is needed. However, congested RF bands below 6 GHz are noncontiguous and aggregating to only 780 MHz. In comparison, large contiguous bands are available at mm-wave frequencies from 30 – 110 GHz.

In the future, AESAs will be required to possess extremely broad bandwidth (e.g., 100:1), be conformably deployed on various platforms, and be compliant with stringent constraints of SWaP+C.

1.1 UWB Active Phased Array Antenna Using Optical Approach

To realize a multifunctional AESA system, conventional RF technologies face multiple challenges for achieving ultra-wide bandwidth such as the limited fractional bandwidth over which waveguides and other key components can operate. A solution to overcoming these challenges is the use of coherent RF photonics: upconverting RF signals into the optical domain, where components such as Lithium Niobate (LiNbO_3) modulators, semiconductor lasers, and optical fibers provide operational bandwidths that exceed the entire RF spectrum. For example, 200 GHz represents a fractional bandwidth of only 0.1% for a 200-THz optical carrier. Furthermore, compared to conventional RF components, optical components are often vastly lighter, exhibit lower losses, are immune to electromagnetic interference (EMI), and frequently are less costly. Therefore, the ability to use an optical architecture for active phased arrays offers an opportunity to exploit enormous absolute bandwidth associated with optics

by acquiring and processing signals in the optical domain. The goal of the research described in this dissertation has been to develop a new concept as candidate solutions to realize multifunctional UWB phased arrays by exploiting RF photonics techniques.

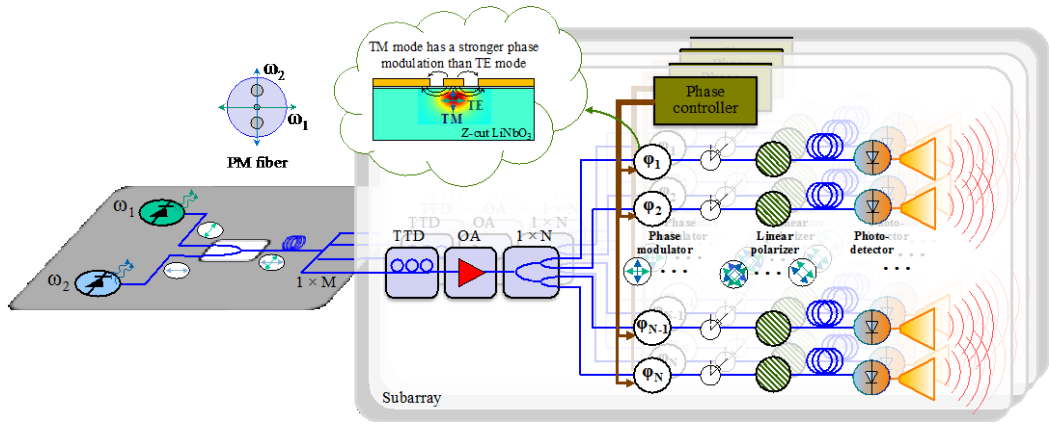


Figure 1.1 Architecture of an optically addressed UWB phased array. This architecture employs a widely tunable photonic RF source, optically based feed network, analog phase shifter, high-speed down-conversion module, and UWB antennas. (TTD: true-time delay, OA: optical amplifier.)

Figure 1.1 shows a schematic of an optically addressed phased array transmitter architecture proposed for this dissertation. The development of such an architecture requires many technological advances, including a widely tunable RF synthesizer with high spectral purity, an optically-based phased feed network consisting of true-time delay (TTD) lines and analog phase shifters, and antenna-coupled, high-speed, high-power down-conversion modules, and low-profile UWB array antennas. This concept evolved from the widely tunable photonic RF source [3], illustrated in Figure 1.2. This RF source generation is based on the use of electro-optic (EO) phase modulation of a master semiconductor laser to frequency-shift a portion of

the output by a select multiple of a low-frequency RF reference. By phase locking a second semiconductor laser to the shifted portion (after filtering), the two lasers can be mixed at a fast photodetector, resulting in a RF beat tone that exhibits extraordinary RF spectral purity. Using this method [3], it has been shown that the generated RF signal has 1-Hz linewidth and is tunable from 4 GHz to 110 GHz.

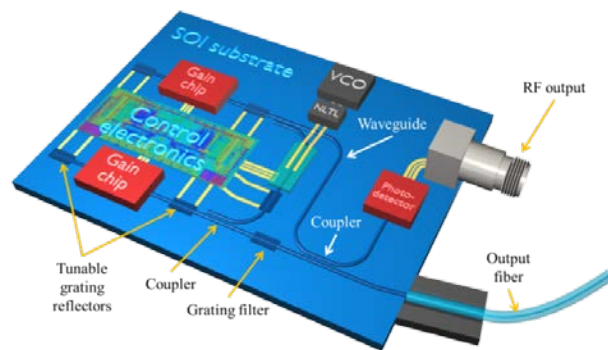


Figure 1.2 Narrow-line widely tunable RF source based on [3]. The picture is a fully integrated chip-scale system with notional rendering.

Since RF signals are borne on optical carriers through the entire system, there is no need for costly, bulky high-frequency cables and waveguides. As a result, the proposed system well suited for network-scale signal distribution. To achieve signal distribution and beam steering, an optical feed network with low insertion losses and low noise is required. Another essential component in the system is antenna arrays with ultra-wide bandwidth to match the frequency agility of signal sources, which operate over many octaves of bandwidth. Without UWB antennas, the phased array will be either restricted to narrow operating bandwidths, or be bulked up with multiple narrow band antennas. This dissertation addresses the challenges arising from the

development of the UWB phased array, ranging from optical feed network to UWB antennas and arrays.

1.2 Overview of UWB Array Antennas

1.2.1 State-of-the-Art in UWB Array Antennas

Tremendous effort has been made to develop UWB array antennas in recent decades, and multiple significant advances has been achieved in the area. To recap the history, Figure 1.3 shows a summary of the most popular UWB arrays together with their invention date and performance parameters. Some milestone events since the 1990s are listed as follows:

- In 1994, a single-polarized “bunny-ear” antenna array operating at 850 – 1400 MHz was developed at Hughes [4].
- In 1997, Raytheon developed a multifunctional array using tapered-slot antennas (TSAs) operating at upper C, X, and Ku band (about 4 – 18 GHz) [5].
- In 1999, 144-element dual-polarized TSA array with operating bandwidth of 1 – 5.9 GHz was developed at University of Massachusetts (UMass) [6].
- In 2003, Raytheon developed a 9×9 bunny-ear dual-polarized antenna array operating at 1 – 5 GHz [7].
- In 2004, Raytheon developed a bunny-ear dual-polarized antenna array operating at 3 – 14 GHz [8].
- In 2005, the UHF long-slot aperture was developed with an operating bandwidth of 0.4 – 2 GHz at Raytheon [9].
- In 2007, Harris developed a TCA array operating at 2 – 18 GHz [10].
- In 2009, NRL developed an all-metal TSA array operating at 0.7 – 9 GHz [11].

- In 2011, Georgia Tech developed a fragmented antenna aperture operating at 0.285 – 10 GHz [12].
- In 2012, OSU developed a TCA array with ground plane and embedded resistive FSS for the operation of 0.3 – 5.92 GHz [13].
- In 2013, UMass developed a planar ultra-wideband modular antenna (PUMA) operating at 7 – 21 GHz [14].

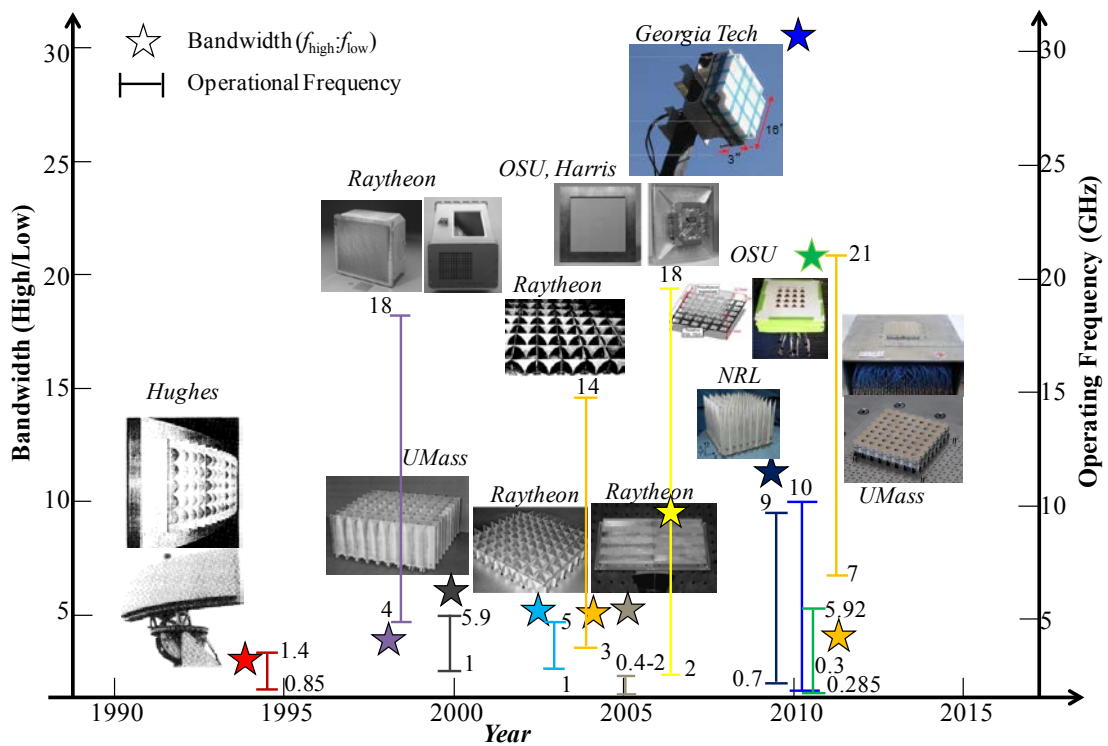


Figure 1.3 Chart of status of ultra-wideband antenna array technology since 1990s.

As indicated from the survey, the trends in the development of UWB arrays include an increase in bandwidth, low-profile (subwavelength depth at the high end of a bandwidth), and migration to high-gigahertz frequencies (e.g., mm-wave).

Performance of an antenna array is mostly determined by that of its elementary

radiators. Some elements suitable for UWB arrays are high-profile tapered-slot antenna (TSA), low-profile bunny-ear antenna, and current sheet antenna (CSA), tightly coupled dipoles and spirals. The operating frequency of UWB arrays has increased from UHF to Ku band. The next section will briefly compare strengths and weaknesses of these most popular elements for UWB arrays.

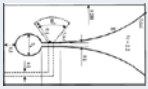
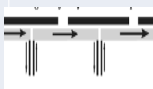
Coupled Radiating Element	Vivaldi	Bunny Ear	Long Slot	Dipole (Current Sheet)	Spiral	Fragment
Element						
Developer (Appearance Time)	Raytheon (1990, one pol) UMass (1999, dual pol)	Raytheon (2003)	Raytheon (2005)	OSU, Harris (2007)	OSU (2011)	Georgia Tech (2011)
Pros	easy to feed	easy to feed, low profile, and cross-pol	low profile, planar	planar, low profile and cross-pol	wider bandwidth, planar, and low profile	wider bandwidth, planar, and low profile
Cons	high profile and cross-pol	not planar, external balun needed	complicate feeding, low frequency	external balun needed	low frequency, circular-pol	lower efficiency, high cross-pol

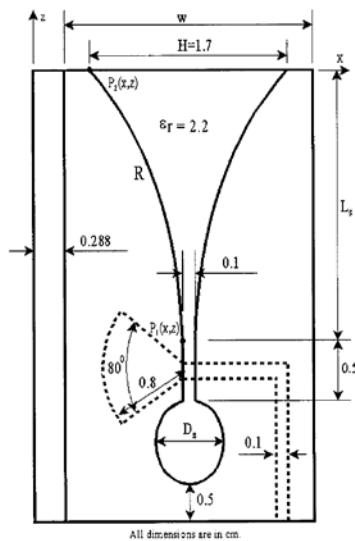
Figure 1.4 Major types of radiating elements for wideband antenna array and comparison of their advantages and disadvantages.

1.2.2 Radiation Elements for UWB Array Antennas

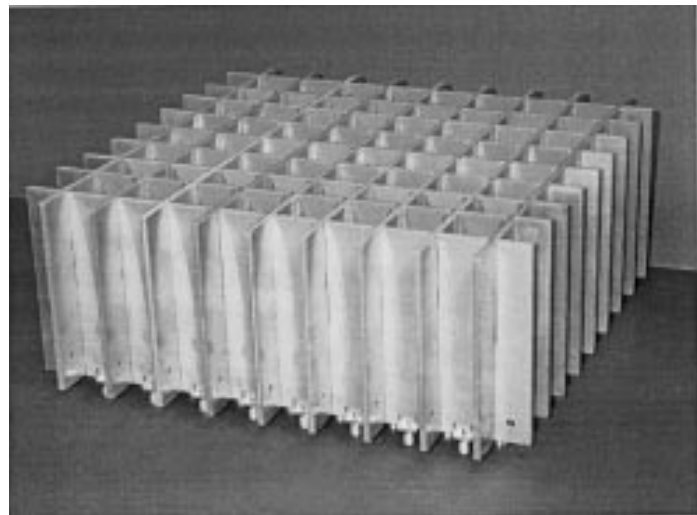
1.2.2.1 First-Generation Designs

Figure 1.4 lists the following UWB array elements: TSA, bunny-ear antenna, long-slot antenna, and tightly-coupled-array (TCA) antenna that are comprised of dipole, spiral, or fragment antenna. The TSA, as shown in Figure 1.5, is the first generation of UWB arrays. This array can be easily fabricated and fed by microstrip or

stripline. In most cases, a TSA array operates in a frequency band for which their tapered slots are longer than half a wavelength at the low end of a band and larger than two wavelengths at the high end for a typical 3:1 bandwidth. Wider bandwidth can be accommodated with a longer taper, but the element radiation pattern may become narrower due to higher gain and grow unstable with scan blindness when higher order modes begin to degrade the aperture distribution [7]. Several drawbacks are inherent in a TSA array. First, a TSA array has a high profile, which is not suitable for UHF antennas on airborne platforms. Second, high-order modes exist along the E-plane of a TSA array, which can cause undesired resonances. Third, TSA arrays are known to produce high cross-polarization in the principal planes (E- and H-plane) and especially in diagonal cut.



(a)



(b)

Figure 1.5 (a) Stripline-fed tapered-slot antennas, (b) 144-element dual-polarized tapered-slot arrays, from [6], © 2000 IEEE.

Many of the drawbacks associated with a TSA array can be mitigated in bunny-ear antenna arrays. Figure 1.6 shows bunny-ear antennas, the profile of which is compared with that of the TSAs with a similar operational bandwidth. As illustrated in the figure, both of the inner and outer edges of bunny-ear antennas are flared. This geometry provides bunny-ear antennas with lower profile and stronger immunity to scanning blindness [7]. Bunny-ear antennas require parallel striplines as an input port and, if fed by coaxial lines, baluns from coaxial line to stripline become necessary. As a result, the operational bandwidth is directly constrained by the performance of the baluns employed in the array.

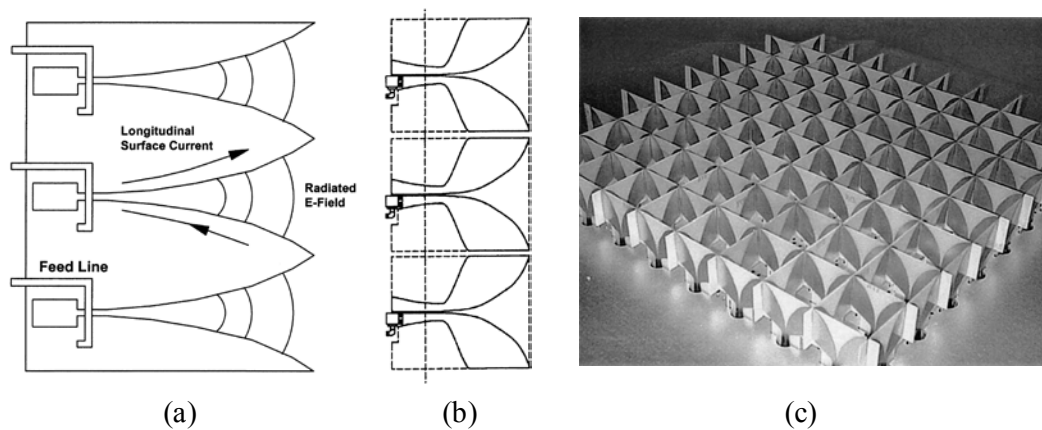


Figure 1.6 Comparison of TSA and bunny-ear antenna arrays. (a) The tapered slot is relatively long, two wavelength or more, and longitudinal surface current tends to produce high cross-pol. (b) The bunny-ear is shorter with negligible longitudinal current and hence produce lower cross-pol. (c) Front side of a 9×9 element dual-pol egg-crate array, from [7], © 2003 IEEE.

1.2.2.2 Second-Generation Designs

Phased arrays comprised of other radiating elements, such as long slots [9], connected dipoles, and tightly coupled elements, e.g., dipoles [10], bowties, and

spirals [15], are originated from the same concept of current sheet antenna (CSA). These antenna arrays are the second generation of UWB arrays. Differing from a TSA and a bunny-ear array, a CSA can be fabricated on an ultra-thin substrate in a planar and conformal form. In the absence of a ground plane, an ideal CSA can possess infinite bandwidth. Given these positive characteristics, CSAs have become the premier candidate for UWB arrays and therefore are receiving increasing attention lately. Figure 1.7 shows the four typical CSA forms: (a) a 32-element long-slot array for 150 – 600 MHz operation, (b) a 5×5 interwoven spiral array for 30 – 300 MHz operation, (c) a tightly coupled dipole array for 2 – 18 GHz operation, and (d) a fragment array aperture for 0.3 – 10 GHz operation.

Although a CSA has many distinct advantages, there are multiple challenges in realizing efficient excitation over ultra-wide bandwidth. First, its feed lines are physically normal to the surface of the radiation elements. Second, the input impedance of a CSA is much higher than 50Ω , which cause difficulty in impedance match when $50\text{-}\Omega$ RF coaxial cables are used as the feed lines. Third, CSA elements usually have a symmetrical geometry, thus requiring an UWB balun to suppress common-mode excitation. Fourth, the integration of RF cables with CSA elements is difficult to perform at mm-wave frequencies due to their small dimensions and limited space. To circumvent these challenges, various techniques have been used: placing another substrate of feeding circuitry vertically to that of the CSA elements [13], applying external bulky wideband baluns [10], and using narrowband integrated balun and impedance matching network [16]. However, these methods can significantly degrade the performance of a CSA and are not viable at mm-wave frequencies. Further discussion of feeding techniques for CSAs is detailed in Chapter 4.

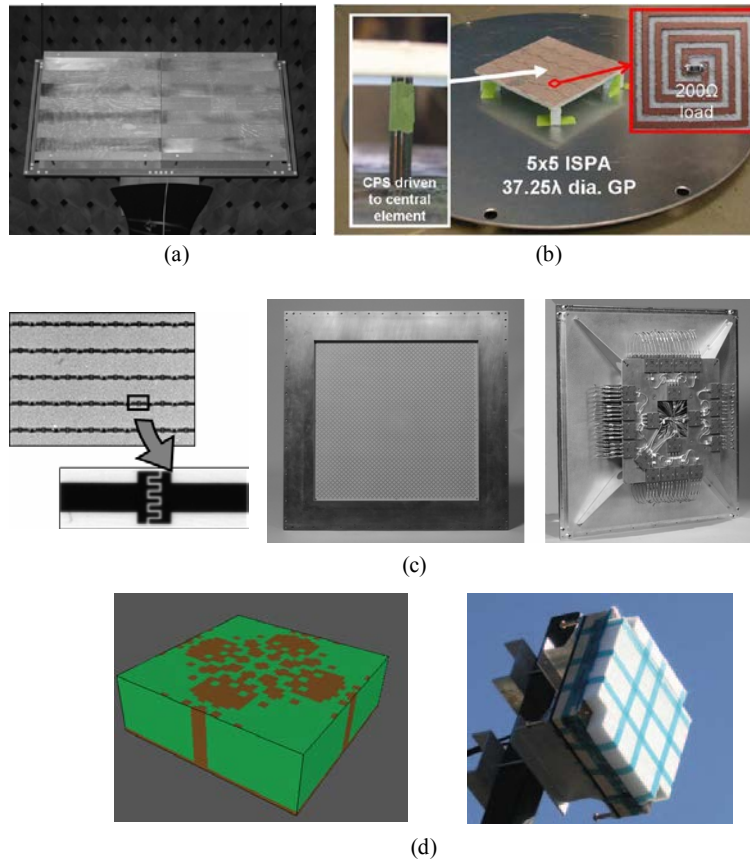


Figure 1.7 (a) 32-element long-slot array for 150 – 600 MHz operation, from [9], © 2006 IEEE; (b) 5×5 interwoven spiral antenna array for 30 – 300 MHz operation, from [15], © 2011 IEEE; (c) single-polarization CSA breadboard showing the coupled elements (left), entire aperture (middle), and feed network (right) designed for 2 – 18 GHz, from [10], © 2007 IEEE; (d) the fragment element (left) and array aperture (right) for 0.3 – 10 GHz operation, from [12], © 2011 IEEE.

To better understand the state of the art of CSAs, let us compare their relative strengths and weaknesses of a variety of tightly coupled radiation elements used in CSAs. A long-slot and connected-dipole array are complementary in geometry, so they have similar impedance characteristics. However, planar connected-dipole arrays possess the lowest cross-polarization. In addition, the reactive energy contained in

their feeds can be tuned in order to achieve broad matching independently from the scan angle [17]. An interleaved-spiral array demonstrates the widest bandwidth, but suffers from high cross-polarization. A fragment-antenna array exploits a genetic algorithm (GA) to synthesize a broadband radiation aperture. It actually can be seen as infinite current sheet where the current flows in any path rather than two orthogonal directions. Fragment arrays also suffer from high cross-polarization. As a result, tightly coupled dipole antennas are a relatively better candidate for practical applications requiring both ultra-wide bandwidth and low cross-polarization.

The preceding survey provides essential context for the research effort described in this dissertation and also raises two significant questions. The first question is how to design UWB antenna arrays for an optically addressed phased array system? Second, what are the essential differences between optically fed and electrically fed antennas? The above questions will be addressed throughout this dissertation.

1.3 Original Contributions and Dissertation Outline

I introduced multiple novel techniques used in the process of developing an optically addressed phased array. Specifically:

- A novel optically addressed phased array transmitter architecture is proposed. This architecture features ultra-wide bandwidth, spatial agility, and low SWaP.
- A novel UWB Vivaldi antenna with an operational bandwidth of more than 46 GHz is proposed. The loading techniques can effectively increase the bandwidth of Vivaldi antennas while keeping the antennas compact.

- A wideband electrically small antenna is proposed. It has an operational bandwidth of 1 – 1.7 GHz and efficiency approaching the Chu limit.
- Photodiode-coupled TCA antennas as well as their analysis, design, and fabrication methods are developed. This optical feeding scheme preserves the operational bandwidth of a TCA antenna and can drive a TCA antenna at high-gigahertz frequencies.
- A novel optical feed network realized by interleaved optical fibers with low excess noise is demonstrated. This optical feed network can distribute two-tone coherent optical signals across an RF aperture with low loss and distortion.

This dissertation is organized as follows:

In Chapter 2, I examine Vivaldi antennas and propose two modified antipodal Vivaldi antennas terminated by two different kinds of loadings to match the termination of a traditional Vivaldi antenna. Although the physical mechanisms of the two loads which enable the antenna to radiate below the cutoff frequency are different, both are able to mitigate the restriction on the antenna length and aperture, thereby offering a more compact antenna configuration for a particular UWB operation.

In Chapter 3, I first review metamaterial-inspired techniques used in the design of electrically small antennas. Then, an electrically small antenna with a footprint of $\lambda/10 \times \lambda/14$ (where λ is the free-space wavelength at 1 GHz) is developed comprised of a subwavelength resonator driven by an interdigital monopole coupler, along with an embedded matching network. This antenna operates over the bandwidth of 1 – 1.7 GHz and has the efficiency approaching the Chu limit.

In Chapter 4, the history of TCA array and various excitation methods are first reviewed. Then, the concept of an optically fed photodiode-coupled TCA is proposed to overcome many practical difficulties occurring in electrical feeding schemes. Analysis and design techniques required by the optically fed array are investigated. As an example, a connected-dipole array with an operational bandwidth of more than 12 GHz is designed and simulated.

In Chapter 5, a novel optical phased feed network is proposed. The excess noise coupled into the optical signals imparted to the antennas undermines the beam steering of the optically addressed phased array. This chapter offers a candidate solution to address this issue.

In Chapter 6, a novel optically addressed phased array transmitter architecture, briefly described in Chapter 1, is further described and implemented. A system prototype comprised of RF source generation, optical feed network, integrated active antenna, and electronic control, is developed. Two different antenna arrays, i.e. patch and TCA, are employed in measurements to demonstrate for the concept's validity.

In Chapter 7, I summarize this dissertation and provide some insight towards future research. The analysis and design method introduced in this dissertation can be applied to develop a larger phased array with a higher operational frequency.

Chapter 2

2-50-GHZ ULTRA-WIDEBAND MODIFIED VIVALDI ANTENNA

2.1 Introduction to Vivaldi Antennas

The Vivaldi antenna [18] is one of the best candidates for UWB radio systems due to its planar structure, low profile, light weight and ultra-wide bandwidth. Vivaldi tapered slot antenna (TSA) generally consists of two different structures, i.e. coplanar [19] and antipodal [20] geometry. Coplanar Vivaldi antennas usually offer wideband performance, i.e., two octaves. This limitation is mainly imposed by the feeding transitions, e.g., microstrip-to-slotline, to work as the feeding balun used in coplanar Vivaldi antennas. For instance, in this structure, microstrip fan-shaped stub produces very high radiation loss and even distorts radiation patterns at high frequencies. Compared with a coplanar Vivaldi antenna, an antipodal one, however, can achieve much wider bandwidth, i.e. $> 10:1$, owing to some natural UWB feeding transitions, e.g., microstrip-to-parallel stripline. One drawback involved in antipodal Vivaldi antennas is relatively high cross polarization. J. D. S. Langley, *et al.*, [21] presented a balanced antipodal configuration capable of lowering the cross polarization. The design criteria and performance of conventional Vivaldi antennas have been reported [22], [23]. The bandwidth of Vivaldi antennas is generally proportional to their length and aperture. Therefore, the antenna becomes bulky when UWB performance is desired. Some modifications were implemented on coplanar Vivaldi antennas to attain compact configuration [20], [21], [19] – [32]. Corrugated aperture edge is applied to mitigate sidelobe level as the width of the antenna outer edge decreases [19] [24].

Numerical techniques has also been employed in order to optimize antenna geometrical parameters [26]. In addition, dual exponentially tapered slots antenna (DE TSA) have been achieved by modifying antipodal Vivaldi antenna to minimize the size for UWB operation. However, the radiation patterns of DE TSA lack directivity and stability [27]. Thus far, there has been few reported compact Vivaldi antenna with over 25:1 impedance bandwidth to meet the requirements of an ultra-wideband antenna array fed with a RF-photonics system.

In this chapter, I propose two modified antipodal Vivaldi antennas which are terminated by two different kinds of loadings, i.e., circular-shape-load and slot-load to match the termination of a traditional Vivaldi antenna [28]. Although the physical mechanisms of two loads, which enable antenna to radiate below the cutoff frequency, are different, both are able to mitigate the restriction on the antenna length and aperture, thereby offering more compact antenna configuration for a particular UWB operation. Both antennas are simulated with three dimensional AYSYS High Frequency Structural Simulator (HFSS) based on finite element method (FEM). All the measurements are implemented on Agilent PNA Network Analyzer E8361C.

2.2 Antenna Design and Parametric Study

2.2.1 Circular-Shape-Load Vivaldi Antenna

Figure 2.1 shows the geometry of a conventional Vivaldi antenna designed on a 10-mil substrate with a dielectric constant of 2.3. In the design of an antipodal Vivaldi antenna, two arms metalized on either side of the substrate are flared in the opposite direction to form a tapered slot. To improve the impedance characteristics, the exponentially tapered slot is typically defined as:

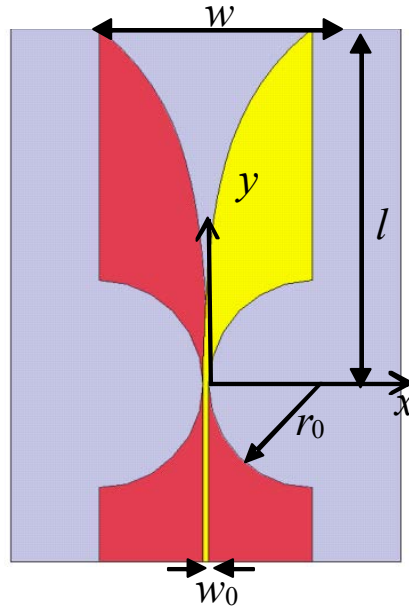


Figure 2.1 A conventional antipodal Vivaldi antenna. Red is the bottom layer, yellow is the top layer, and blue is the substrate.

$$x = \begin{cases} w_0 - 0.5w_0 \exp(\alpha y) & \text{top layer} \\ -w_0 + 0.5w_0 \exp(\alpha y) & \text{bottom layer} \end{cases} \quad (2.1)$$

where w_0 is the width of the feeding microstrip, and α is the rate of exponential transition, which can be determined by:

$$\alpha = \frac{1}{l} \ln \left(\frac{w_0 + 0.5w}{0.5w_0} \right), \quad (2.2)$$

where l is the effective radiation length and w is the aperture size. The antipodal configuration allows for a natural transition from microstrip feeding, thereby providing ultra-wideband characteristics as well as lower radiation loss at high frequencies compared to the microstrip-to-slotline transition used in coplanar Vivaldi antennas. Circular taper with radius of r_0 is used to microstrip ground to achieve the

transition from microstrip to parallel strip line. An optimal radius of $r_0 = 11.6$ mm is used. For a given tapered slot length of $l = 40$ mm and aperture of $w = 24$ mm, α needs to be optimized for an ideal bandwidth. The antenna cutoff wavelength can be defined by [23]:

$$\lambda_c = 2w \quad (2.3)$$

As a result, the lower cutoff frequency is about 7 GHz here. In other words, the current aperture and length of this conventional Vivaldi antenna has to be approximately enlarged three times to reach the lower cutoff frequency of 2 GHz.

To further improve the bandwidth while making the antenna compact, the circular-shape-load Vivaldi antenna, as shown in Figure 2.2, is proposed. This antenna is attained by adding a circular load on each arm of the conventional one. The outer edge of circular load matches with the conventional Vivaldi antenna. The overall extension distance d , circle center (x_0, y_0) and radius of r , are related by:

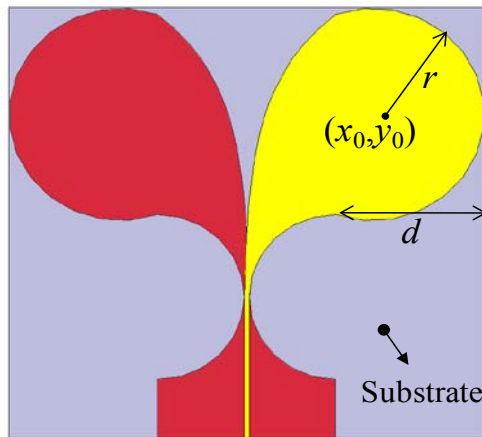


Figure 2.2 The circular-shape-load Vivaldi antenna. Red is the bottom layer, yellow is the top layer, and blue is the substrate.

$$r = \left[\frac{(l-r_0)^2}{4} + d^2 \right] / 2d \quad (2.4)$$

$$\begin{cases} x_0 = r_0 + d - r \\ y_0 = r_0 + (l-r_0)/2 \end{cases} \quad (2.5)$$

Based on our previous discussion, the parameter d along with α is to be optimized under the criteria of achieving the widest bandwidth and compact geometry through a parametric study. First, by maintaining α constant, the return loss by varying d is investigated. Figure 2.3 is the simulated return loss with $\alpha = 0.1$ and d varying from 0, 10 mm, 20 mm, and 25 mm, respectively, illustrating the impedance bandwidth to be dramatically expanded by applying the load. Without the load ($d = 0$), the lowest operating frequency with return loss less than -10 dB is about 9 GHz. By increasing d , this frequency can be lowered to about 4 GHz. However, it is also observed the return loss has no noticeable change at d above 20 mm. In addition, I keep d constant and vary α to study impedance characteristics. Figure 2.4 shows the simulated return loss with d of 20 mm and α respectively of 0.05, 0.08, 0.1, and 0.13. As shown from Figure 2.4, return loss decreases as α increases from 0.05 to 0.1 and then increases when α is above 0.1. Therefore, $\alpha = 0.1$ and $d = 20$ mm is found to offer the ultra-wideband performance and compact configuration with the circular-shaped load. All of the geometrical parameter values are listed in Table 2.1.

Table 2.1 The geometric parameters for the antenna

w_0	r_0	l	w	α	d	S
0.675mm	11.6mm	40mm	24mm	0.1	20mm	0.9mm

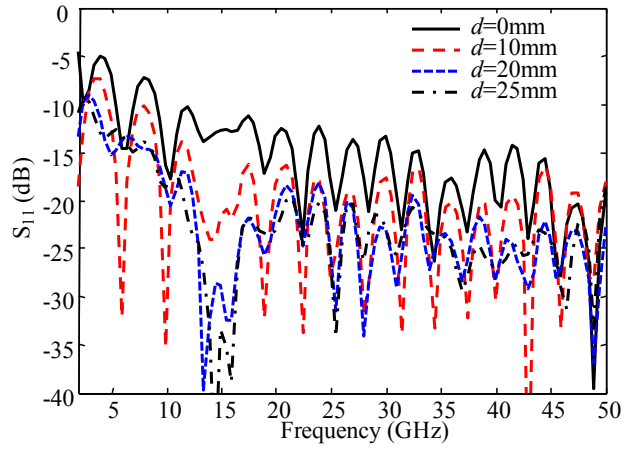


Figure 2.3 The simulated return loss of circular-shape-load Vivaldi antenna with $\alpha = 0.1$ and varies d of 0, 10, 20, 25mm.

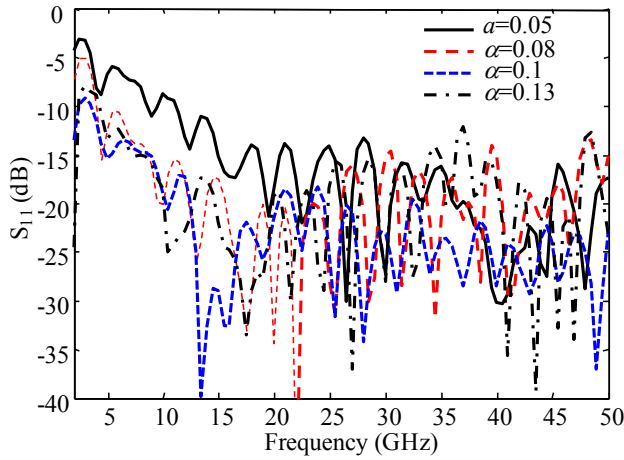


Figure 2.4 The simulated return loss with $d = 20$ mm and varies α of 0.05, 0.08, 0.1, 0.13.

2.2.2 Slot-Load Vivaldi Antenna

The antenna impedance bandwidth at low frequency can be further increased. In addition, the radiation pattern can be improved and tailored to achieve high directivity. To achieve this, the slot-load antenna as shown in Figure 2.5 is proposed.

Such an antenna is designed by properly introducing slots on the optimized circular-shape-load. Extensive numerical studies on the slot orientation have been performed, and it concludes that the orientation of the slots chosen about 45° with respect to y -axis provides the better directivity. The slot-load basically gives rise to two-folded effects on the performance of the circular-shape-load antenna. First, due to the change of the current flow, i.e., the current distributes along the “fingers” instead of the circular edge, actually producing more directive radiation pattern than the circular-shape-load Vivaldi antenna. Secondly, loaded slots will change the return loss of circular-shape-load Vivaldi antenna, particularly at relative low and high frequency range. This is because the circular-shape-load is mainly characterized as a resistor whereas the slot-load is more like an RLC resonator. The resonant wavelength of each finger can be approximately estimated by

$$l_s = \lambda_0 / 4 \sqrt{\frac{1 + \epsilon_r}{2}} \quad (2.6)$$

where l_s is length of each finger and ϵ_r is dielectric constant of the substrate. In order to achieve a wideband performance, multiple slots with varied lengths are used to merge these resonances. The gradually increased length of the six fingers on each load is listed in the Table 2.2. Slot width of s does not impact return loss apparently, except for the resonances slightly shifted toward the lower frequency as s decreases. This phenomenon similarly exists in all dipole antennas. By the parametric study, the slot width of s is chosen as 0.9 mm to achieve a good impedance bandwidth. The design parameters for the slot-load antenna are listed in Table 2.1 and Table 2.2.

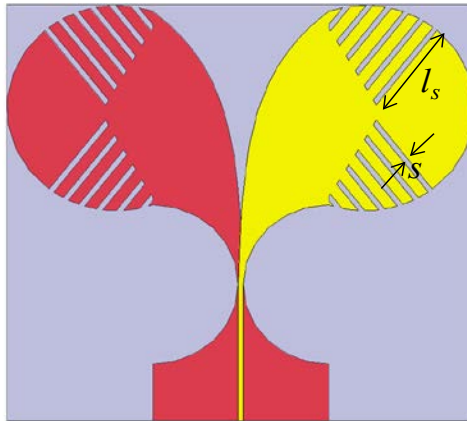


Figure 2.5 The slot-load Vivaldi antenna. Red is the bottom layer, yellow is the top layer, and blue is the substrate.

Table 2.2 The resonant frequency incurred by the slot-load

Finger Lengths (mm)	Calculated f_0 (GHz)	Simulated f_0 (GHz)	Measured f_0 (GHz)
13.7	4.3	4.3	4.3
12.7	4.7	4.7	5.0
11.3	5.2	5.2	5.8
9.6	6.2	6.0	6.2
7.4	8.0	7.5	7.5
4.5	13.0	13.5	13.0

2.3 Measured Results and Discussion

The antenna is fabricated with standard lithography technology on a 10 mil thick Rogers Duroid 5880 substrate, and then is attached on a piece of Eccostock SH8 (polyurathane) foam with very low loss and dielectric constant in order to keep the antenna stable during measurement. The antennas are fed through 2.4-mm coaxial

adaptor capable of working from DC to 50 GHz. Figure 2.6 shows the fabricated circular-shape-load and slot-load Vivaldi antenna.

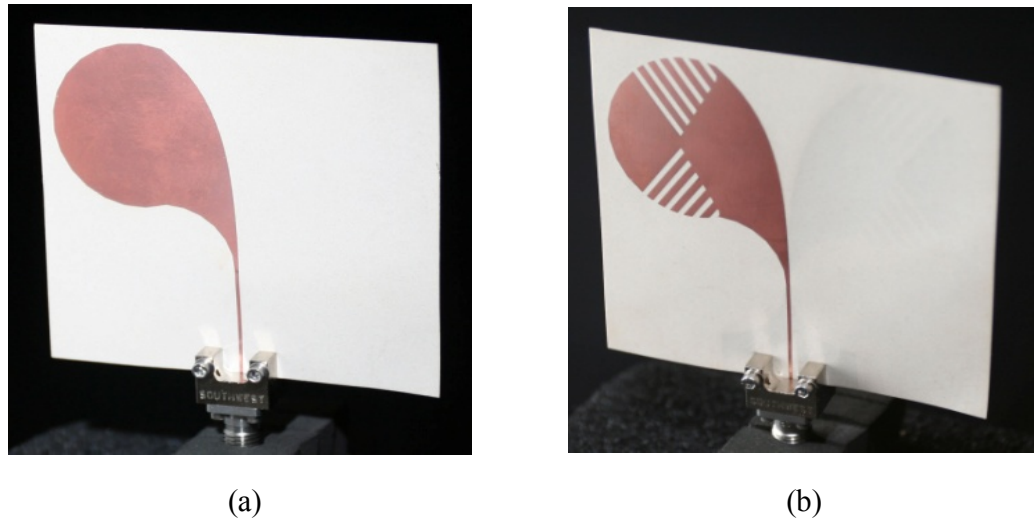


Figure 2.6 Fabricated (a) circular-shape-load Vivaldi antenna and (b) slot-load antenna.

The measured return loss of the conventional and modified Vivaldi antennas is compared in Figure 2.7. It can be seen that at the low frequency, i.e., 2 – 8 GHz, the slot-load Vivaldi antenna demonstrates the best wideband performance in terms of impedance bandwidth with a return loss less than -10 dB, except at a few frequencies. The results are also in agreement with the simulation. The return loss of the slot-load Vivaldi antenna becomes larger than that of the other two antennas, as seen from the figure, at the high frequency, i.e., 40 – 50 GHz, which is attributed to a rising mismatch with large reactance involved in the slot-load. In summary, the achievable impedance bandwidth of the conventional, circular-shape-load and slot-load Vivaldi antennas with geometrical parameters in Table 2.1 are about 9 – 50 GHz, 4 – 50 GHz, and 2 – 50 GHz, all with the typical return loss less than -10 dB and the maximum less

than -8 dB. Therefore, the antennas with the optimized loads, i.e., circular-shape-load and slot-load, can dramatically improve the impedance bandwidth and achieve compact geometry.

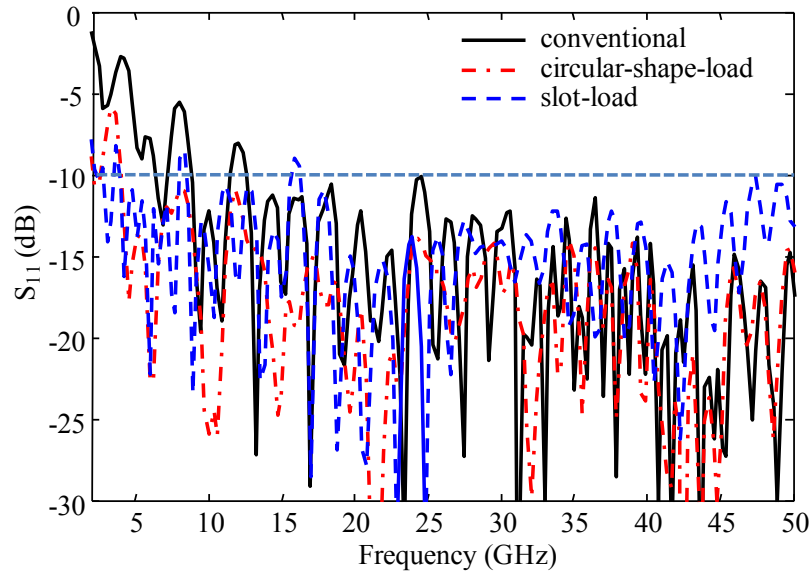


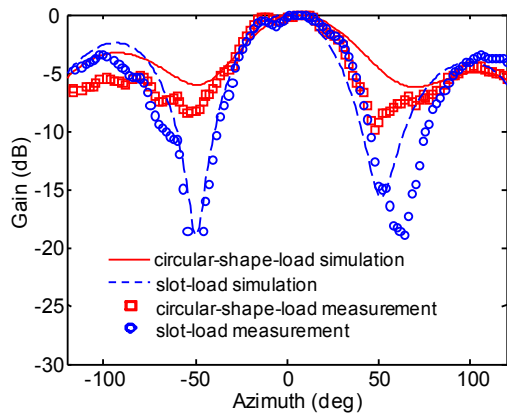
Figure 2.7 The measured return loss respectively of the conventional, circular-shape-load, and slot-load Vivaldi antenna.

The physical mechanism of circular-shape-load Vivaldi antenna with the capability of radiating below the cutoff frequency of the conventional Vivaldi antenna can be explained as follows. Surface current on the metallization layers is primarily confined to the metallization edges of the radiating flares. At high frequencies, the longer electric length of tapered slot allows sufficient radiation and thereby a small amount of current remains at the end of the flare. However, for low frequencies, the flare length in terms of wavelength is much shorter. As a result, the current on the flare is less efficiently radiated. In addition, the remaining current at the end of the flare cause the radiation pattern to be distorted. In the circular-shape-load Vivaldi

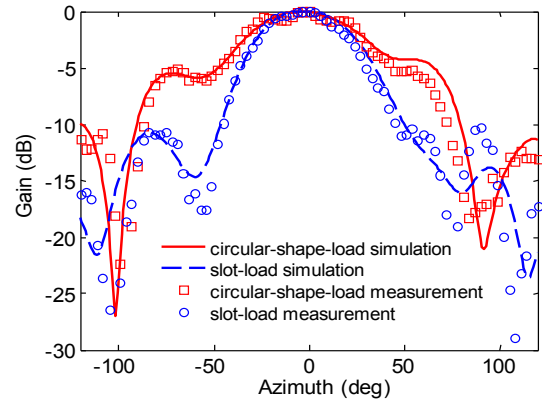
antenna, the current path is smoothly extended longer along the circular curve, and is thereby capable of providing symmetric radiation over an ultra-wide bandwidth. The slot-load Vivaldi antenna can radiate below the cutoff frequency, however, because the “fingers” at the end of the flare induce resonances. As a result, the slot-load antenna behaves like a resonant antenna with multiple resonant frequencies at low frequency instead of a traveling wave antenna at high frequency. As mentioned above, the fundamental resonances of the slots can be evaluated according to Eq. (2.6). It is worth examining the impact of the loaded slots on the return loss. Table 2.2 offers the comparison of the calculated resonant frequencies with the simulated and measured results. Good agreement between them allows accurate design to improve the impedance characteristic at low frequency.

Figure 2.8 shows the measured E-plane (the xoy plane in Figure 2.1) radiation patterns of both modified Vivaldi antennas at five frequencies in the range of 4 – 50 GHz. The measured results are also compared with simulations at 4 GHz, 10 GHz, and 20 GHz for validation. The comparison at higher frequency is not implemented due to limited computer memory and time. As seen from the figure, the measured E-plane patterns are in good agreement with the simulated results. In addition, the slot-load antenna displays better directivity in terms of smaller half-power beamwidth (HPBW) and sidelobes, especially at frequencies lower than 30 GHz. At higher frequencies, the radiation patterns of both antennas tend to be identical, because most power has already been radiated before arriving at the loading structures.

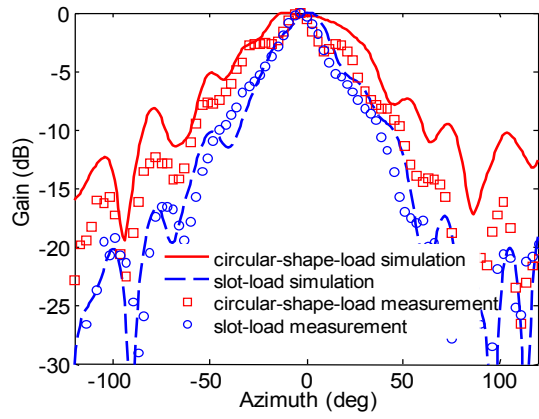
Figure 2.9 shows the measured H-plane radiation patterns of the slot-load antenna at 4 GHz, 10 GHz, 20 GHz, 30 GHz, and 40 GHz, respectively. Through examining the Figure 2.8 and Figure 2.9, I found the pattern beamwidths in both E and



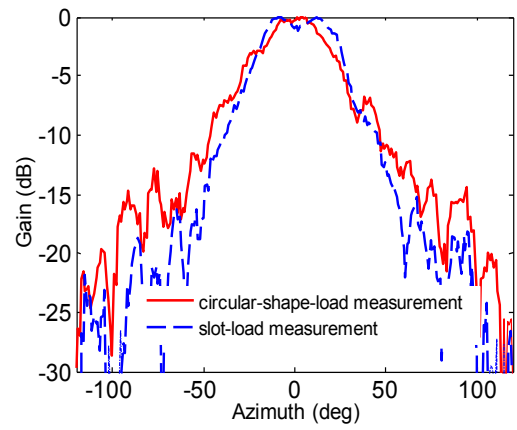
(a)



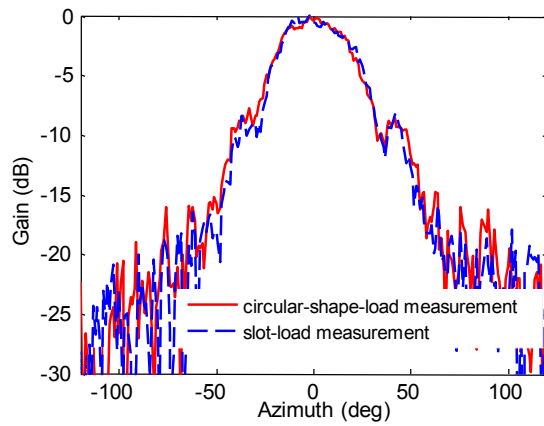
(b)



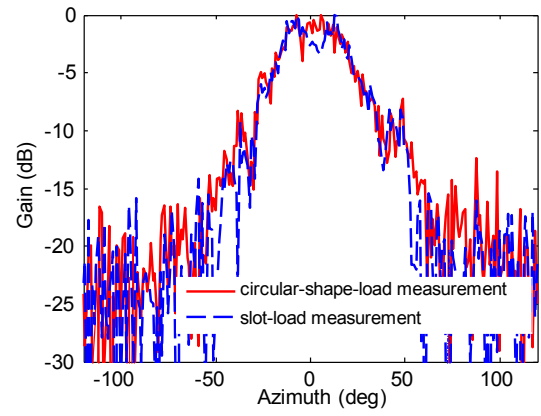
(c)



(d)



(e)



(f)

Figure 2.8 Simulated and measured radiation patterns of the circular-shape-load and slot-load Vivaldi antenna at (a) 4 GHz, (b) 10 GHz, (c) 20 GHz, and the measured results at (d) 30 GHz, (e) 40 GHz, and (f) 50 GHz.

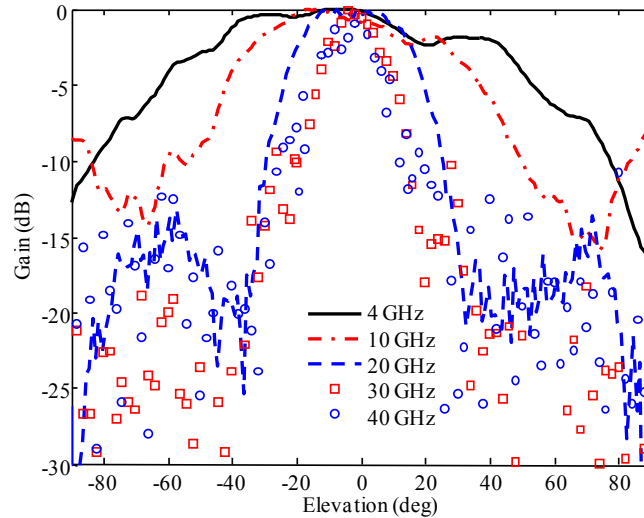
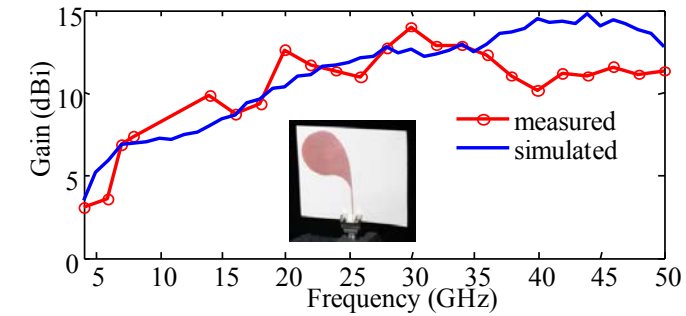


Figure 2.9 Measured H-plane radiation patterns of the slot-load antenna.

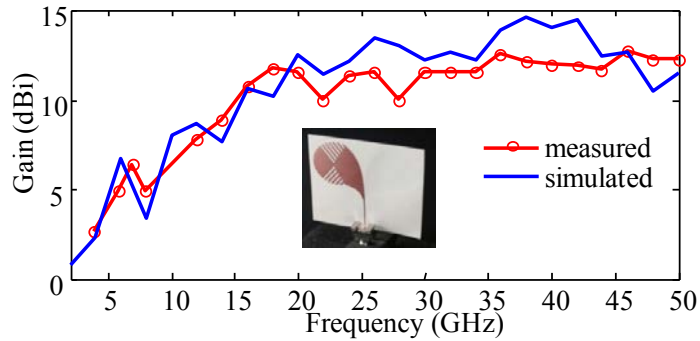
H-plane are wider at low frequencies and then narrow to a constant beamwidth as the frequency increases to above 30 GHz

The gain of the two antennas is slightly different, as shown in Figure 2.10, and varies between 3 to 12 dBi over 4 – 50 GHz. The discrepancy between the simulation and measurement is due to ohmic and substrate loss, surface roughness of fabrication and other factors which are very difficult to be predicted but significant at high frequency. The measured results of the gain and radiation patterns at the frequency below 4 GHz are not available here due to the measurement system capability of 4 – 50 GHz. According to the simulated result as shown in Figure 2.10 (b), the gain of the slot-load Vivaldi antenna at 2 GHz is expected to be about 1.0 dBi. The cross-polarization of the modified Vivaldi antenna is generally similar to the traditional one

and has maximum -15 dB in the operating bandwidth. It can be further lowered, if necessary, using a balanced antipodal structure.



(a)



(b)

Figure 2.10 Measured versus simulated gain. (a) Circular-shape-load and (b) slot-load Vivaldi antenna.

2.4 1 × 4 Phased Slot-Load Vivaldi Antenna Array

A 1 × 4 slot-load Vivaldi antenna array fed by fixed true-time delay lines is fabricated and characterized. To demonstrate beam steering, the feed network with three different fixed delay times, as shown in Figure 2.11, are applied to achieve beam shift of 0°, 18°, and 30°, respectively. The network is fabricated on a 10 mil thick RT/Duroid 6010 substrate with $\epsilon_r = 10.2$. Seven-order Chebyshev impedance

transformation from 100Ω to 50Ω is used to feed the array in order to achieve broadband operation.

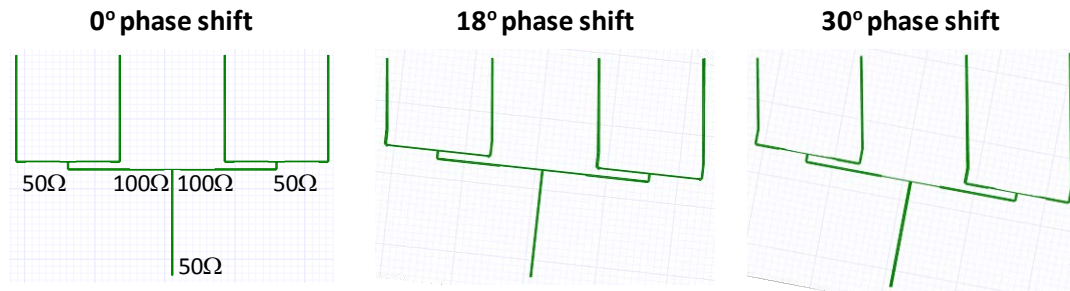


Figure 2.11 1-to-4 feed network with different fixed true time delays to achieve beam shift of 0° , 18° , and 30° , respectively.

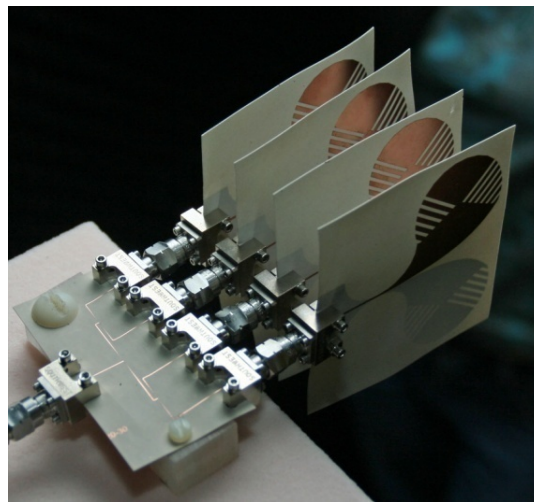


Figure 2.12 The fabricated 1×4 slot-load Vivaldi antenna array with the true-time delayed lines.

The fabricated array composed of four slot-load Vivaldi antennas as shown in Figure 2.12. The adjacent antennas are spaced with 15 mm. The experimental results

of beam steering at 4 GHz, 8 GHz, 12 GHz, and 16 GHz are shown in Figure 2.13 [33].

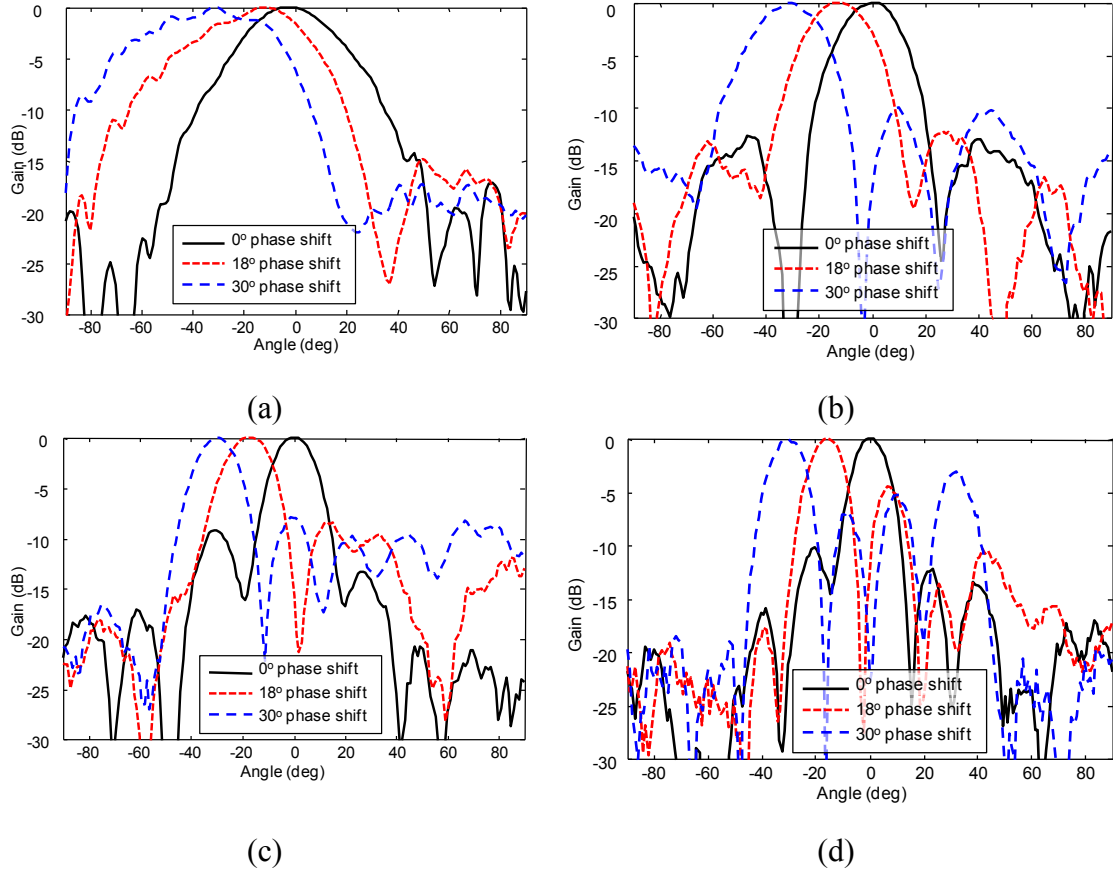


Figure 2.13 The measured normalized radiation patterns of beam steering at frequencies of (a) 4 GHz, (b) 8 GHz, (c) 12 GHz, and (d) 16 GHz.

The result demonstrates the array possesses capability of broadband operating of beam steering. The highest operational frequency is limited by the array element spacing, which ensures no grating lobe occurs inside the scanned zone of interest. It is noted that the highest sidelobe of the 30°-offset beam arises from -10 dB to -4 dB as the frequency increases from 4 GHz to 16 GHz. In addition, with the true-time delay, there is no beam squint observed as we expected.

2.5 Summary

This chapter presents two ultra-wideband compact Vivaldi antennas. By introducing two different loading structures, i.e., circular-shape-load and slot-load, both antennas have ultra-wideband performance of more than 46 GHz. Loading structures mitigates the requirement of bandwidth on the antenna length and aperture, resulting in a compact structure for the antenna. It is worth pointing out that the slot-load Vivaldi antenna can have wider bandwidth by manipulating the slot length and width to create a lower frequency resonance to be merged. In summary, the circular-shape-load Vivaldi antenna is characterized as lower return loss, while the slot-load Vivaldi antenna exhibits nearly 2 GHz wider impedance bandwidth with typical return loss of less than -10 dB except only a few frequencies which could cause problem. The slot-load Vivaldi antenna is allowed to possess the radiation pattern with suppressed sidelobes and higher directivity in a particular spectral range. The beam patterns of modified Vivaldi antennas are symmetric in both E- and H-plane and become stable when frequency is larger than 30 GHz. In addition, the modified Vivaldi antenna is characterized of compact geometry, symmetric and directive radiation pattern in antenna plane (xoy plane), convenient integration with optoelectronic circuit, therefore being suitable for realizing an ultra-wideband antenna array fed with a RF-photonics system. One more thing to be noted is the loading method employed in this chapter theoretically differs from other techniques utilized to optimize impedance characteristics, e.g., DETSA, which is through a modified tapered slot and flare. Therefore, our loading method can be applied together with dual exponential taper to achieve a more miniaturized configuration and wider operational bandwidth.

Chapter 3

METAMATERIAL-INSPIRED WIDEBAND ELECTRICALLY SMALL ANTENNA

3.1 Introduction to Electrically Small Antenna

Wideband, planar, electrically small antennas (ESAs) are receiving increased attention for applications in wireless communications and systems, most notably at VHF and UHF frequencies. Recently, metamaterial (MTM) based techniques have been investigated for use with ESAs [34]-[50] and in such techniques the MTM can be used for a variety of roles. MTMs with negative constitutive permittivity (ϵ) or permeability (μ), when used as substrates of antennas, can shift resonant frequencies to the lower end [34]-[36]. Zeroth-order MTMs have an infinite wavelength which allows for size reductions of antennas [39]-[41]. Split-resonator ring (SRR) MTMs can be used to impedance match small antennas to 50Ω [42]. A single unit of MTMs in these antennas can be viewed as a parasitic component capable of changing the impedance of feeding antennas, which usually dominates radiation. Another kind of MTM, capacitively loaded loops (CLLs), have coupling between resonance and radiation, and therefore they can be individually seen as antennas [43]-[45]; however, it is quite challenging to feed this kind of MTM-based antenna due to their extreme impedance property and naturally narrow bandwidth. Near-field coupling from the open stub of a coax has been able to drive CLLs, but a good impedance matching was only achieved in an exceedingly narrow band. Most of the MTM-based ESAs described above are subject to a narrow bandwidth, which limits practical applications

especially in emerging broadband wireless communications. In order to alleviate this problem, multi-band and multi-mode techniques of ESAs have been investigated [46]-[51]; however, the bandwidths are still less than 5% and most of them are not in a planar configuration.

To alleviate this problem, I present a planar ESA on the basis of coupled subwavelength resonators comprised of D-rings (see Figure 3.1) capable of resonating at a wavelength of about $1/12\lambda$. Coupled D-rings (CDRs) exhibit strong coupling to radiation and consequently very low Q values varying from 3.5 to 1.5 times the Chu limit when the number of arms of D-rings increases from two to eight [52]. Despite this advantage (lower Q values offers ESAs wider bandwidths because of $Q = 2/\text{FBW}_{3\text{dB}}$), only two coupled planar D-rings are used in order to realize a wideband ESA with a planar configuration, which is desired in many portable wireless devices. In addition, resonant frequencies of CDRs, unlike that of CLLs, are determined by both the physical dimension of a single ring and their mutual coupling (see Figure 3.6). Lower resonant frequencies can be achieved by closer spaced D-rings owing to their stronger mutual coupling. There are two fundamental resonant modes, i.e., even and odd mode, corresponding to capacitive and inductive coupling, respectively, between the two rings. Later it will be shown that the magnetically coupled D-rings have lower Q values than the capacitively coupled D-rings, which implies that it is the appropriate MTM for use in ESAs. It is quite challenging to drive the two coupled D-rings properly with an impedance match of a typical value of 50Ω , let alone in a wide bandwidth. I will show that D-rings with a footprint of $\lambda/10 \times \lambda/14$ (where λ is the free space wavelength at 1 GHz), driven by an interdigital monopole coupler with an embedded matching network, are able to be operated over the bandwidth of 1 – 1.70

GHz [53]. To the author's best knowledge, this is the widest bandwidth achieved by ESAs without using an external matching network composed of lumped components. In addition, the simulated result shows the efficiency approaches the theoretical Chu limit.

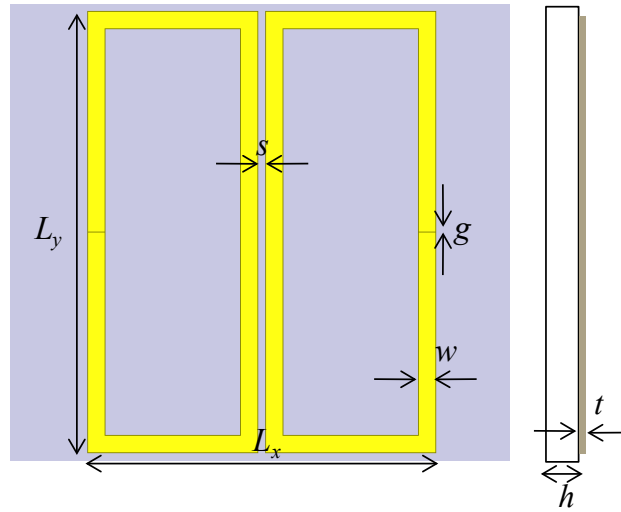


Figure 3.1 Two planar coupled D-ring whose parameter in the figure are $L_x = 20.5$ mm, $L_y = 26$ mm, $w = 1$ mm, $g = 0.05$ mm, $h = 25$ mil, and $t = 0.7$ mil.

3.2 Subwavelength Coupled D-Ring Resonators

A planar coupled D-ring resonator on a 25mil-thick Duroid 5880LZ substrate, as shown in Figure 3.1, consists of two rectangular metal rings with widths of w , spaced by a distance of s . Each ring has a slit with a width of g . All the parameters are shown in Figure 3.1 and their values are given in the caption. A CDR is expected to have two fundamental modes, i.e., even and odd mode, due to its symmetric geometry. The field distribution of each mode can be obtained by performing a numerical simulation of eigenmode analysis by placing the D-rings in a box surrounded by perfect matched layer (PML) boundaries. In the simulation, the metal of the rings is

set as copper with a conductivity of $\sigma = 5.8 \times 10^7$ siemens/m. Electric fields of the first two fundamental modes are shown in Figure 3.2. The simulation result shows that the first mode (see Figure 3.2 (a)) appears at a frequency of 2.1 GHz while the second mode (see Figure 3.2 (b)) appears at 4.5 GHz. Comparing the electric field distribution I find that the first mode has a symmetric field (therefore called even mode) while the field of the second mode is anti-symmetric (called odd mode). The even mode is of interest due to its smaller Q value, which indicates strong coupling to radiation because of the higher radiation loss involved. In fact, the electric field of the even mode is similar to that of a negative- ϵ sphere [52]. The field is fairly uniform inside the rings while outside the rings the field behaves like the field of a dipole. Moreover, the two rings have the same potential in the even mode and therefore are magnetically coupled. The resonant frequency f_r of the even mode is:

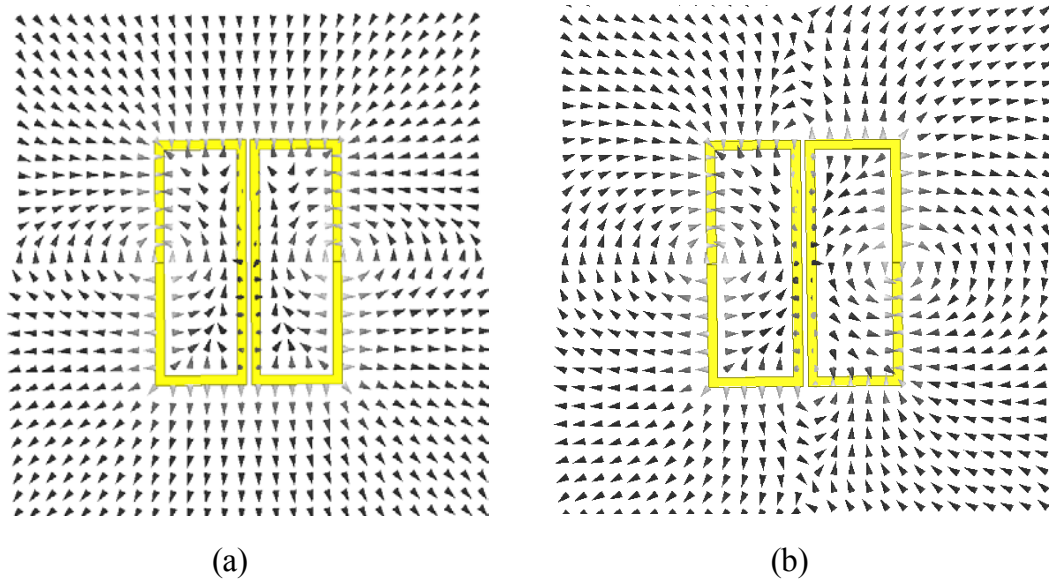


Figure 3.2 Electric field distribution of two fundamental modes of the CDR resonator: (a) even mode at 2.1 GHz and (b) odd mode at 4.5 GHz.

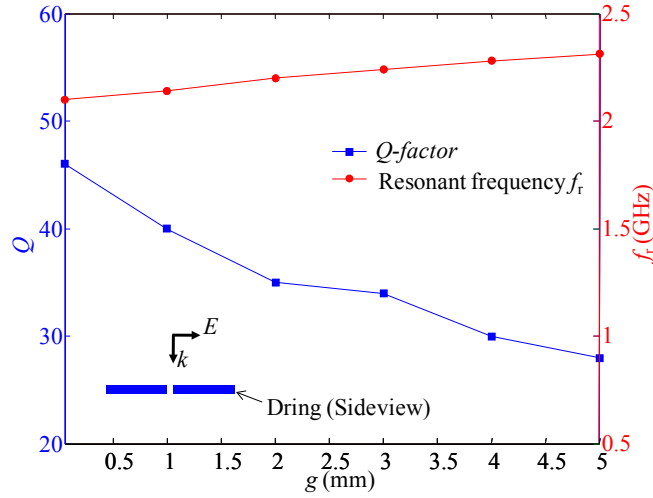


Figure 3.3 The Q -factor and resonant frequency f_r versus the slit width g of the D-ring under the even mode.

$$f_r = \frac{1}{2\pi} \frac{1}{\sqrt{(L_r + M_r)C_r}} \quad (3.1)$$

where L_r and C_r are the effective inductance and capacitance of a single ring, and M_r is the effective mutual inductance between two rings. In addition, I also investigate the Q -factor of the D-rings with different slit width g . To this end, the D-ring is placed in free space surrounded with radiation boundaries in HFSS. A planar wave with the polarization aligned with the slit is normally incident on the D-ring in order to only excite the even mode, as shown in the inset of Figure 3.3. At the resonant frequency, the D-ring has the largest scattering cross section, i.e., the highest scattering power. The Q -factor is estimated by the resonant frequency divided by 3-dB scattering power bandwidth. In this way, Q -factor and resonant frequency f_r are obtained for g equal to 0.05 mm, 1 mm, 2 mm, 3 mm, 4 mm, 5 mm, and 6 mm, respectively, as shown in Figure 3.3. It is observed that f_r increases as g increases while the Q -factor decreases.

In order to obtain a low resonant frequency, g equal to 0.05 mm is chosen and its corresponding Q -factor is 46. Therefore, Q/Q_{chu} of 11.6 is obtained when dielectric and conduction losses are not included. Q_{chu} is [54]:

$$Q_{\text{chu}} = \frac{1}{(ka)^3} + \frac{1}{ka} \quad (3.2)$$

where a is the minimum radius of a sphere enclosing the D-rings. The odd mode, unlike the even mode, is produced by a capacitive coupling between the two arms. The odd mode will also generate an undesired cross polarization. For the above reasons the ESA will be implemented by driving the even mode of the CDRs and suppressing the odd mode.

3.3 Operating and Design Principle

3.3.1 Driving Mechanism

The even mode of CDRs can be driven by a monopole between the two rings. The driving mechanism is plotted in Figure 3.4 (a). Part of the electric field flux (black dashed lines) originating from the monopole and flowing through the slits of the rings is able to generate a voltage or displacement current across the slits, activating these gaps. Such an activated gap, equivalent to an ideal current source (with an infinite impedance), can drive the rings. In this way, an effective drive can be achieved through electric or capacitive coupling between the monopole and rings. As a result, the driven current on the rings (red solid lines) will flow opposite to the driving current on the monopole (blue solid lines) as plotted in Figure 3.4 (a). The rings could also possibly be driven by magnetic coupling between the rings and monopole. In this case, the driven current would be flowing in the same direction as the driving current.

Because of the opposite direction of the driven current due to the two possible coupling mechanisms, I need to confirm the dominant case. Figure 3.4 (b) shows the simulated result of the current distribution at the resonant frequency of 1.7 GHz obtained by performing HFSS, which indicates that electric coupling is a major driving mechanism, which is consistent with prior analysis. The resonant frequency shift from 2.1 to 1.7 GHz will be explained later in this section.

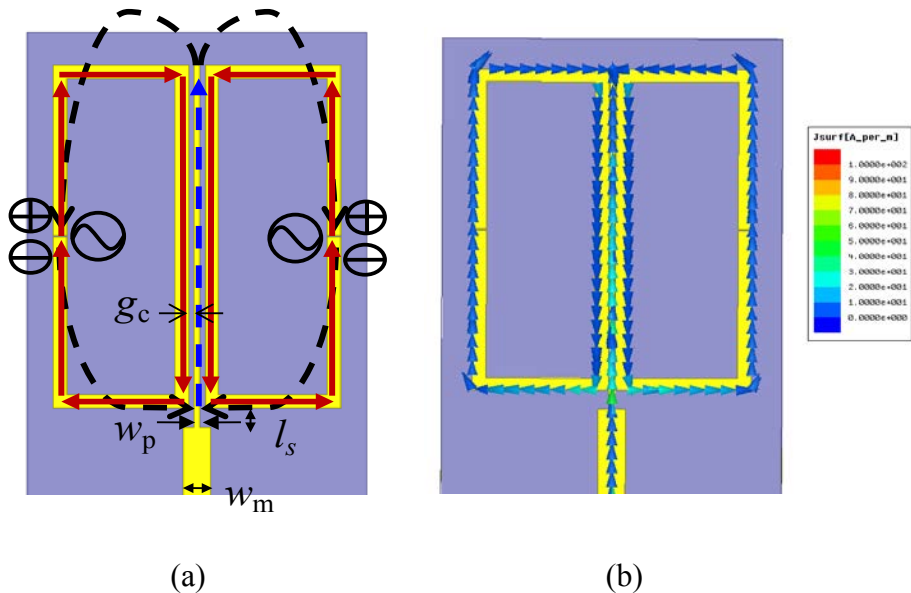


Figure 3.4 Excitation mechanism of the D-ring resonator: (a) physical mechanism (dashed lines represents electric field and solid lines represent current distribution) and (b) simulated current distribution.

The even mode of the CDRs behaves like an anti-resonance, which can be modeled as a parallel RLC circuit, where the equivalent inductance of L_r and capacitance of C_r are extracted as follows. At a high frequency, $C_r \approx 1/(2\pi f Z_{11})$ where Z_{11} is the self-impedance of the individual D-rings under normal illumination of a planar wave whose electric polarization is vertical to the slits on the rings. Then, $L_r =$

$1/(2\pi f_r)^2 C_r$, where f_r is the anti-resonant frequency of 2.1 GHz. As a result, the extracted L_r and C_r are 10.2 nH and 0.58 pF, respectively. Figure 3.5 shows the impedance obtained from the circuit model and full-wave simulation. A good agreement between the two results is observed and thereby verifies the modeling of the D-ring as a parallel RLC resonator near the frequency of 2.1 GHz. Based on the above analysis, an equivalent circuit of the driven rings is shown in Figure 3.6. The input impedance of Z_{in} can be written as:

$$Z_{in} = \frac{1}{sC_m + \frac{1}{\frac{1}{R_r} + s(C_r + C_m)} + \frac{1}{s(L_r + M_m)}} + R_d + \frac{1}{sC_d}, \quad (3.3)$$

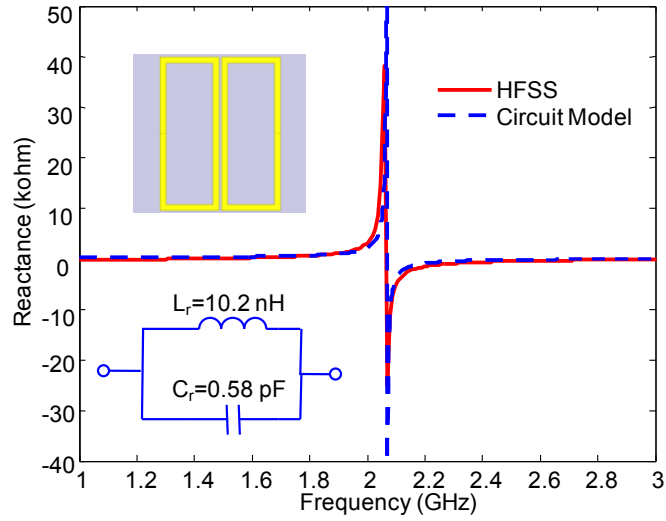


Figure 3.5 Equivalent circuit model of the D-ring is extracted from the HFSS simulation results.

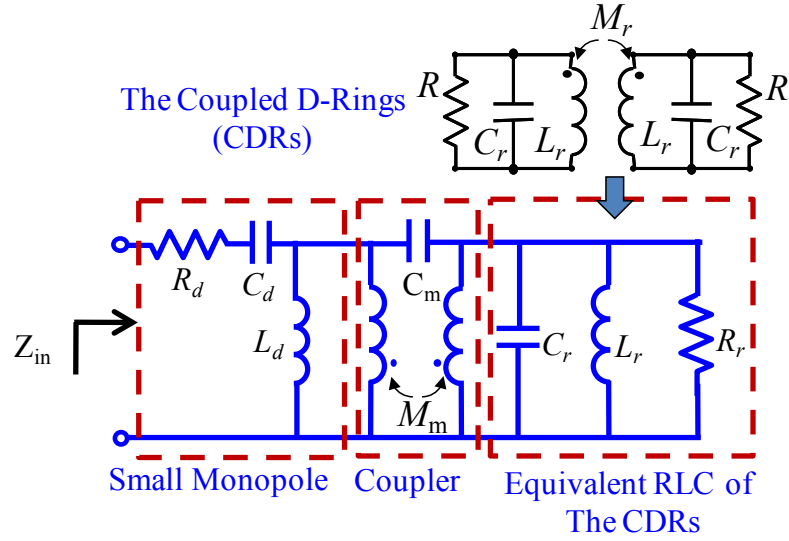


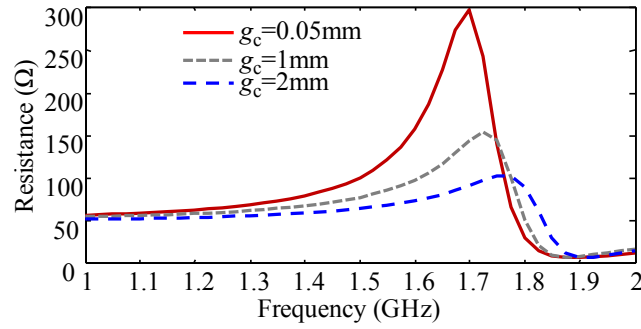
Figure 3.6 Circuit model of the CDRs and the monopole driven CDRs.

where C_m and M_m is the effective coupling capacitance and mutual inductance between the rings and monopole, and L_r , C_r , and R_r are the effective inductance, capacitance, and resistance of the rings, and R_d and C_d are the radiation resistance and capacitance of the driving monopole. Due to a very large R_r ($\sim 1300 \Omega$) under anti-resonance, it is quite challenging to realize an impedance match of the driven rings to 50Ω and more difficult to achieve a wide bandwidth. At the condition of strong coupling between the driving small monopole and CDRs, i.e., $\omega^2 C_m (L_d + M_m) > 1$, $R_d \ll R_r$, and $C_d \gg C_m$, the input resistance, i.e., the real part of Eq. (3.3), can be written as:

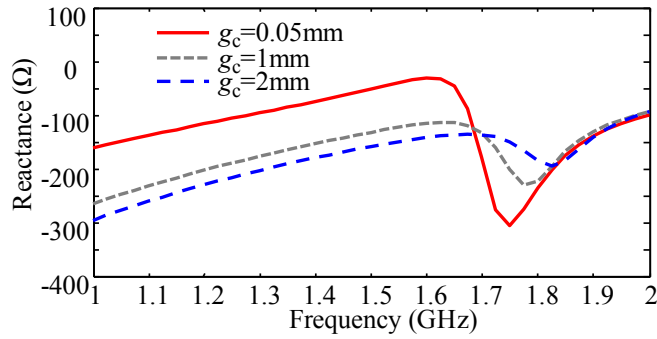
$$R_{in} \approx \frac{1}{R_r (\omega C_m)^2} \quad (3.4)$$

This is the case discussed in Section 3.2 when the CDRs are strongly coupled capacitively with the driving monopole. It is evident from Eq. (3.4) that C_m can affect the input impedance; a larger C_m produces a smaller R_{in} . Therefore, the electric

coupling actually functions as an impedance transformer. Another effect of C_m is to cause a further decrease of the resonant frequency. As we noted, f_r changed from 2.1 GHz to 1.7 GHz. Furthermore, C_m can be affected by changing the distance of g_c between the monopole and rings. Measuring R_{in} with a various g_c parameter helps find the coupling strength, or C_m .



(a)



(b)

Figure 3.7 The input impedance Z_{in} of the monopole driven D-ring with the various coupling distance of g_c : (a) real part and (b) imaginary part.

Figure 3.7 (a) shows R_{in} values when g_c is 0.05 mm, 1 mm, and 2 mm, respectively. From the figure, it is found that R_{in} decreases as g_c increases. On the other hand, from Eq. (3.4), when C_m increases, R_{in} decreases. Therefore, C_m is proportional to g_c under the strong coupling condition. However, as g_c increases

further, only the weak coupling exists between the CDRs and the monopole, therefore, R_{in} will approach R_d . Since R_d is very small, R_{in} will decrease as g_c increases. Therefore, for both the strong and weak coupling condition, R_{in} continuously decreases with an increasing g_c as indicated by Figure 3.7 (a). We will see later that such a coupling is capable of optimizing the impedance property for realizing a wider impedance bandwidth. It is noted from Figure 3.7 that the largest C_m corresponds to a g_c value of 2 mm for which R_{in} is closest to 50 Ω . However, the impedance matching cannot be achieved simply by reducing g_c since the reactance X_{in} below f_r moves to larger negative values simultaneously. The reason for this is as follows. Below f_r , the coupled rings are inductive while the driving monopole is capacitive. As g_c increases, less inductive energy exists around the monopole to compensate the capacitive energy and hence the reactance is more capacitive. A lumped inductor could be applied, but this would only achieve the impedance match at an exceedingly narrow bandwidth and also reduce the antenna efficiency. Therefore, this is not the preferable choice and the analysis below demonstrates a new technique capable of matching the impedance of the ESA to 50 Ω over a wide bandwidth.

3.3.2 Embedded Wideband Impedance Matching

There are different techniques for impedance matching [56], e.g., T-network in Figure 3.8 (a) and (b). However, for ESAs, a matching with lossless inductors and capacitors is effective over only an exceedingly small bandwidth [57]. To achieve a wideband match, I use a method whose baseline configuration is shown in Figure 3.8 (c). In the figure, a section of transmission line with a characteristic impedance of Z_m (not equal to 50 Ω) and length of L_m follows an antenna. This method is effective only

when the loci of the impedance to be matched runs clockwise on a Smith chart as frequency increases.

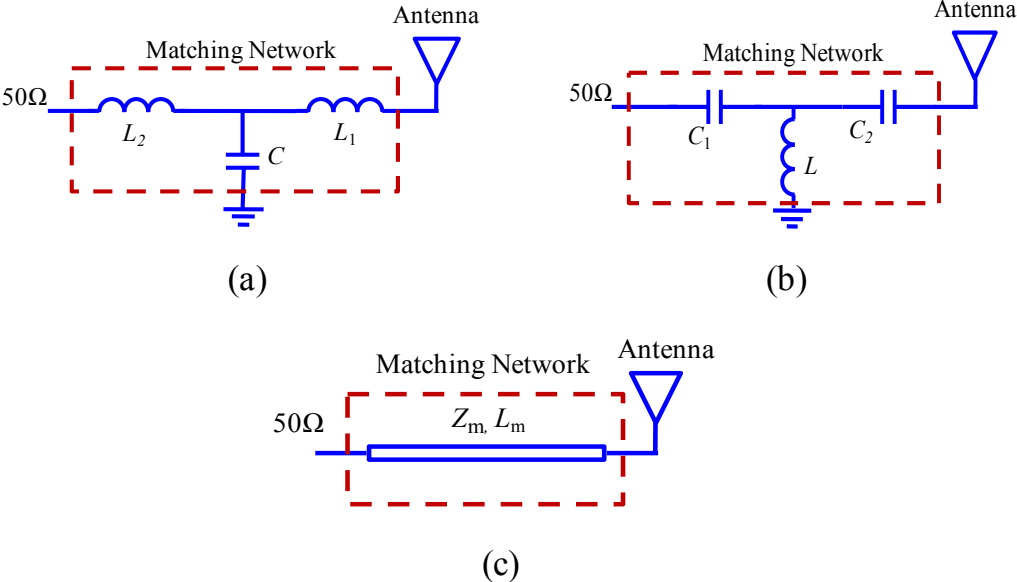


Figure 3.8 Antenna impedance matching techniques: (a) *LCL* T-network, (b) *CLC* T-network, and (c) transmission line.

For example, Figure 3.9 shows the impedance curves from Figure 3.7 in a Smith chart. In the matching process, the loci of the impedance transform are a series of concentric circles with a center of C_m located along the real axis of the Smith chart as determined by the value of Z_m . For the impedance curves corresponding to the various values of g_c , an appropriate location of C_m is likely within the area marked in Figure 3.9. The maximum bandwidth achievable is determined by the frequency range of the curve satisfying the requirement as described above. In this frequency band, the higher frequencies run a longer distance but in a faster speed, and eventually they arrive at the same final point as the lower frequencies. It is worth pointing out that in our case

the frequencies meeting the requirement must be located at the points of the “loop” of each impedance curve. Therefore, the impedance property should be optimized such that it forms a large loop in order to achieve a wideband impedance match. In Figure 3.9, the loop becomes larger as the coupling gap, g_c , decreases. Smaller g_c values mean stronger edge capacitive coupling as mentioned earlier.

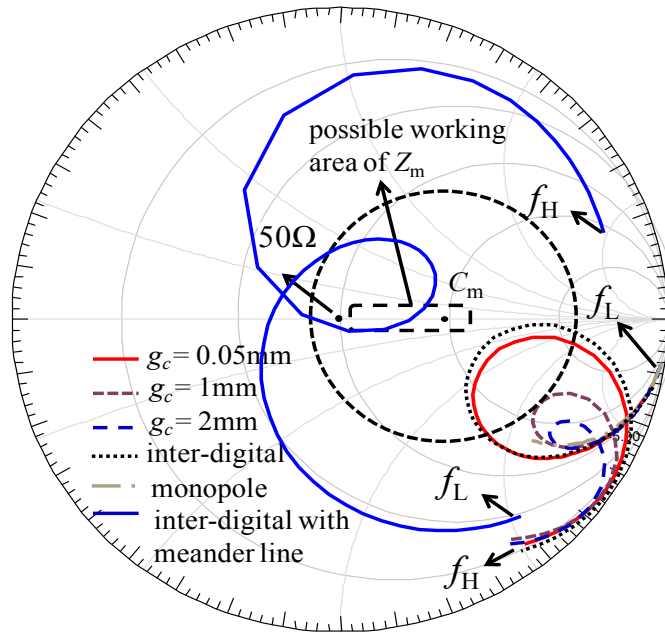


Figure 3.9 Smith chart of the impedance of the monopole driven D-ring antenna with g_c equal to 0.05 mm, 1 mm, and 2 mm, respectively, referenced to 50 Ω . In the figure, $f_L = 0.5$ GHz and $f_H = 2.0$ GHz.

Therefore, the interdigital coupler, as shown in the inset of Figure 3.10 (or Figure 3.13 without the meander line), is able to enhance the coupling where the middle and bottom strips of the rings are sandwiched by the strips of the coupler with the same spacing as g_c . The two separate strips of the coupler are connected via the bonding

wires. The input impedance curve of the antenna driven by an interdigital monopole coupler in the Smith chart is also plotted in Figure 3.9. Compared with that of the antenna driven by the monopole, the loop of the impedance of the interdigital monopole driven antenna is obviously enlarged, so a considerable improvement of the bandwidth can be achieved as will be shown later.

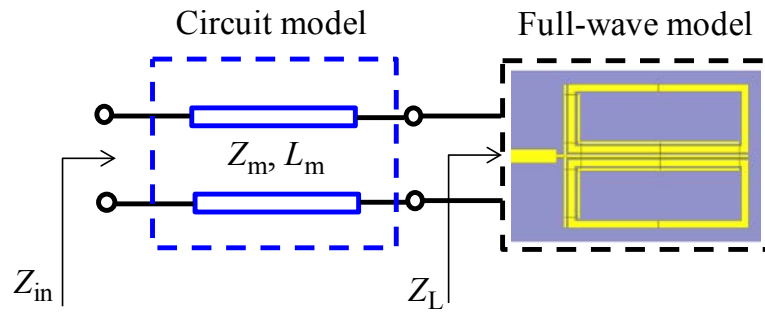
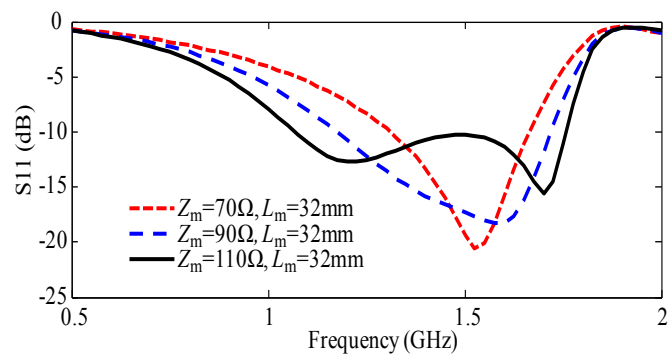


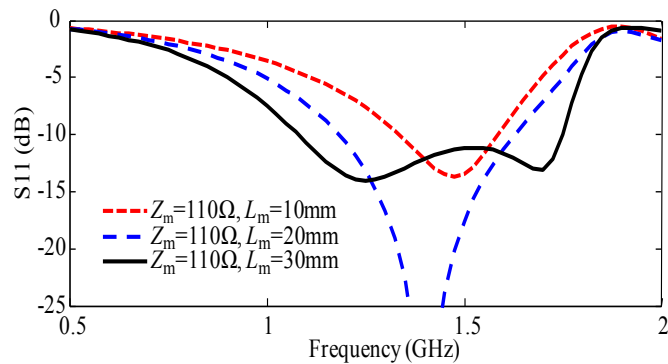
Figure 3.10 The mixed simulation model of the driven D-rings with a matching network.

The impedance Z_m and length L_m are optimized using a mixed full-wave and circuit simulation. Its configuration is shown in Figure 3.10, where the impedance of the monopole driven D-rings (with an embedded length of microstrip), i.e. Z_L , is connected to the matching transmission line whose Z_m and L_m are to be optimized for matching the input impedance of Z_{in} to 50Ω over a wide bandwidth. L_m is the physical length of any TEM transmission line in a medium of $\epsilon_r = 1$. The optimized value of Z_m and L_m can be found by performing an extensive simulation. I begin with changing Z_m while maintaining L_m at a constant value. As shown in Figure 3.11 (a), the impedance bandwidth increases as Z_m varies from 70Ω to 110Ω , with L_m equal to 32 mm . Next, I vary L_m while maintaining Z_m . From Figure 3.11 (b), it is found that L_m

equal to 30 mm provides the widest impedance bandwidth when L_m varies from 10 mm to 30 mm and Z_m is equal to 110 Ω . Therefore, the optimum bandwidth of 1.1 GHz – 1.75 GHz with $S_{11} < -10$ dB is found when Z_m and L_m are equal to 110 Ω and 30 mm, respectively. A similar procedure is also conducted for the monopole driven antenna and the optimum values of Z_m and L_m are found to be 110 Ω and 35 mm, respectively.



(a)



(b)

Figure 3.11 The simulated reflection coefficient of the interdigital coupler fed D-ring antenna with embedded matching network: (a) $L_m = 32$ mm, $Z_m = 70$ Ω , 90 Ω , and 110 Ω ; (b) $Z_m = 110$ Ω , $L_m = 10$ mm, 20 mm, and 30 mm.

Comparing the results obtained for the above two cases as shown in Figure 3.12, we can observe that a bandwidth increase in excess of 300 MHz is achieved. In addition, the simulated impedance of the interdigital monopole-driven D-ring with the meander line in Smith chart format is shown in Figure 3.9. From the figure, we can clearly see that the impedance located on the “loop” is transformed to be around the center after applying the meander line.

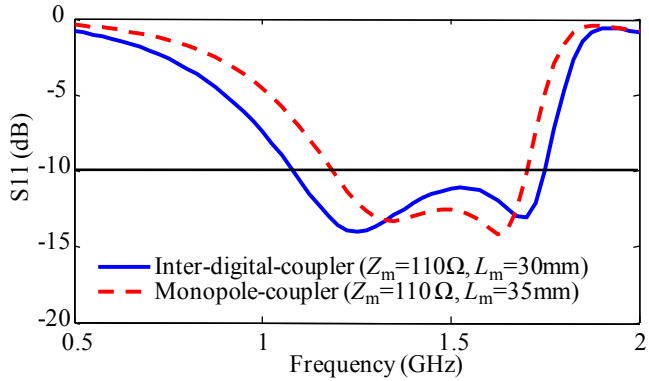


Figure 3.12 The reflection coefficient of the D-rings driven by the interdigital coupler compared with that of the monopole-coupler.

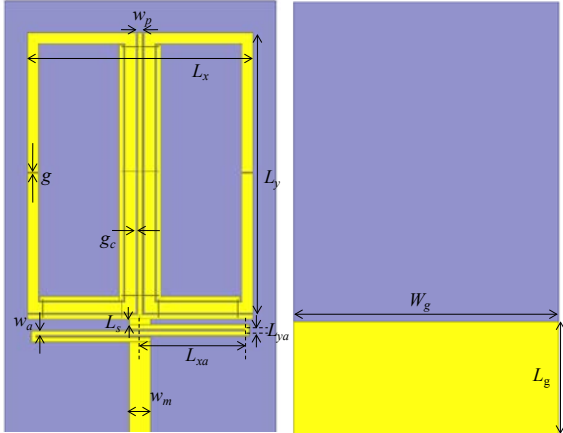


Figure 3.13 The interdigital monopole-driven D-ring antenna with meander line.

3.3.3 Ground Effect

Ground in ESAs, if smaller than $\lambda/4$, should be viewed as a part of a radiator. I investigate the ground effect of the antenna by observing the impact of ground on the return loss. To this end, I first increase the ground width from 24 mm to 40 mm while maintaining the length of 4.4 mm; then, I increase the ground length from 4.4 mm to 70 mm while maintaining the width of 24 mm. The simulated results are shown in Figure 3.14. It is observed from the figure that the resonance at the frequency of 1.7 GHz is only altered slightly; however, a notable change at 1.1 GHz occurs. The reason for this will be explained in the next section.

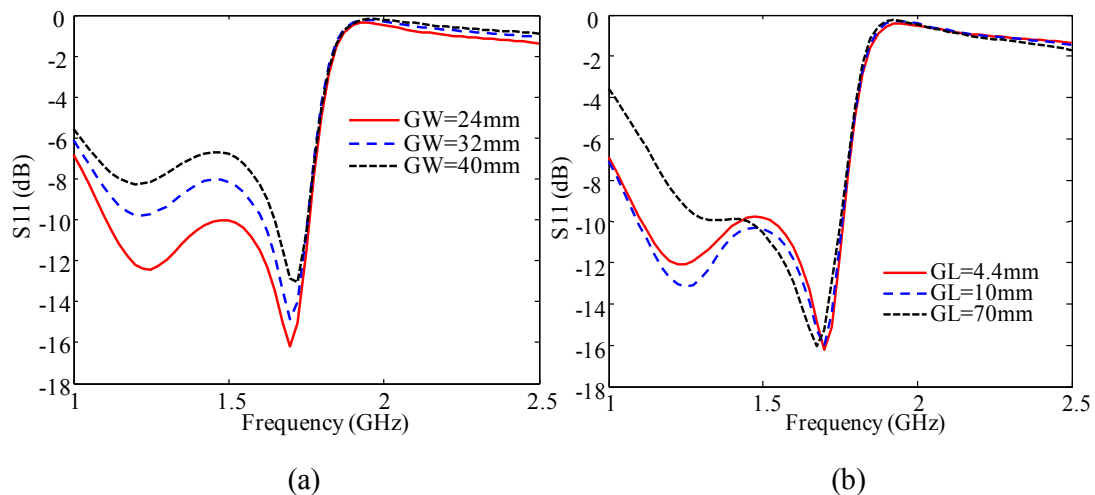


Figure 3.14 The reflection coefficient with different ground size: (a) varied ground widths of 24 mm, 32 mm, and 40 mm, while maintaining the length of 4.4 mm; (b) varied ground lengths of 4.4 mm, 10 mm, and 70 mm, while maintaining the width of 24 mm.

3.4 Results and Discussion

The antenna is fabricated using a standard lithography technique on a 25-mil-thick Rogers 5880LZ substrate with a permittivity of 2.0 and loss tangent of 0.0019.

The copper is ~ 0.7 mil thick with a conductivity of 5.8×10^7 siemens/m. The bonding wire used in the interdigital monopole is gold wire with a diameter of 1 mil. All the parameters are defined in Figure 3.13 and their values are provided in Table 3.1. Figure 3.15 shows the fabricated antenna. As seen from the figure, the bonding wires are used to inter-connect the separated strips of the interdigital monopole.

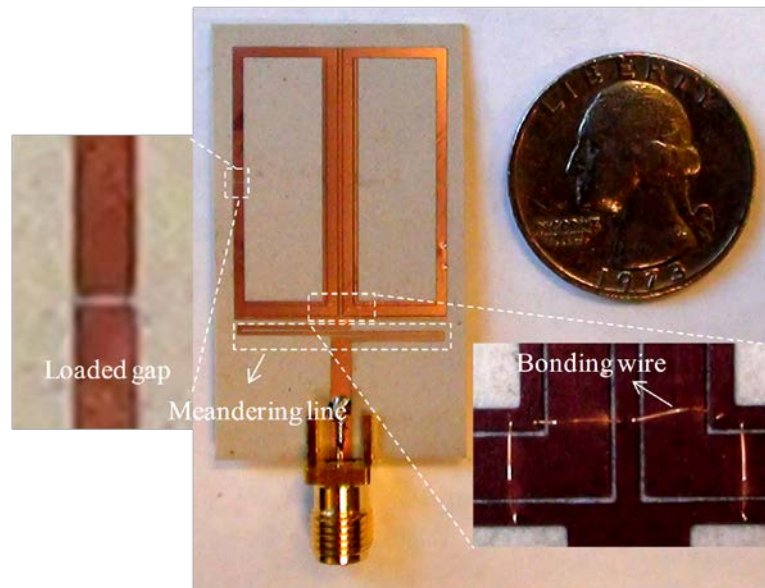


Figure 3.15 The fabricated interdigital monopole-driven D-ring ESA.

Table 3.1 Parameters of the coupled D-rings driven by the interdigital monopole (unit: mm)

g	g_c	L_s	L_x	L_{xa}	L_y	L_g
0.05	0.05	0.5	20.5	5.0	26	6.2
L_{ya}	w_a	w_m	w_p	w_r	W_g	
0.6	0.4	1.96	0.4	1.0	25.0	

Comparison of the simulated and measured reflection coefficients S_{11} is shown in Figure 3.16. The measured result is in good agreement with the simulation one. The slight shift in the resonant frequency is likely due to fabrication errors and connector

impact. From the figure, it is found that the -10-dB impedance bandwidth spans from 1 GHz to 1.7 GHz.

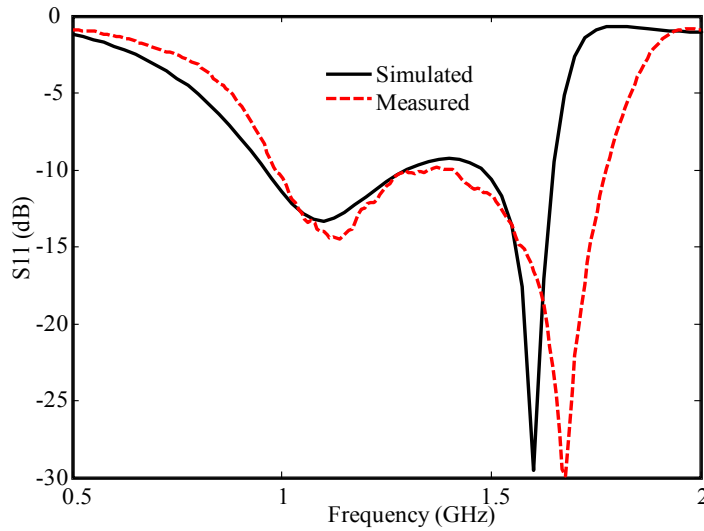


Figure 3.16 The comparison of the simulated and measured reflection coefficient.

It is noted from Figure 3.16 that the wide impedance bandwidth is attributable to the two resonances at 1.1 GHz and 1.7 GHz, respectively. First, the resonant frequency of 1.7 GHz is due to the even-mode resonance of the CDRs. This frequency deviates from 2.1 GHz because of the capacitance C_m . The monopole serves as a driving probe to excite the CDR, which is actually the major radiating part of the antenna. Another resonance at 1.1 GHz is produced by the small driving monopole whose miniaturization is owing to an embedded impedance matching circuit composed of the meandering line and D-rings acting like a distributed inductor. Moreover, such a dual-mode operation can also explain the result observed in Figure 3.14. At the low frequency around 1.1 GHz, the impedance of the antenna under monopole mode varies with the ground size. Like regular planar monopoles, ground size has a significant

impact on their impedance. However, at the high frequency around 1.7 GHz, the impedance of the antenna under the D-ring mode only changes very slightly with the different ground size. This is because under the D-ring mode the ground is not a major source of radiation. Only small changes of the impedance of the antenna with the ground width are due to the effect of mirror current induced on the ground.

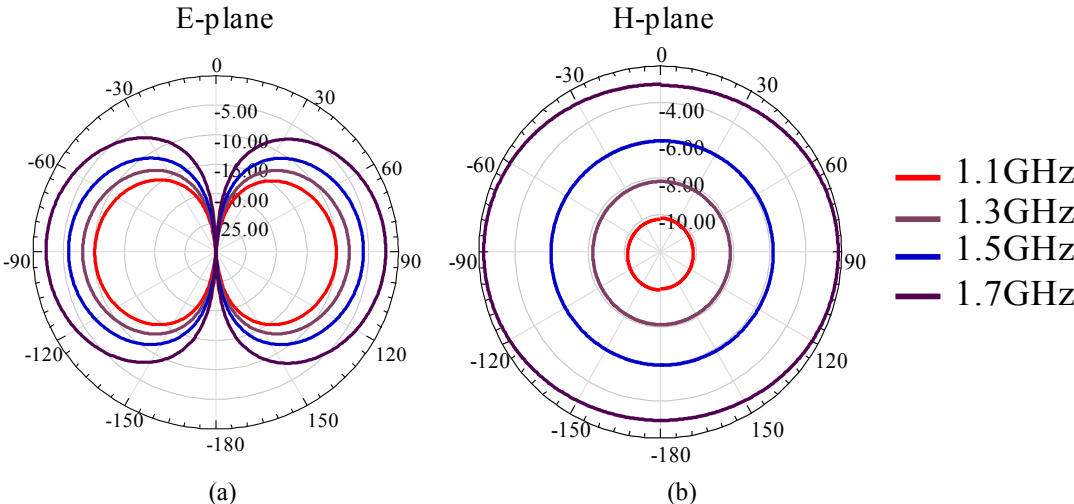


Figure 3.17 The simulated radiation patterns of E-plane and H-plane at frequencies of 1.1 GHz, 1.3 GHz, 1.5 GHz, and 1.7 GHz.

Radiation patterns, as shown in Figure 3.17, are typical “donut” shapes as we expected. This can be understood by examining the current distribution. Figure 3.18 shows the current distributions under two resonant frequencies of 1.1 GHz and 1.7 GHz. It is noted, at 1.1 GHz (called “monopole mode”), the current on the monopole is inductively coupled with that on the CDR since they are flowing in the same direction. Therefore, the antenna radiates like a dipole at the low frequency. At 1.7 GHz (called “D-ring mode”), I found that the current on the CDR are strongly excited through the capacitive coupling with the monopole, indicated by their current in an

opposite direction. Despite operating at the different modes, the antenna is able to offer stable radiation patterns. This is because the far-field radiation is always attributable to an effective current located at the inner edge of the CDR; meanwhile, the currents on the top and bottom edge of the CDR have an approximately equal magnitude but are out of phase, therefore they are not able to produce strong radiation from such a subwavelength structure. As a result, the radiation patterns are maintained similar to that of the small dipole over the whole operational bandwidth.

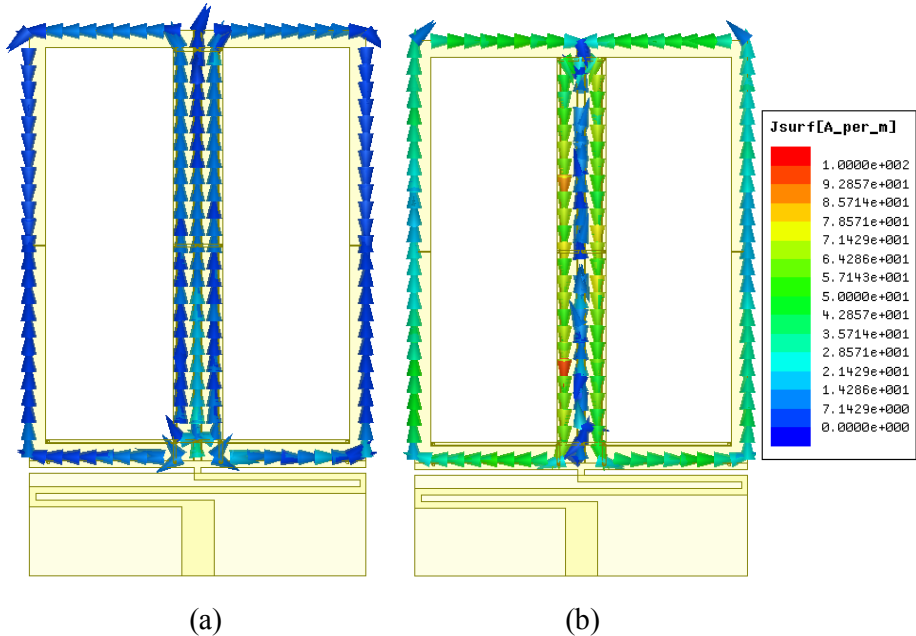


Figure 3.18 The simulated current distribution at the two resonant frequencies: (a) 1.1 GHz; (b) 1.7 GHz.

It is also observed from the figure that the gain of the antenna increases from -10 dBi to -2 dBi as the frequency increases from 1.1 GHz to 1.7 GHz, which corresponds to an increase in the antenna efficiency. The measured and simulated peak gains are shown in Figure 3.19, which are in a reasonable agreement.

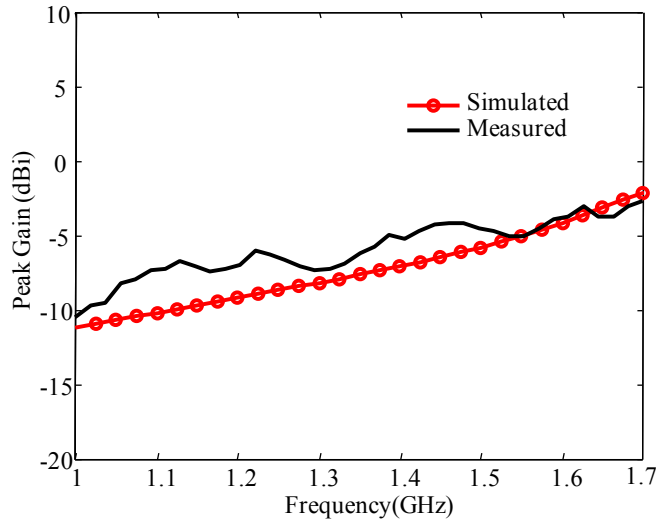


Figure 3.19 The measured and simulated peak gain.

It is well known for ESAs that a maximum product of efficiency and bandwidth is determined by the Chu limit. For the bandwidth of self-matched antennas, the maximum achievable efficiency can be obtained through the Chu limit [57]:

$$\eta = \frac{VSWR - 1}{\sqrt{VSWR}} \left(\frac{1}{ka} + \frac{1}{(ka)^3} \right)^{-1} \frac{1}{B} \quad (3.5)$$

where B is the impedance bandwidth, η is the efficiency, $VSWR$ is the voltage standing wave ratio, and a is the radius of a sphere enclosing the antenna. The radius, a , should be large enough to enclose the ground and embedded matching network because they have dimensions that are much less than the wavelength. The value of the radius, a , is calculated to be 20.58 mm and ka varies from 0.44 to 0.73 over the bandwidth. With the substitution of $a = 20.58$ mm, $B = 0.52$, and $VSWR = 2$ into Eq. (3.5), the

calculated, HFSS-predicted, and measured efficiency is shown in Figure 3.20. The simulated efficiency exceeds the Chu limit at some points because Eq. (3.5) is not rigorously accurate for an ESA with a wide bandwidth and a matching network [57]. The measured efficiency is obtained by comparing the measured peak gain of the antenna with that of a half-wavelength dipole due to their similar radiation patterns. The radiation efficiency is between 10% and 38% over the bandwidth of 1.0 GHz – 1.7 GHz, and also approaches the Chu limit. As a comparison, this proposed antenna is more preferable in terms of the product of efficiency and bandwidth than some other metamaterial antennas (e.g., [44], [49], [58], and [59]).

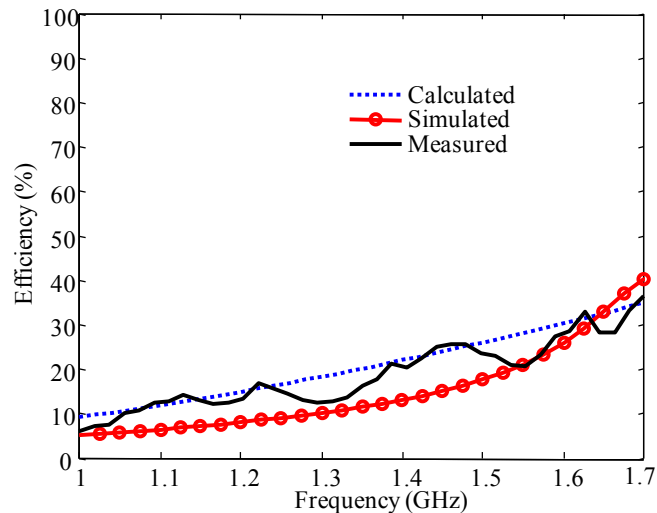


Figure 3.20 The comparison of the calculated, simulated, and measured antenna efficiency.

3.5 Summary

I present a wideband, electrically small, planar, coupled D-ring resonator antenna driven by an interdigital monopole with an embedded matching network. The wide bandwidth is attributable to the dual-mode operation of the antenna. I use an

interdigital monopole to drive the D-ring based on electric coupling. In this process, the coupling between the driving monopole and the D-ring is investigated and exploited to optimize the impedance property of the antenna which allows the antenna to achieve a wide bandwidth after a compact meandering line is applied. Based on this matching method, a dual-mode operation of the antenna is formed. In one mode, the coupled D-ring driven by the interdigital monopole acts as a major radiator resonating at the frequency of 1.7 GHz. In another mode, the driving monopole becomes a major radiator, capable of resonating at a lower frequency of 1.2 GHz due to an embedded matching network comprised of the D-ring and meandering line. As a result, the antenna can achieve an impedance bandwidth of 1 – 1.7 GHz. The predicted efficiency of the antenna is close to the Chu limit within the bandwidth. Despite the relative low efficiency, the antenna is still likely to find many applications, e.g., short-range wideband communications.

Chapter 4

OPTICALLY DRIVEN TIGHTLY COUPLED PHASED ANTENNA ARRAY

4.1 Introduction to Tightly-Coupled-Array Antennas

Tightly-coupled-array (TCA) antenna makes use of strong mutual coupling between elements, e.g., dipole, bowtie, and patch, to increase their operating bandwidth. Unlike other antenna arrays where mutual coupling is seen as a detrimental effect, TCA antennas cannot achieve wideband performance without such significant mutual coupling. To enhance mutual coupling, all of the elements in a TCA antenna can be connected or capacitively coupled. The Current Sheet [60] proposed by Wheeler in 1965 has been used as a classical model to study the performance of TCA antennas.

Figure 4.1 shows an infinite planar current sheet with current density of J , which possesses infinite impedance bandwidth. Current sheet antennas (CSAs) radiate TEM-mode electromagnetic waves towards the broadside when the current across the aperture has a constant phase. Thus, the radiation impedance of a CSA radiating at the broadside, R_0 , is half of plane-wave impedance in free space, i.e. 188Ω , due to the bidirectional radiation. When the current has a progressive phase, the radiation beam steers away from the broadside. In the two principal planes, i.e., the xoz and $yo z$ plane in Figure 4.1, the radiation modes are the TE and TM with the impedance of $R_0 \cos \theta$ and $R_0 / \cos \theta$, respectively [60]. Thus, the impedance of a CSA mainly varies with the beam direction and is independent of operating frequency. A conceptual CSA can be realized by connected-dipole arrays in which the adjacent dipoles are connected as

shown in Figure 4.2. The input impedance of connected-dipole arrays can be expressed as [17]:

$$Z_{in} = \frac{d_x}{d_y} \frac{k_0 \eta_0}{2} \sum_{m_x=-\infty}^{+\infty} \frac{\sin c^2 \left(\frac{k_{xm} t}{2} \right)}{(k_0^2 - k_{xm}^2) \sum_{m_y=-\infty}^{+\infty} \frac{J_0 \left(k_{ym} \frac{w_s}{2} \right)}{\sqrt{k_0^2 - k_{xm}^2 - k_{ym}^2}}} \approx \frac{d_x}{d_y} \frac{\eta_0}{2} \frac{\cos \theta}{1 - \sin^2 \theta \cos^2 \phi}, \quad (4.1)$$

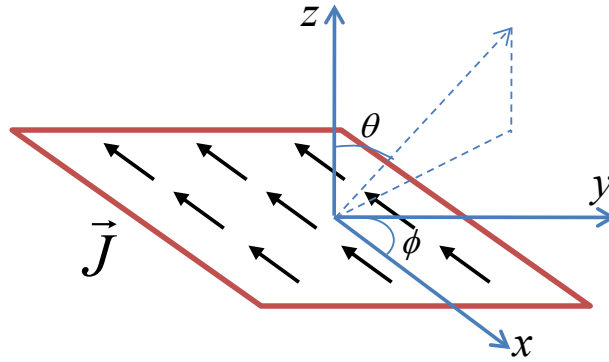


Figure 4.1 Current Sheet with the current density of \mathbf{J} . The progressive phase can steer the radiation beam to the direction of (θ, ϕ) .

in which d_x and d_y are spatial period in the x and y direction, η_0 is free-space wave impedance, w_s and t are the width and thickness of the dipoles, k_{xm} and k_{ym} are the x and y component of the wave number of the m -th Floquet mode, k_0 is the wave number in free space. It is noted that if the array is only operated at the fundamental mode, i.e. $m = 0$, the input impedance becomes consistent with that of an infinite current sheet when d_x is equal to d_y . In addition, similar to the CSA case, this impedance is only a function of the beam direction rather than the frequency, thus exhibiting an infinite

relative bandwidth. The approximation in Eq. (4.1) is valid for low frequencies since under small arguments the Bessel function and the *sinc* function tend to be one. Therefore, to satisfy this condition, the dipoles should be much smaller than the wavelength at the operational frequencies. Correspondingly, the length of the dipole is chosen as half a wavelength at the high end of an operating bandwidth to avoid the emergence of grating lobes, and thus at the low frequencies, the dipole becomes electrically small.

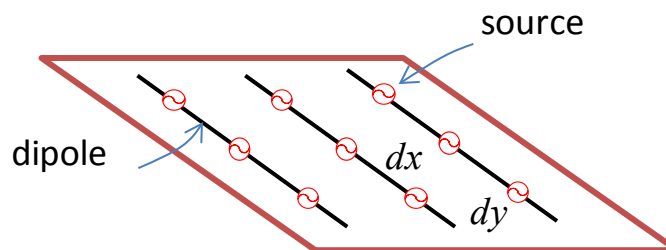


Figure 4.2 Connected-dipole arrays are a realistic form of conceptual current sheet antennas. Each dipole is spaced in the period of d_x and d_y which are much smaller than the wavelength in its operational bandwidth.

In many applications, a ground plane is desired by connected-dipole arrays to isolate the elementary antennas from spurious effects of a feed network. The loading effect of a ground plane periodically changes the input impedance of elementary antennas over a given frequency range. The circuit model of a CSA in free space is compared with that of the same CSA located above a ground plane in Figure 4.3. In the circuit model, the RF source drives two parallel transmission lines with characteristic impedance of 377Ω . The transmission line terminated by the ground plane is shorted when the source is above the ground plane with a distance of half a wavelength. As a result, the bandwidth is restricted by the presence of a ground plane.

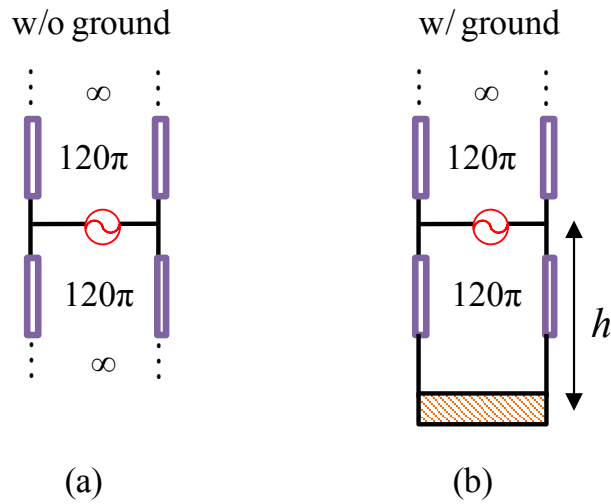


Figure 4.3 The equivalent circuit of connected-dipole arrays: (a) without a ground plane and (b) with a ground plane.

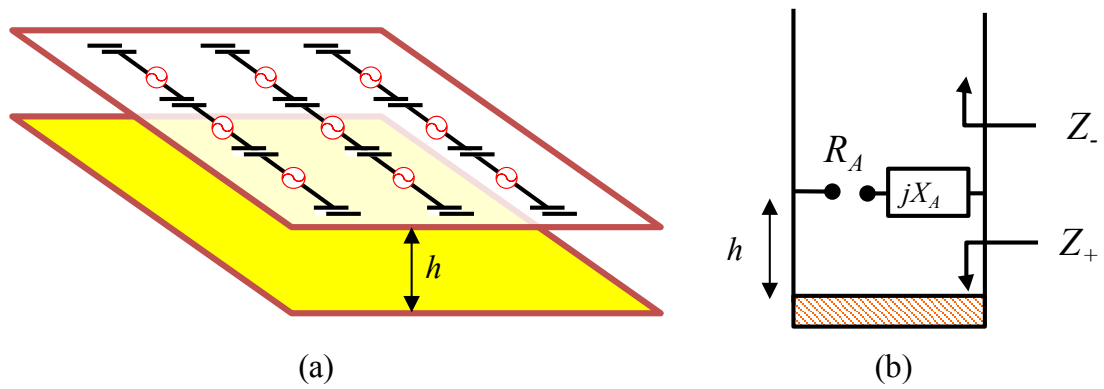


Figure 4.4 (a) Tightly coupled dipole arrays with a ground plane, (b) equivalent circuit.

In order to increase the operational bandwidth of connected-dipole arrays at the presence of ground plane, Prof. Munk [10] introduced strong capacitive coupling to the adjacent dipoles as illustrated by Figure 4.4 (a). Hence, this array is named as tightly coupled dipole antennas. The use of strong capacitive coupling attempts to

cancel the inductance caused by the ground plane. In its equivalent circuit, jX_A ($X_A < 0$) represents the mutual coupling capacitance which acts as a part of the impedance matching circuit. With this method, a bandwidth of 4.5:1 has been achieved [10]. In addition, a superstrate and a resistive FSS can be applied to further improve bandwidth up to 21:1 [13].

The concept of CSAs have been developed into a variety of forms which are generally named as TCA antennas. Tremendous effort has been made to address efficient excitation of a TCA antenna in an ultra-wide bandwidth. In the next section, I revisit some of the most popular electrical feeding schemes and discuss technical difficulties in them.

4.2 Electrical Excitation of TCA Antennas

4.2.1 Balanced Feed

A TCA is comprised of a large number of elementary antennas which usually have symmetric forms such as dipole and bowtie. When each elementary antenna is fed by symmetric transmission lines, the currents induced on two arms of a dipole are equal in magnitude and opposite in phase (called balanced feed). However, if fed by coaxial cables, the currents will become unbalanced, which results in impedance instability and high cross-polarization. Additionally, TCA antennas normally have a high input impedance difficult to match with their feeding transmission lines typically with a characteristic impedance of 50 Ω . To realize a balanced feed as well as an impedance match, a balanced-to-unbalanced transformer, i.e., balun, is used by each element. However, baluns can impose additional restrictions on the performance of a TCA, such as the bandwidth, operational frequency, weight and profile.

Assembled and integrated baluns have been studied to be used in electrical feeding for efficient excitation of a TCA. Wideband passive baluns typically have high insertion loss and are only available at sub-gigahertz frequencies. Active baluns are mainly unidirectional as well as incapable of handling high RF powers, hence not suitable for transmit applications. Figure 4.5 shows an electrical feeding using an external balun, which is capable of converting CPW to stripline and transforming impedance from $50\ \Omega$ to $200\ \Omega$. However, this balun only operates at a frequency up to 600 MHz and has the insertion loss as high as 3 dB [61].

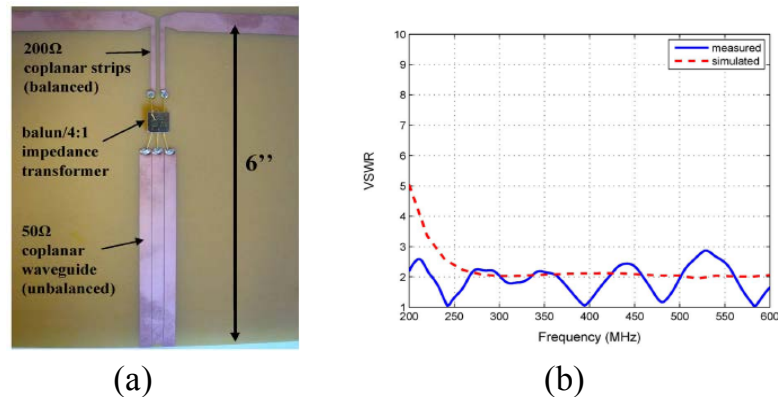


Figure 4.5 (a) The electrical feed of a TCA implemented with an external balun, and (b) the result of VSWR, from [61], © 2013 IEEE.

Alternatively, integrated baluns can be applied to the electrical feeding of TCA antennas, offering distinct features such as compact dimension, low insertion loss, and high operational frequency. Integrated baluns are required to be simultaneously designed along with a TCA, which they are used to feed. However, a large fractional bandwidth still cannot be achieved due to many additional restrictions imposed by the baluns from the design and fabrication process. In Figure 4.6 [16], each dipole is fed

by a ring hybrid serving as a balun. This antenna that is assisted by a superstrate load has an operational bandwidth of 8 – 12 GHz when $VSWR < 2$. Although relatively high operating frequencies are achieved, this antenna still suffers from a narrow bandwidth due to the use of the ring-hybrids.

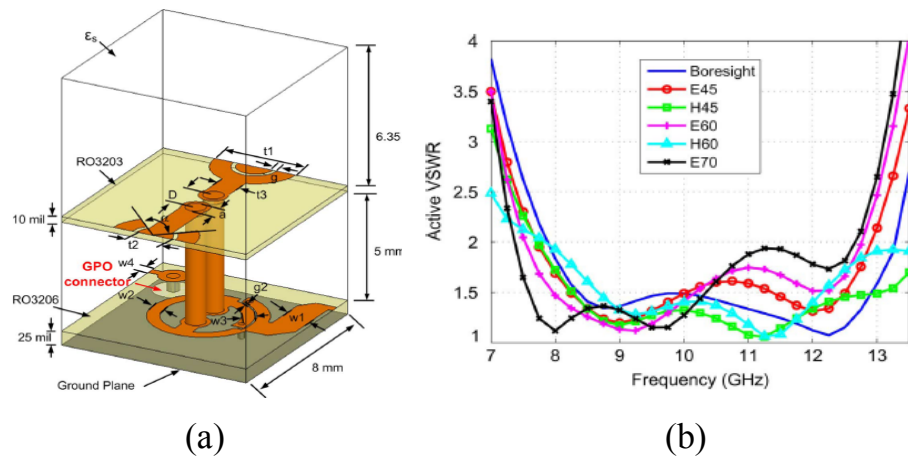


Figure 4.6 (a) The electrical feed of a TCA is implemented with a hybrid integrated balun, and (b) results of VSWR, from [16], © 2013 IEEE.

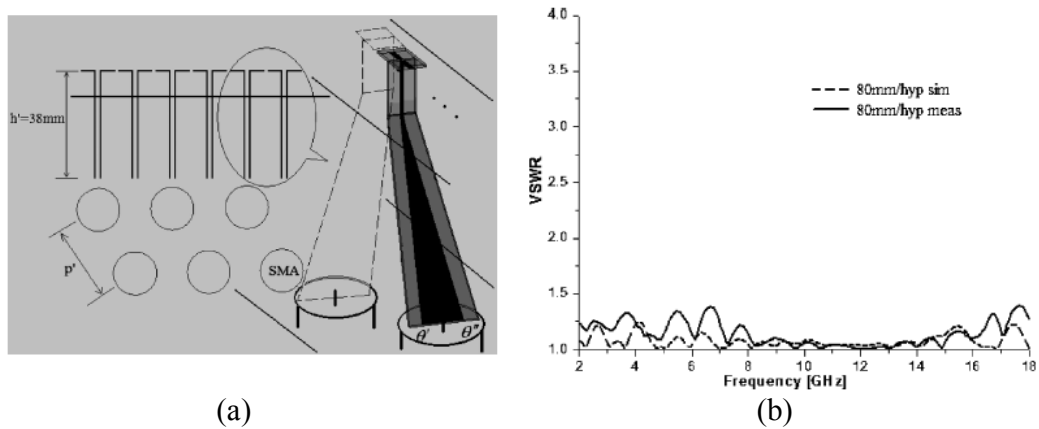


Figure 4.7 The wideband balun using microstrip-to-stripline transition with a tapered ground (a) and VSWR (b), from [62], © 2009 IEEE.

Figure 4.7 shows another UWB balun for which microstrips are transformed to striplines with a slowly tapered ground [62]. In this way, an operational bandwidth of several octaves can be achieved. However, this balun has to be bulked up as long as multiple wavelengths at the high end of a desired operational bandwidth. Therefore, it is not suitable for TCA antennas comprised of subwavelength elements to operate at high gigahertz frequencies.

4.2.2 Unbalanced Feed

Baluns are required to avoid spurious radiation of unbalanced feeding transmission lines that feed TCA antennas. In other words, the absence of baluns can result in anomalous responses. Figure 4.8 (a) shows current distribution when the connected-dipole array is fed by coaxial cables underneath a ground plane. From the figure, it is noted that the current excited on the two arms of dipoles is unbalanced.

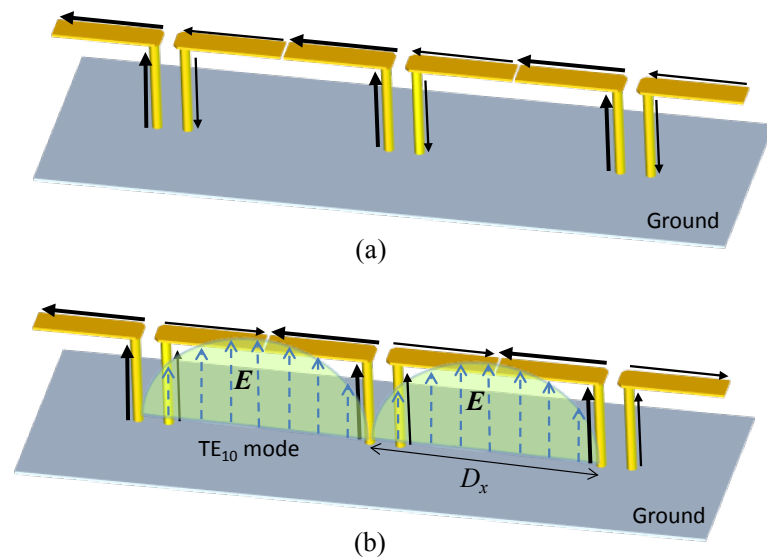


Figure 4.8 (a) An unbalanced feed (the arrow line represents excited current), (b) TE₁₀-mode resonance caused by an unbalanced feed (the solid lines represent excited current, the dotted lines represent electric field).

As seen in Figure 4.8 (b), two cavities are formed by the arms of the dipoles, the protruding feed lines, and the ground plane. The net current in the vertical direction can excite multiple cavity modes. The resonant frequency of TE₁₀ mode resides in the desired operating bandwidth free of grating lobes. When the cavities resonate, the current excited on the feed lines becomes in phase, thereby producing strong spurious radiation that has a polarization normal to the ground plane. This situation is called common-mode resonance. The current and electric field of TE₁₀ mode are plotted in Figure 4.8 (b). For a planar two-dimensional TCA array, the fundamental common-mode resonant frequency can be estimated by [63]:

$$f_{cm} \approx \frac{c_0}{2\sqrt{\epsilon_{eff}} \sqrt{D_x^2 + D_y^2}} \quad (4.2)$$

where D_x and D_y are the period in the x , y direction, and ϵ_{eff} is effective dielectric constant. Calculated from Eq. (4.2), the frequency f_{cm} is nearly located at the middle of an operational bandwidth. Therefore, this anomaly frequency must be eliminated. To this end, metal pins are used to connect each dipole and the ground plane [63]. As a result, the common-mode resonance is relocated and will occur at a frequency about twice higher than the original resonant frequency. Using this method, a TCA allows to be directly driven by coaxial cables and has achieved an operational bandwidth of 7 – 21 GHz [16].

4.2.3 Scan Blindness

Scan blindness near 46° in the E plane is found in a regular dipole array due to the presence of vertical feeding transmission lines [64]. When the radiation beam is steered off the broadside, each vertical feed line radiates like a monopole. This

spurious radiation is called “monopole radiation” that tends to cancel out the desired radiation of the dipoles. This scan blindness occurs in the direction when the dipole radiation is canceled by the monopole radiation. To alleviate it, metal walls can be added in the H-plane to suppress the monopole radiation by isolating the feed lines.

Likewise, TCA antennas need to address similar problems as well. To suppress spurious monopole radiations, feed organizers as shown in Figure 4.9 are used for shielding the feed lines of a TCA. Each feed organizer groups two pairs of coaxial cables through four holes to feed one elementary radiator of a dual-polarized TCA. However, the use of these feed organizers precludes planar fabrication and modularity of TCA antennas. In addition, tight mechanical tolerance of the fabrication restricts the feed organizers only suitable for low-frequency applications [16].

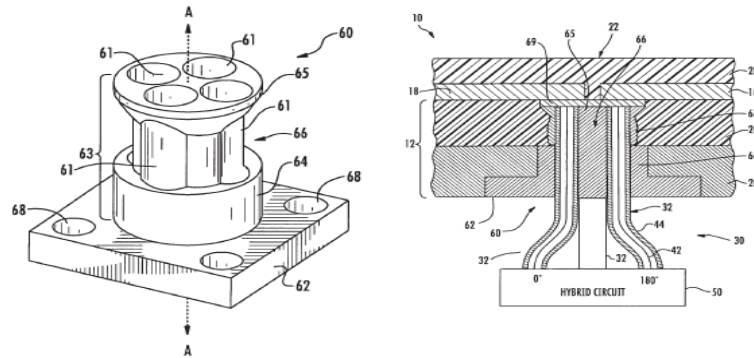


Figure 4.9 Feed organizers for a dual-polarization CSA antenna, from [10], © 2007 IEEE.

4.3 Optical Excitation of TCA Antennas

4.3.1 Concept of Photodiode-Coupled Antennas

In the proposed optical addressed phased array transmitter architecture, transmitting signals need to be transformed between the optical domain and electrical

domain, respectively, using EO modulators and photodiodes. RF signals generated from a relative low frequency source are upconverted into the multiple sidebands of an optical carrier signal. This modulated optical signal can be remotely imparted to photodiodes via optical fibers. Desired RF signals are recovered by photomixing at photodiodes, and are transmitted by antennas. In each frontend module of the transmitter, the photodiode is ideally directly integrated with the radiator. As such, each element of the transmitter is allowed to be driven via an optical fiber instead of a RF transmission line. The use of this optical feeding scheme into TCA antennas circumvents many challenges incurred by the electrical feeding schemes as discussed previously. This is due to the absence of feeding RF lines and baluns. The optical feeding scheme can eliminate the scan blindness while maintaining the operational bandwidth, light weight, and low profile aspects of TCA antennas. In addition, this optical feeding scheme is applicable to TCA antennas that operate up into the mm-wave regime.

To apply the optical feeding scheme to an optically addressed phased array, RF power amplifiers regularly used in conventional transmitters to meet radiation power requirements must be eliminated. Therefore, high-power and high-speed photodiodes become an essential component. Fortunately, tremendous progress has been made in the development of these photodiodes, in recent years. Figure 4.10 shows a chart that summarizes the performance of the photodiodes from the published literature for comparison. Various versions of modified untraveling-carrier (MUTC) photodiodes [65], labeled as “MUTC4” and “MUTC5”, have demonstrated both higher speed and output power than the other designs. From the figure, MUTC4 photodiodes have 15-GHz 3-dB bandwidth and 1-W saturation power, and MUTC5 photodiodes have 65-

GHz 3-dB bandwidth and 38-mW saturation power. As a result, a TCA consisting of a great number of the elementary radiators that are integrated with these high-power photodiodes can transmit enormous RF power sufficient for various applications.

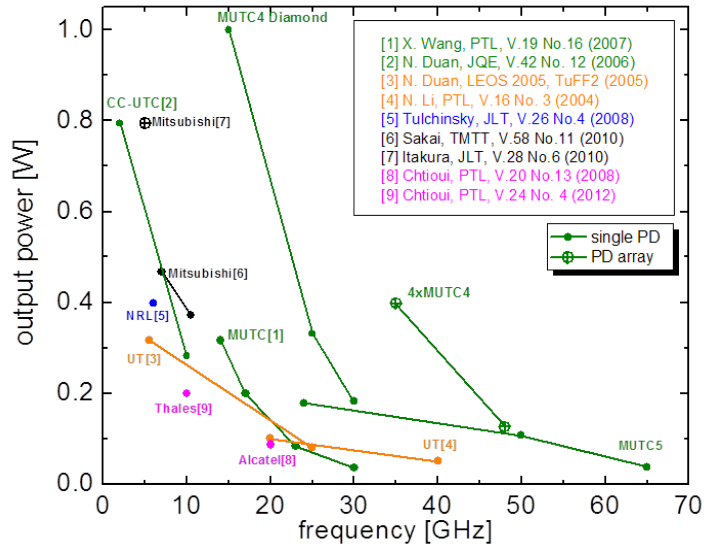


Figure 4.10 A survey on status of development of high-power photodiodes. The output power of 1 W has been achieved by the MUTC4 photodiodes on diamond substrate with an operational bandwidth of 22 GHz. The output power of 38 mW has been achieved by the MUTC5 photodiodes with an operational bandwidth of 65 GHz. Figure courtesy of Prof. Joe Campbell, University of Virginia.

4.3.2 Analysis of Photodiode-Coupled TCA Antennas

4.3.2.1 Circuit Model

As illustrated in Figure 4.11, the dipoles in a connected-dipole array are excited by the photodiodes that are spaced from each other by a distance of d_x and d_y along the x - and y -axis. Each photodiode serves as a source equivalent to an ideal current source I_{ph} in parallel with a capacitance C_{ph} . I_{ph} is the photocurrent generated

by photomixing two optical signals with the frequency of ω_1 and ω_2 , the power of P_1 and P_2 , and the phase of φ_1 and φ_2 . I_{ph} can be derived as:

$$I_{ph} = \Re \sqrt{2P_1P_2} h(\omega) e^{j(\omega_{RF}t + \varphi_{RF})} \quad (4.3)$$

where $\omega_{RF} = \omega_1 - \omega_2$ and $\varphi_{RF} = \varphi_1 - \varphi_2$ are the radian frequency and the phase of the RF photocurrent, \Re is the responsivity of photodiode, $h(\omega)$ is the frequency response of the photodiode. The capacitance of C_{ph} can be extracted by $h(\omega)$ as:

$$C_{ph} \approx 1/100\pi B_{ph} \quad (4.4)$$

in which B_{ph} is the 3-dB corner frequency of $h(\omega)$ when the photodiode is loaded by a 50- Ω resistor.

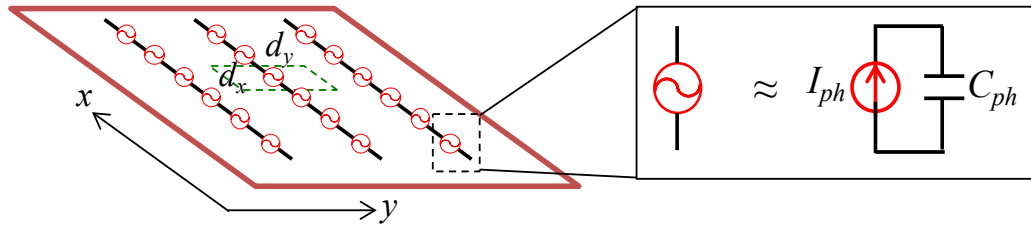


Figure 4.11 A photodiode-coupled TCA representation comprising of connected dipoles each of which is driven by a photodiode. A photodiode can be simply equivalent to a current source in parallel with a capacitance.

In a photodiode-coupled TCA, each radiating element acts as a dynamic load of photodiodes and therefore imposes direct impact on the performance of a TCA. To expedite the analysis, an infinite \times infinite two-dimensional array, with uniform amplitude and phase excitation, is considered. Under this condition, a unit cell is sufficient to represent an entire periodic array that can approximate a large-scale array.

The top view of a unit cell is shown in Figure 4.12 (a) where periodic boundary conditions (PBC) truncate its four side walls, and absorbing boundary conditions (ABC) terminate the left and right wall of the air box, as shown in Figure 4.12 (b). Lumped and current ports provided by HFSS will be utilized in subsequent analyses. The use of lumped port in simulations can offer the active input impedance and admittance of driving antennas. Lumped port impedance is not allowed to be set too high for mimicking current sources. In contrast, a current port is similar to a current source that has infinite impedance. The effect of port impedance on the active input impedance of a TCA is first investigated.

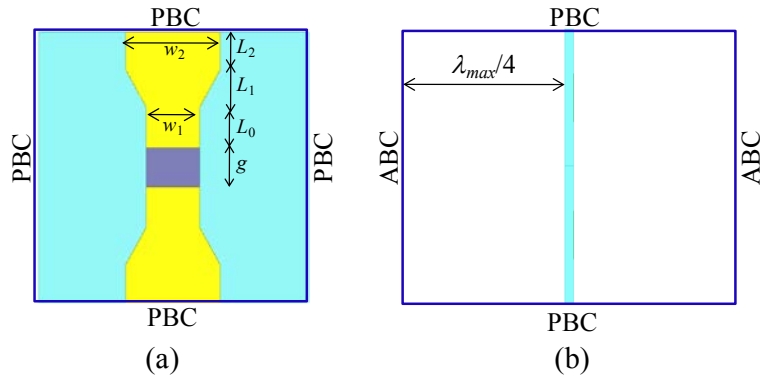


Figure 4.12 The simulation configuration of an infinite connected dipole array. The parameters are chosen as $w_1 = 1.4\text{mm}$, $w_2 = 2.5\text{mm}$, $L_0 = 1.05\text{mm}$, $L_1 = 1\text{mm}$, $L_2 = 1\text{mm}$, $g = 1.04\text{mm}$. ABC is located at least a quarter-wavelength of the lowest simulation frequency. (a) Topview, and (b) sideview.

It is expected that the active input impedance is not susceptible to the source impedance. In the simulation, the TCA is driven by a current port (with infinite impedance) as well as a lumped port with various port impedances of $50\ \Omega$, $200\ \Omega$, $500\ \Omega$, and $1\ \text{K}\Omega$, respectively. The active input resistance R_{in} of a TCA excited by current sources can be obtained by:

$$R_{in} = 2P_r / I_g^2, \quad (4.5)$$

in which I_g is the amplitude of source current and P_r is the radiation power from the antenna.

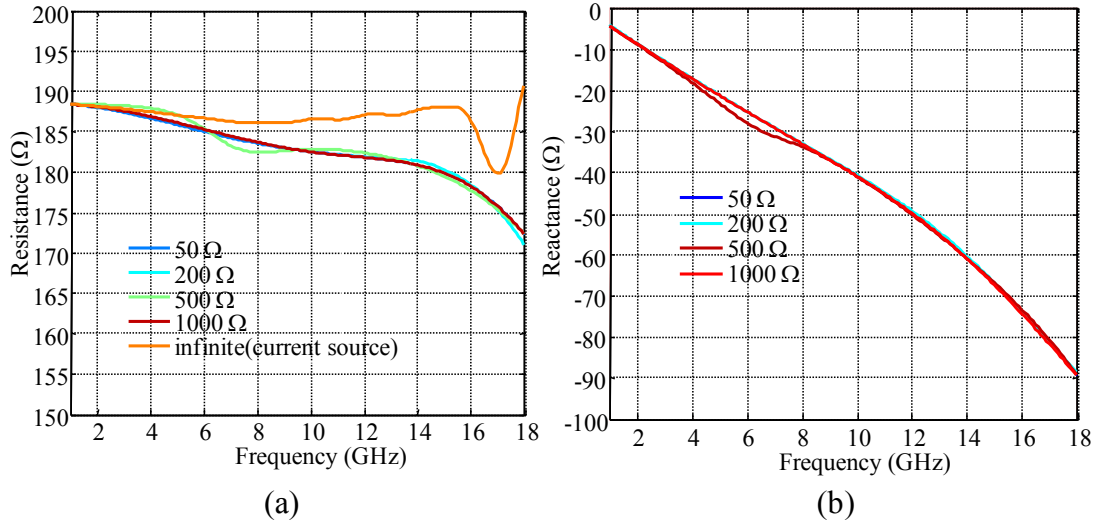


Figure 4.13 Simulated impedances of the connected dipole array fed by a lumped port with various port impedances (50 Ω, 200 Ω, 500 Ω, and 1 KΩ), and a current port with infinite impedance. (a) Resistance, and (b) reactance.

As shown in Figure 4.13 (a), the simulated active resistance does not vary appreciably as the port impedance. The resistance obtained from the lumped-port excitation only slightly decreases from 188 Ω to 170 Ω as the frequency increases. In comparison, the resistance obtained from the current source excitation has a nearly constant value of 188 Ω. Figure 4.13 (b) shows the capacitive reactance that can be extracted from the simulation. The equivalent circuit as shown in Figure 4.14 is sufficient to represent the TCA over an ultra-wide bandwidth, It is comprised of a

resistance R_{TCA} in parallel with a capacitance C_{TCA} , both nearly independent of the operating frequency and source impedance.

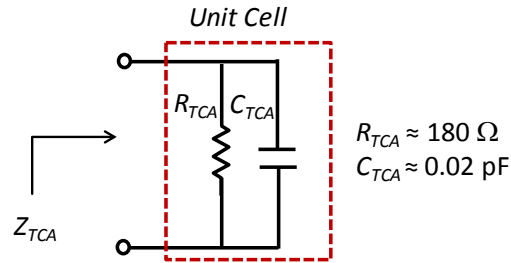


Figure 4.14 Wideband equivalent circuit model of the TCA in Figure 4.12.

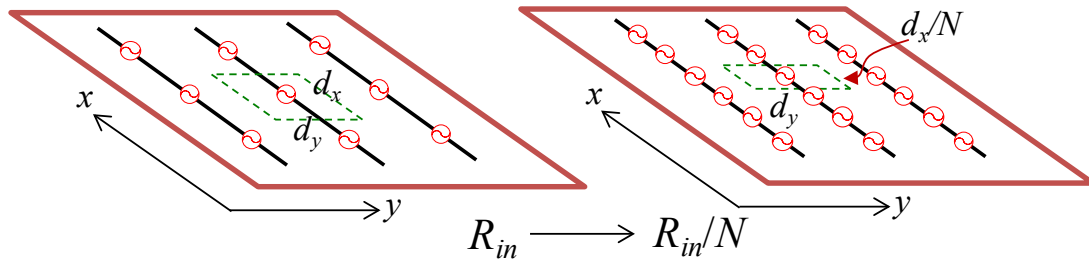


Figure 4.15 The impedance of a TCA reduces by N times when the SR ratio of the E-plane to the H-plane increases by N times. d_x and d_y are the spatial periodicities of the excitation sources along the x and y axis, respectively.

In addition, the active impedances of TCA antennas depend on the spatial sampling rate (SR) of their excitations. Here, a SR is defined as the number of driving sources per wavelength at the high end of an operating bandwidth. Eq. (4.1) clearly shows that the active impedance has nearly constant real values when the $SR > 2$. The resistance is inversely proportional to the ratio of the SR in the E-plane (xoz) to that in the H-plane (yoz). For example, as shown in Figure 4.15, when the SR in the E-plane

increases by N times while it remains unchanged in the H-plane, the active impedance will decrease by N times. As a result, a high ratio of the SR in the E-plane to the H-plane can reduce the input impedance, which helps an impedance match for electrically fed TCA antennas or increases the operational bandwidth of optically fed TCA antennas as will be discussed later. In the following analysis, the SR only refers the sample rate in the E-plane, since the SR in the H-plane has a fixed value of two.

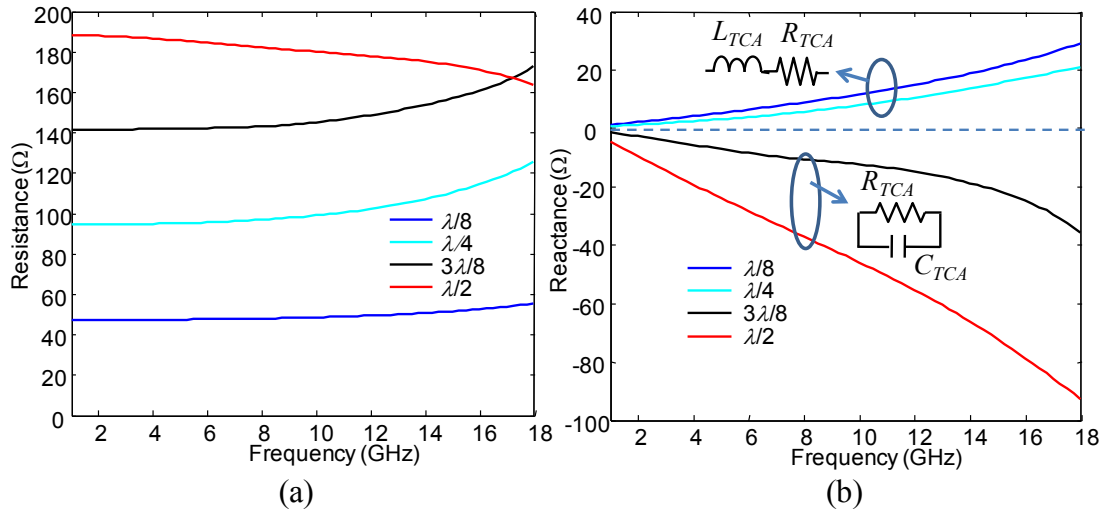


Figure 4.16 Simulated input impedances versus SR. The SR in the E-plane is 2, 8/3, 4, and 8 while the SR of 2 maintains in the H-plane. (a) Resistance, and (b) reactance.

To study the impact of the SR on the antenna characteristics, the simulation model in Figure 4.12 is still applicable, except that all the dimensions along the x axis need to be scaled for various SR values. The dimensions along the x -axis are decreased by the factors of 4/3, 2, and 4. In other words, the spatial periodicity is $3\lambda/8$, $\lambda/4$, and $\lambda/8$, or the SR is 8/3, 4, and 8. The simulated active impedance is shown in Figure 4.16. It is observed that the active impedance varies with SR, i.e., active

resistance decreases as SR increases, and active reactance transits from capacitive values to inductive values as SR increases. Therefore, a general equivalent circuit of photodiode-coupled TCA antennas has two forms contingent on different SRs. As shown in Figure 4.17, a TCA can be equivalently represented by a parallel RC circuit at a low SR, while represented by a series RL circuit at a high SR.

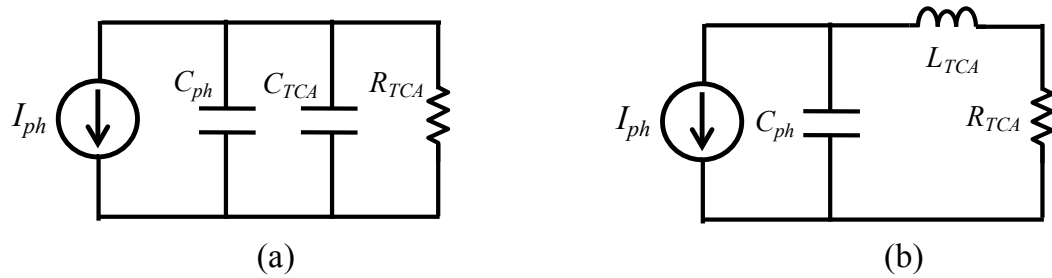


Figure 4.17 The equivalent circuit models of a photodiode-coupled TCA. (a) TCA antennas with a low SR, (b) TCA antennas with a high SR. Neither of them takes into account the losses from the photodiode and antenna.

4.3.2.2 Performance of Photodiode-Coupled TCA Antennas

The performance of a photodiode-coupled TCA can be evaluated in terms of bandwidth, power efficiency, and radiation gain. Analyses will be conducted based on a low-SR model applicable to the situation faced in Chapter 6. Similar analyses can also be conducted based on a high-SR model, which thus will not be repeated here.

Figure 4.18 shows the schematic of a photodiode-coupled antenna with bias circuitry. The voltage of V_{bias} provides reversed voltage bias through an inductor serving as an RF choke. A two-tone optical signal with the frequency of ω_1 and ω_2 , and the phase of φ_1 and φ_2 , is incident into a photodiode. The current I_{ph} , generated by photomixing, can drive an antenna to radiate RF power. Based on the circuit model as shown in Figure 4.17 (a), the radiation power P_r from an antenna can be expressed as:

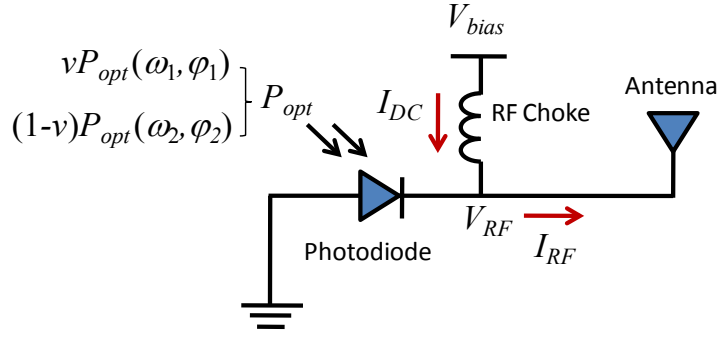


Figure 4.18 The circuit representation of a photodiode-coupled antenna includes the bias circuit. A two-tone optical signal is incident on a photodiode producing a RF signal of I_{RF} .

$$P_r(\omega) = \frac{I_{ph}^2 R_{TCA}}{1 + [R_{TCA}(C_{ph} + C_{TCA})]^2} \quad (4.6)$$

The operational bandwidth (BW) is defined as the frequency f_c at which P_r is rolled off by 3 dB from its maximum. From Eq. (4.6), the frequency of f_c is expressed as:

$$BW = f_c = \frac{1}{2\pi R_{TCA}(C_{ph} + C_{TCA})} \quad (4.7)$$

The radiation power in the BW is approximated as:

$$P_{r\max} = I_{ph}^2 R_{TCA} \quad (4.8)$$

It is a trade-off between P_r and BW , i.e., higher impedance increases radiation power but decreases BW . Additionally, BW is inversely proportional to total capacitance exhibited for the photodiode. The ratio of $BW \cdot P_r$ product over the square of photocurrent is a fair figure of merit to evaluate photodiode-coupled TCAs, which can be written as:

$$\frac{BW \cdot P_{r \max}}{I_{ph}^2} = \frac{1}{2\pi(C_{ph} + C_{TCA})}. \quad (4.9)$$

This value is mainly determined by the total capacitance of the photodiode and TCA.

Power efficiency is another important parameter for evaluating photodiode-coupled TCA antennas. The power efficiency η is defined by a ratio of the radiation power to total power consumption consisting of the optical power P_{opt} coupled into a photodiode and dissipation power P_{dc} in the photodiode. η can be expressed as:

$$\eta = \frac{P_r}{P_{opt} + P_{dc}}, \quad (4.10)$$

in which P_{dc} can be calculated as multiplying the bias voltage by the photocurrent. To calculate P_r , assume a two-tone optical signal consisting of the frequency of ω_1 and ω_2 , and the power of νP_{opt} and $(1-\nu)P_{opt}$, respectively for each tone, is incident into the photodiode as shown in Figure 4.18. From Eq. (4.3) and Eq. (4.6), and $h(\omega) \approx 1$, the radiation power can be expressed as:

$$P_r(\omega) \approx \frac{2\nu(1-\nu)h^2(\omega)\Re^2 P_{opt} R_{TCA}}{1 + [R_{TCA}(C_{ph} + C_{TCA})]^2}. \quad (4.11)$$

The maximum radiation power can be achieved when the two tones have an equal power, i.e., $\nu = 0.5$. In addition, to ensure a linear operation, the photodiode must have a bias voltage larger than $V_{bias, min}$:

$$V_{bias, min} \approx \sqrt{2} I_{ph} R_{TCA}. \quad (4.12)$$

Under this condition, the power dissipated in the photodiode can be estimated as:

$$P_{DC} \approx \sqrt{2} \Re P_{opt} I_{ph} R_{TCA}. \quad (4.13)$$

Substituting Eq. (4.11) - Eq. (4.13) into Eq. (4.10), the efficiency is obtained as:

$$\eta \approx \frac{\frac{1}{2} \Re^2 h^2(\omega) P_{opt} R_{TCA}}{\Re^2 h^2(\omega) P_{opt} R_{TCA} + 1}. \quad (4.14)$$

From Eq. (4.14), we can observe that η increases as P_{opt} , \Re , and R_{TCA} . If $\Re \approx 1$, $h(\omega) \approx 1$, and $P_{opt} R_{TCA} \gg 1$, η approaches the maximum value of 0.5, which is the theoretical limit of efficiency of a photodiode-coupled TCA. Moreover, the gain of a TCA under a uniform excitation can be estimated as:

$$G_{TCA} \approx \frac{4\pi A}{\lambda^2}, \quad (4.15)$$

in which A is the physical area of a TCA aperture and λ is the operational wavelength.

4.3.3 Design of Photodiode-Coupled TCA Antennas

4.3.3.1 Radiation Bandwidth

Some useful techniques to improve bandwidth of photodiode-coupled TCAs will be studied in this section. According to Eq. (4.7), the bandwidth is determined by $R_{TCA}(C_{ph}+C_{TCA})$. The smaller capacitance of C_{ph} can offer a larger bandwidth. On the other hand, the capacitance C_{TCA} , if much larger than C_{ph} , can become dominant in determining the bandwidth. The parametric study is performed to obtain the optimized design as shown in Figure 4.12 with the minimized capacitance of C_{TCA} . In this design, C_{TCA} is only about 0.02 pF, thereby not serving as a crucial factor in determining the bandwidth. In fact, the parasitic capacitances produced in the process of integrating photodiodes with a TCA are dominant terms in the total capacitance.

Moreover, high resistance of R_{TCA} can restrict the bandwidth of a TCA as well. To mitigate this restriction, SR can be increased to reduce R_{TCA} . As shown in Figure 4.16, R_{TCA} decreases in a similar rate as SR increases. Increasing SR offers another benefit in that it can simultaneously reduce C_{TCA} . It is worth pointing out that SR does not change the radiation power density when the optical power incident into a TCA is provided. This is because when SR increases, the number of elementary antennas of a TCA increases correspondingly. Nevertheless, the radiation power of each antenna decreases as the radiation resistance of the TCA when SR increases. As a result, the total radiation power is determined by the physical aperture size of a TCA and the optical power incident into the photodiodes. As illustrated in Figure 4.19, no matter SR is two or four, the TCA has a radiation power density of S :

$$S = P_r / dx dy \quad (4.16)$$

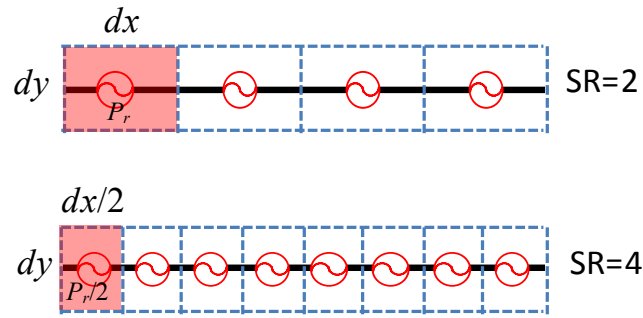


Figure 4.19 The radiation power density of a TCA when the SR is equal to 2 and 4.

where P_r is given by Eq. (4.8). The use of higher SR can offer a larger bandwidth while maintaining the density of radiation power. Increasing SR also raises the cost and power consumption of a photodiode-coupled TCA.

Another method to increase bandwidth without changing SR is to intentionally introduce little ohmic (thermal) loss into each radiator of a TCA. Thermal loss can be added by using external chip resistors in parallel with photodiodes. The simulation model is shown in Figure 4.20. In the figure, the external resistor with resistance of R_{ext} is above the source port (light blue) and across the two arms of the dipole. The equivalent resistance of R_{loss} is added to modify the equivalent circuit in Figure 4.14. R_{loss} represents the thermal loss due to the power dissipation in the external resistor. We should be aware that R_{loss} is not necessarily equal to R_{ext} , and these two resistances can be related with a first-order approximation:

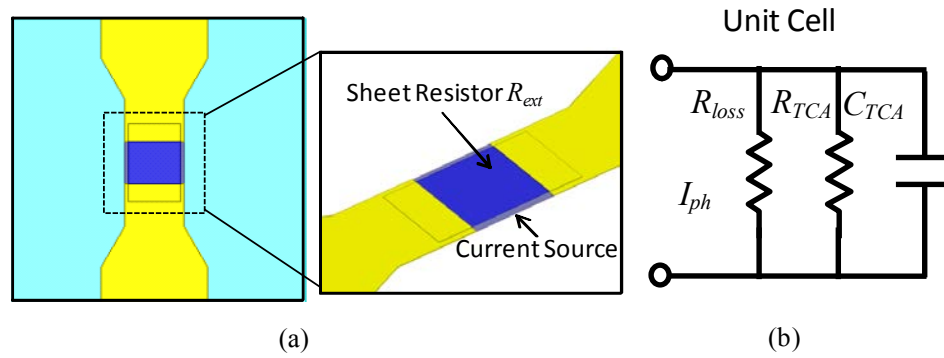


Figure 4.20 (a) The HFSS simulation model of a TCA with an external resistor (top) and the driving port (bottom) and (b) the equivalent circuit. The dimensions of this model are given in Figure 4.12.

$$R_{loss} \approx \alpha R_{ext}, \quad (4.17)$$

in which the coefficient of α is constant and can be extracted from the full-wave simulation result in Figure 4.21 (a). It turns out that α is about 0.73. Thus, the input resistance of the TCA is:

$$R_{in} = \frac{\alpha R_{rad} R_{ext}}{R_{rad} + \alpha R_{ext}}. \quad (4.18)$$

To improve the accuracy of this relation, the radiation power is respectively calculated by a full-wave simulation and circuit analysis. Figure 4.21 (a) offers the values of R_{loss} that corresponds to the value of R_{ext} from 50 Ω to 500 Ω . Figure 4.21 (b) demonstrates the results from the both methods are in a good agreement. Insertion loss (IL) caused by the additive external resistance can be estimated from R_{TCA} and R_{loss} as:

$$IL = -10 \log \left(1 + \frac{R_{TCA}}{R_{loss}} \right). \quad (4.19)$$

A low IL is desired such that the efficiency is not significantly compromised.

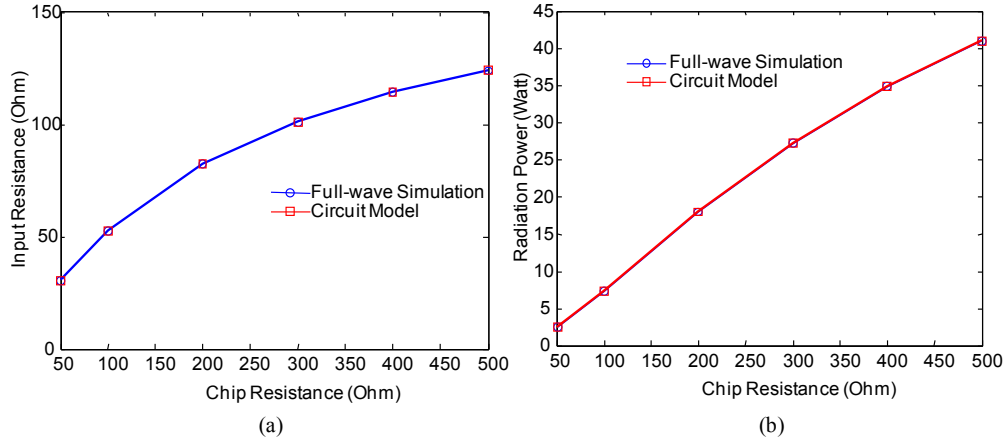


Figure 4.21 (a) Input resistance and (b) radiation power versus the applied external resistance calculated from the full-wave simulation and equivalent circuit model.

In addition, the bandwidth of a photodiode-coupled TCA can be increased by inductive peaking. For example, in a low-SR model ($SR < 4$), a TCA can be approximated by an RC circuit. The inductive peaking can effectively boost the

bandwidth without increasing the number of photodiodes and insertion loss of a TCA antenna, as detailed in the next section. However, there is a bandwidth limit governed by the Bode theory [66]. Photodiode-coupled TCA antennas with high-order peaking circuitry usually are too complicated to practically implement. Therefore, the first and second-order peaking circuits are normally employed.

4.3.3.2 Photodiode Biasing Network

A photodiode-coupled TCA antenna needs many bias lines for all the photodiodes. Ideally, only DC current is allowed to flow on these bias lines and zero RF current. In reality, since each radiator is electrically small, bias lines impose loading effect on each radiator of a TCA. Therefore, the bias line must be analyzed together with the other parts of a TCA. I found a kind of radiation blindness due to bias networks, which differs with the scan blindness as discussed in Section 4.2.3.

Such radiation blindness should be eliminated from the desired operational bandwidth. To this end, two rules are useful in designing the bias lines, in order to achieve minimizing electromagnetic coupling between the bias lines and primary radiators in addition to relocating anomalous frequencies. First, the contact of bias lines with each radiator should be placed where the RF current is weak. As the second rule, the bias lines within a unit cell should be shorter than half a wavelength at the high end of an operational bandwidth:

$$L_b \leq \frac{\lambda_{\min}}{2\sqrt{\frac{\epsilon_r + 1}{2}}}, \quad (4.20)$$

in which L_b is the length of a bias line, λ_{\min} is the wavelength at the high end of an operational bandwidth, and ϵ_r is the effective dielectric constant. The above rules are applied to the example in Section 4.3.4.

4.3.3.3 Concerns in Integration Process

A photodiode-coupled TCA requires the photodiodes to be integrated with its elementary antennas and feeding optical fibers. An integration process introduces parasitic reactance leading to the reduction of an ideal operational bandwidth. Several sources of parasitic reactance are identified as follows. When a photodiode is attached to a TCA antenna, the height mismatch between the substrate of antenna and photodiode can produce parasitic capacitance. In addition, flip-chip or wire bonding, if applicable, can produce parasitic inductance. The dielectric components, e.g., optical fiber ferrules, can produce parasitic reactance as well. Hence, the impact of an integration process must be accounted in a full-wave modeling in order to obtain precise simulation results.

4.3.4 A Design Example: 12-GHz-Bandwidth TCA (Connected-Dipole) Antenna

4.3.4.1 Infinite TCA Antenna

As shown in Figure 4.22 (a), the connected-dipole array is designed on a 20-mil Rogers 4350 substrate with dielectric constant ϵ_r of 3.66. The photodiode in the simulation is modeled according to Albis PDCS24L with 20-GHz bandwidth [67]. This photodiode is made of 4-mil InGaAs/InP substrate with ϵ_r of 12.9, and is flip-chip bonded on a 4-mil ceramic substrate with ϵ_r of 9.8 as a submount. The simulation model consists of dipole, photodiode, flip-chip and wire bonding, and ceramic submount. The input impedance is expected to be about 188Ω since $SR = 2$, in a good

agreement with the simulation as shown in Figure 4.22 (b). In addition, to investigate the integration impact, the simulation result is compared with the calculated result based on the ideal circuit model in Figure 4.14. The operational bandwidth can be indicated by the input resistance when the photodiode is excited by a current source. As illustrated by the simulation result in Figure 4.22, the integration process can cause the bandwidth reduction by about 2 GHz.

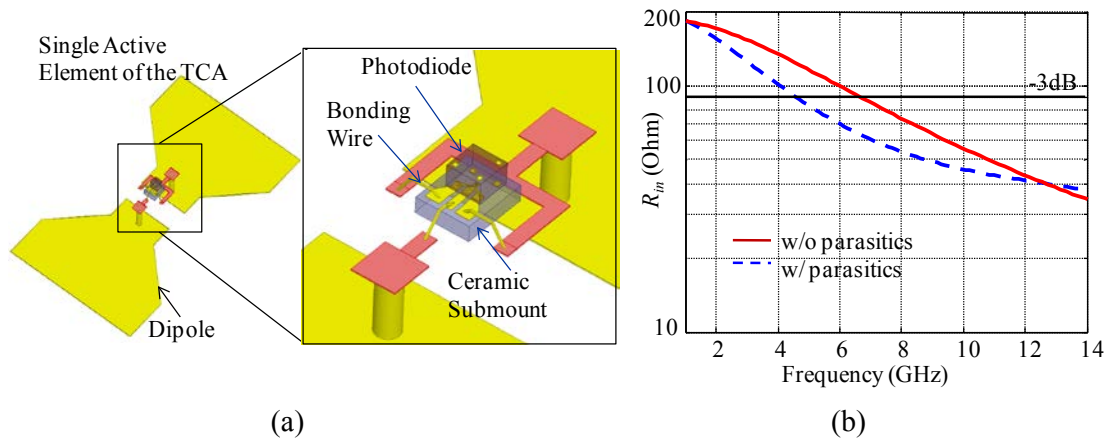


Figure 4.22 (a) The HFSS model of a photodiode-coupled TCA. (b) Simulated frequency responses of the input resistance and ideal frequency response without the integration effect.

The bandwidth can be improved by applying an inductive peaking. To do this, a spiral inductor and an interdigital capacitor are added to the prior model as shown in Figure 4.23 (a), and the equivalent circuit that takes into account the peaking and integration effect, as shown in Figure 4.23 (c). The equivalent circuit can be understood as follows. When the series resistance of R_s (a few ohms) and parallel resistance of R_l ($\sim 1 \text{ G}\Omega$) is ignored, the photodiode is approximated by a current source of I_{ph} in parallel with the capacitances consisting of both the photodiode C_{Dep}

and bonding pads C_{Pad} . Additionally, short tapered CPW transmission lines on the submount are modeled as two cascaded LC ladder circuits. The TCA is modeled as a parallel RC circuit. Moreover, L_p is the inductance of the spiral inductor that is used for inductive peaking, and C_p is the capacitance of the interdigital capacitor used for tuning the peaking frequency. The precise realization of C_p and L_p is accomplished by performing extensive parametric studies. As shown in Figure 4.23 (b), the TCA with the inductive peaking circuitry achieves an operational frequency from DC to 8 GHz below which there is a ripple of 2.55 dB. Thus, this bandwidth is about two times larger than that without the inductive peaking.

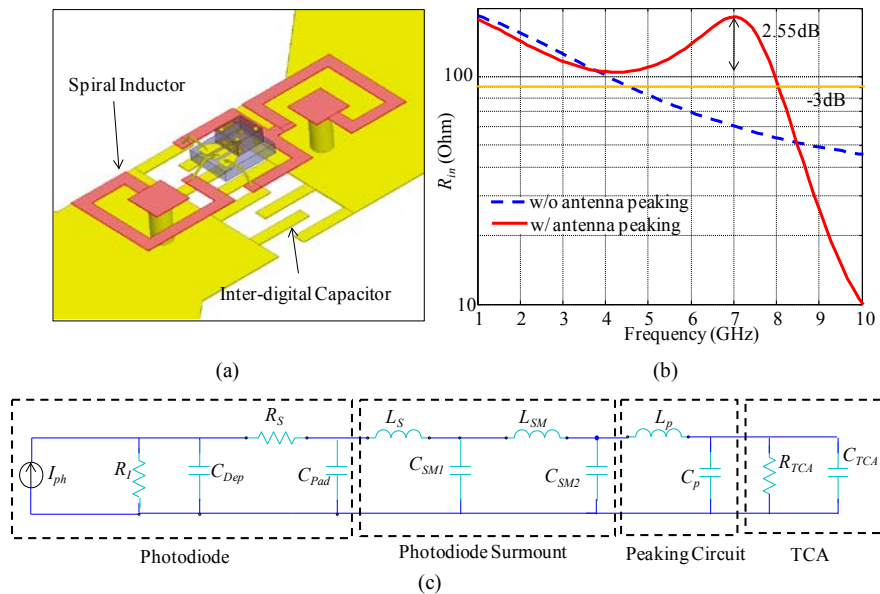


Figure 4.23 (a) HFSS simulation model (b) simulated frequency response of the input resistance before and after inductive peaking (c) equivalent circuit of a TCA integrated with photodiodes with an inductive-peaking circuit.

Alternatively, a larger operational bandwidth can be achieved at the cost of radiation efficiency. To introduce additional losses, high-frequency 221- Ω chip

resistors as shown in Figure 4.24 (a) are placed across the two arms of each dipole. Its HFSS simulation model includes the bias lines and integration components (e.g., ferrules and spacers) as well as the chip resistor.

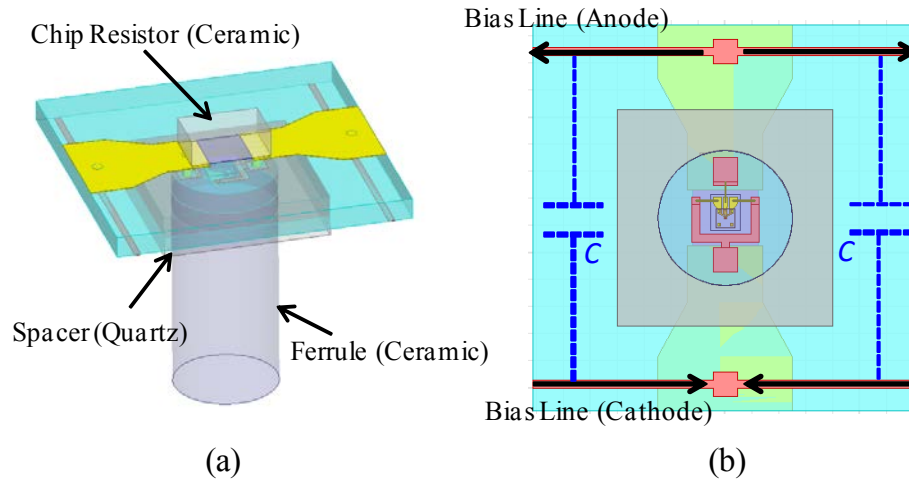


Figure 4.24 (a) HFSS model of the photodiode-coupled TCA incorporating of bias lines and integration components (ferrules and spacers) and (b) illustration of the coupling effect of the bias lines which could cause the radiation blindness.

To investigate the impact of the bias lines, the input impedance of this TCA with the bias lines as shown in Figure 4.25 is compared with the same model without the bias lines as shown in Figure 4.26. From the comparison, the radiation blindness is noticed to occur at the frequency of about 13 GHz due to the presence of the bias lines. This anomalous frequency can be understood as follows. As illustrated in Figure 4.24 (b), the bias lines at both sides of the dipole can be viewed as a transmission line since the RF currents on them are approximately out of the phase. When the length of the bias lines is quarter wavelength, the input impedance exhibited at the contact of the bias lines with the dipole is approaching zero, i.e., the radiation resistance is shorted.

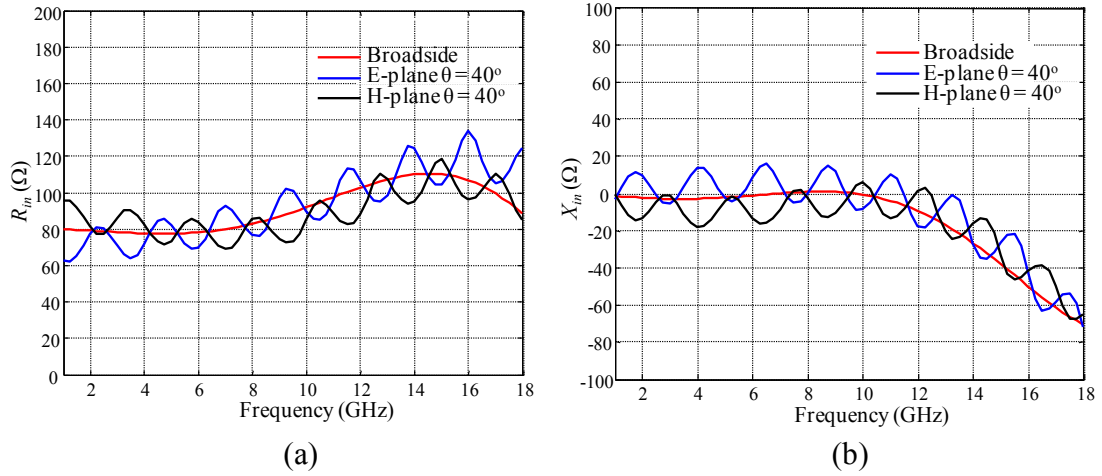


Figure 4.25 Input impedance of the TCA when bias lines are not included: (a) resistance and (b) reactance.

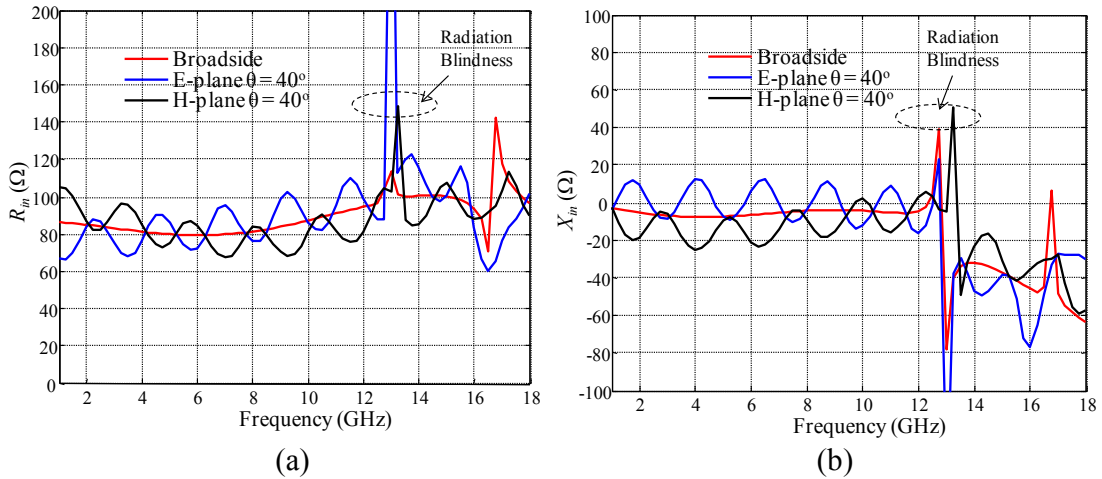


Figure 4.26 Input impedance of the TCA when the bias lines are present: (a) resistance and (b) reactance. The radiation blindness occurs at about 13 GHz due to the bias lines.

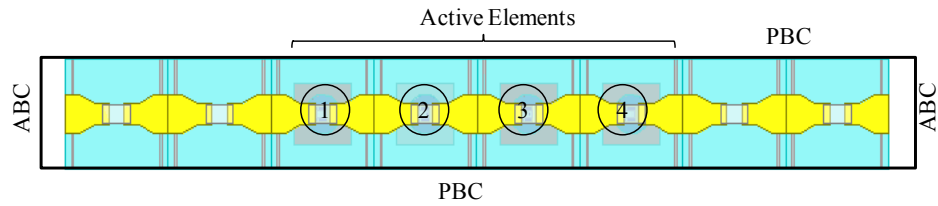
At the frequency less than 12 GHz, the bias line seems to impose slight impact on the input impedance, which exhibits multiple common properties as follows. The input resistance slightly varies between 80 Ω and 100 Ω , while the input reactance is about zero. Additionally, when the radiation beam is steered off the broadside, the input

impedance varies in the range of $\pm 20 \Omega$. Since the low cut-off frequency does not exist, the TCA is assumed to possess an infinite bandwidth and operates up to 12 GHz.

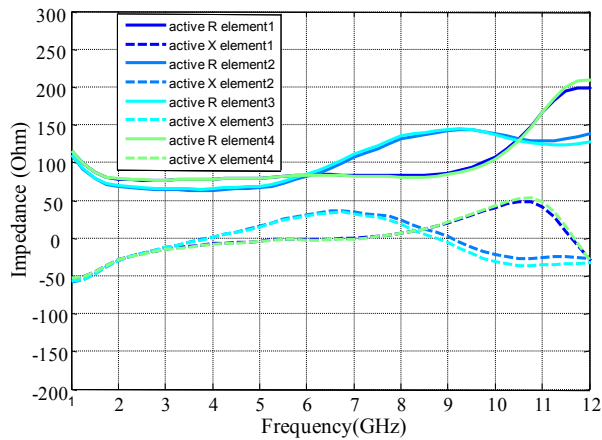
4.3.4.2 Finite \times Infinite TCA Antenna

Four active elements embedded in an 8×8 finite array are used for a system prototype demonstration in Chapter 6. This finite TCA antenna needs to be analyzed for the estimation of its performance. The complete HFSS model of this finite array requires an extremely large computer memory, which currently is not affordable. To investigate edge-truncation effect, this array in the E-plane as shown in Figure 4.27 (a) is studied. In the simulation model, the top and bottom sides are truncated by PBC boundaries to emulate the infinite dimension in the H-plane, while ABC boundaries terminate the left and right sides of the air box. The active elements are labeled in the figure. Each of the dummy elements are loaded by a $50\text{-}\Omega$ chip resistor to minimize the current reflection due to the truncated array.

Figure 4.27 (b) shows the simulated active impedance of each active element. It is observed from the figure that the impedances of #2 and #3 antenna have a larger variation than those of #1 and #4 antenna. This is due to the resistor loaded on each dummy element that can partially absorb the stored energy of its adjacent active element. The active resistance implies the radiation power of each element provided an incident optical power into the photodiode when its active reactance is ignorable. Hence, the radiation power is quite uniform over the frequency from 3 to 9 GHz.



(a)



(b)

Figure 4.27 (a) HFSS model of $4 \times$ infinite TCA and (b) active impedances of four elements labeled in (a). The capacitance of photodiode and the impedance of TCA are accounted in the active impedances in (b).

4.4 Summary

Many popular electrical feeding techniques used to drive a TCA antenna are introduced in the survey, showing that the performance of TCA antennas is primarily restricted by various electrical feeding schemes. For example, the baluns used for the suppression of the common-mode resonances and impedance matching can degrade the operational bandwidth, increase the profile, and narrow the beam steering volume. To address these challenges as well as accommodate the optically enabled phased

array transmitter architecture presented in Chapter 1, an optical feeding scheme is proposed, for which incident light is coupled into the photodiodes that are directly integrated with each elements of a TCA antenna. The optical feeding scheme is superior to the electrical feeding particularly for dense antenna arrays such as a TCA antenna in that the operational bandwidth and low profile can be preserved. Moreover, the performance metrics of a photodiode-coupled TCA, including operational bandwidth, power efficiency, and radiation gain, are described. The main factors that restrict the operational bandwidth is identified and then multiple methods are studied to mitigate them. Lastly, as an example, a 12-GHz connected-dipole array is designed and simulated, which will be further developed in Chapter 6.

Chapter 5

ULTRA-WIDEBAND FEED NETWORK FOR OPTICALLY ADDRESSED PHASED ANTENNA ARRAY

5.1 Introduction to Optical Feed Network

Feed network as an essential part of a phased array is to impart signals to the frontend antennas and to control the phase of signals in each channel. Feed networks can be characterized by the metrics, such as operational/instantaneous bandwidth, insertion loss, and weight. Phase shifters are a component used in a phased array to adjust the phase of transmitting/receiving signals for radiation beam steering. In an electrically addressed phased array, the bandwidth and insertion loss of a feed network normally can degrade and restrict the performance of a phased array particularly at high gigahertz frequencies. In comparison, an optical feed network that is comprised of optical components can possess an operational bandwidth exceeding the entire RF spectrum. For example, 200 GHz represents a fractional bandwidth of only 0.1% for a 200-THz optical carrier. In addition, optical fibers have much lower insertion losses compared with RF coaxial cables or waveguides. Low-speed electro-optic (EO) phase modulators that act as phase shifters do not restrict the operational bandwidth of a phased array. Moreover, large-scaled phased arrays require true-time delay (TTD) lines to overcome emerging frequency squint effect. Optical TTD lines can achieve large delay times with more compact size, smaller dispersion, and lower insertion loss.

A novel optical feed network is proposed to accommodate the optically addressed phased array transmitter architecture (as described in Chapter 1) that

distributes two coherent optical signals with a frequency offset via optical fibers to generate a RF LO signal in the photodiodes. Before turning to the feed network, this chapter will start with a brief description of an ultra-wideband tunable photonic RF source.

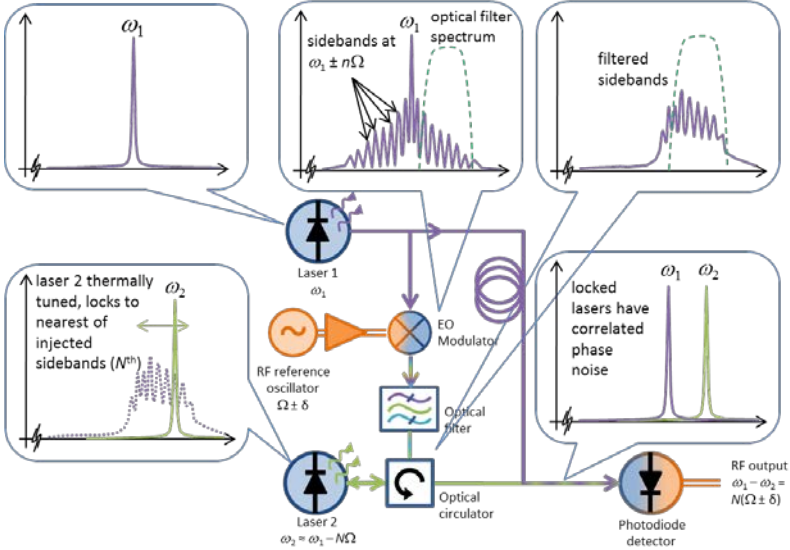


Figure 5.1 Schematic illustration of photonic tunable RF signal generator, reprinted by permission from Macmillan Publisher Ltd: Nature Photonics [3], © 2013.

5.2 UWB Tunable Photonic RF Source

A signal generator suitable for the proposed optically addressed phased array transmitter has been described in Ref. [3]. As shown in Figure 5.1, it uses a pair of semiconductor lasers, injection locked to render them coherent while offset from each other by a precisely controlled frequency that can be tuned over a range of > 100 GHz. One laser is injected with a comb of sidebands obtained by modulation of the other laser with a low-noise, low-frequency reference signal that has been distorted to yield a broad comb of harmonics; frequency tuning is enabled by a combination of coarse

thermal tuning to select which of the harmonics in the comb will be used for locking, and fine tuning by adjusting the reference oscillator. Spectrally pure output RF carriers are generated by mixing at a high-speed photodiode; advanced photodiodes have been demonstrated to have a bandwidth exceeding 100 GHz, and can produce significant output power at up to 500 GHz [3]. Data can be encoded to the optical output carrier by modulating either of the lasers before photomixing at photodiodes, since the data modulation carries through the down-conversion process.

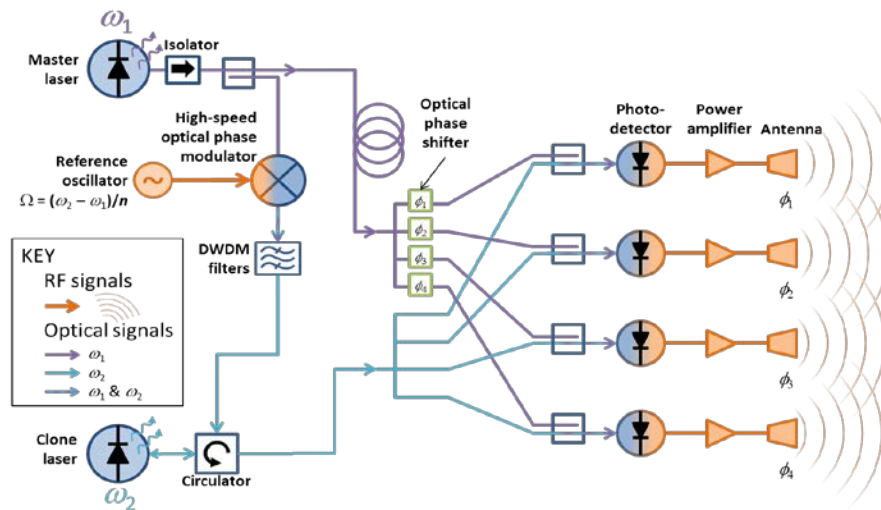


Figure 5.2 A simple scheme of optical feed network.

To apply it into a phased array, the generated coherent optical signals, ω_1 and ω_2 in the schematic, are required to distribute towards each antenna. To this end, a simple scheme is as shown in Figure 5.2, in which each tone is split into N channels with two 1-to- N beam splitters, one set of wavelength channels (tone of ω_1) is phase modulated with N electro-optic phase modulators, and then combined with the other set of optical signals (tone of ω_2) to form a N -channel optical feed network. The beam

splitting, phasing, and recombining can be achieved through typical optical components. However, this approach will impose some technical difficulties in the practical implementation. Due to thermal and mechanical stresses (e.g. acoustic wave) in each channel, relative phase between the two channels drifts over time with a rate as high as kilo-degrees per second, which results in the failure of performing beam steering. A novel optical feed network scheme is proposed to mitigate this time-varying phase fluctuation.

5.3 Novel Optical Phased Feed Network

5.3.1 Operating Principle

Figure 1.1 shows the proposed optical feed network scheme in which signal distribution is via interleaving optical fibers [68], [69]. In this scheme, two coherent optical sources, labeled as ω_1 and ω_2 , are combined with a polarization combiner into the fast and slow axes (i.e., orthogonal in polarization) of a polarization maintained (PM) fiber. The signal is amplified simultaneously with a polarization independent power amplifier, split into N channels with beam splitters, and conveyed to photodiodes for generating RF signals.

The phase drift of optical signals can be mitigated due to two following reasons. First, the phase fluctuation that occurs before the polarization combiner will be equally distributed to each channel. The produced RF signal in each channel after photomixing has an identical phase noise. Hence, the beam steering will be independent of this phase fluctuation. Second, due to the co-propagation of both optical signals in the same fiber after the polarization combiner, they will experience the same phase fluctuation caused by ambient acoustic vibration of fibers. As a result,

the phase variation of the two optical signals in the same fiber will be canceled at the photodiode.

In addition, the phase control in this scheme is realized by using EO phase modulators. Particularly, z -cut LiNbO₃ modulators are employed, in which the TM mode (electric field is aligned in the z direction) is phase modulated and the TE mode has a less modulation due to the odd distribution of electric field relative to the optical mode. After the phase modulation, both signals are projected to the fast and slow axes of the fiber by applying a 45° rotational key. The two sets of orthogonal signals are then filtered by a linear polarizer before mixing in a photodiode.

5.3.2 Analysis of the Optical Feed Network

To analyze the performance, one channel, i.e., i -th channel, is considered without loss of generality. This single channel is redrawn in Figure 5.3. Two coherent sources with the frequency of ω_1 and ω_2 are combined with a polarization combiner into the fast and slow axes of a PM fiber, respectively. As a result, the combined optical signals at the point P₁ can be expressed as:

$$\mathbf{E}_1 = yE_y e^{j[\omega_1 t + \varphi_1(t)]} + xE_x e^{j[\omega_2 t + \varphi_2(t)]} \quad (5.1)$$

in which E_x and E_y are the magnitudes of electric fields in x - and y -directions that correspond to the slow and fast axes of the PM fiber. $\varphi_1(t)$ and $\varphi_2(t)$ are random phase fluctuations that mechanical and thermal stresses induce. After a polarization combiner, the two orthogonal polarized signals are fed into an EO phase modulator for the phase tuning. Specifically, the slow and fast axes of the phase modulator are respectively aligned with the electric field of the TM and TE modes in the LiNbO₃ substrate [70], as shown in the inset of Figure 1.1. The voltage that is applied across

the coplanar electrodes, the electro-optic modulation occurs in both polarized optical modes, with EO coefficients of r_{33} and r_{14} , respectively. However, since $r_{33} = 3r_{14}$, a net phase difference can be imparted between the two optical modes. The signal at the point P_2 is given as:

$$\mathbf{E}_2 = \cancel{y}E_y e^{j\left(\omega_1 t + \phi_1(t) + \frac{\pi V_1}{V_\pi}\right)} + xE_x e^{j\left(\omega_2 t + \phi_2(t) + \frac{\pi V_2}{3V_\pi}\right)}, \quad (5.2)$$

in which V_i is the voltage applied to the modulator of the i -th channel, and V_π is the half-wave voltage that produces a phase shift of π .

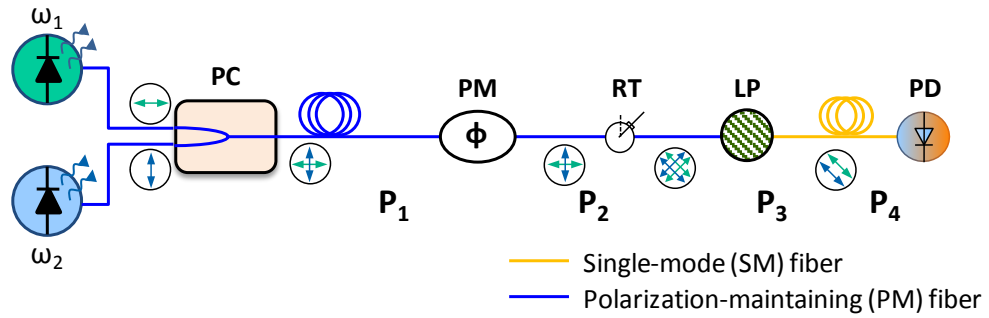


Figure 5.3 One channel of the proposed optical feed network scheme. PC: polarization combiner, PM: EO phase modulator, RT: 45° rotational key, LP: linear polarizer, PD: photodiode.

After the phase modulation, both signals are projected onto the fast and slow axes by applying a 45° rotational key. The rotational key can be realized by intentionally applying 45° offset in the alignment of optical axes between an input and an output PM fiber. Two sets of orthogonal signals are then filtered by a linear polarizer to ensure that they will interfere, before being delivered to photodiodes through a single-mode optical fiber. Taking into account 3-dB loss in a linear polarizer, the electric field at the point P_3 can be written as:

$$E_3 = \frac{\sqrt{2}}{2} \left[E_y e^{j\left(\omega_1 t + \varphi_1(t) + \frac{\pi V_i}{V_\pi}\right)} + E_x e^{j\left(\omega_2 t + \varphi_2(t) + \frac{\pi V_i}{3V_\pi}\right)} \right]. \quad (5.3)$$

Finally, this optical signal is fed to photodiodes where RF photocurrents are produced.

The RF photocurrent can be expressed as:

$$I_{rf} \propto \Re E_4 E_4^* = \frac{\Re E_x^2 E_y^2}{2} \cos \left[\omega_{rf} t + \varphi_1(t) - \varphi_2(t) + \frac{2\pi V_i}{3V_\pi} + \frac{\omega_1 - \omega_2}{c} n_0 L_i \right], \quad (5.4)$$

in which \Re is the responsivity of the photodiode, $\omega_{rf} = \omega_1 - \omega_2$ is the angular frequency of the generated RF photocurrent, c is light velocity, n_0 and L_i is the index and length of the single-mode (SM) fibers in i -th channel.

The length of the PM fibers and their relative index change will not alter the phase of RF signals. If the SM fiber with a length of L_i of each channel is accounted, an additional phase term of RF signals can be identified from in Eq. (5.4):

$$\varphi_{fb} = \frac{\omega_1 - \omega_2}{c} n_0 L_i. \quad (5.5)$$

Since the SM fibers are individually fed to each photodiode, they may experience different index change due to ambient temperature variation. The index fluctuation due to temperature variation can be empirically derived to be [71]:

$$\Delta n = \left(\frac{\partial n}{\partial T} \right) \delta T \approx 10^{-5} \delta T \quad (5.6)$$

For a given 10-meter optical fiber, the phase fluctuation, shown in the third term in Eq. (5.6), is on an order of 6 mrad if $\delta T = 0.1$ K. Such a small phase variation ensures reliable optical phasing in the phased array. To minimize the temperature difference

between fiber arrays during signal delivery, the optical fibers can be grouped together in system implementation.

In addition, a typical phase modulator has a V_π of 4.5 V. For a voltage swing of ± 10 V provided by the electronic controller, a maximum of 600° phase shift can be achieved to demonstrate beam-scanning capability. A progressive phase change, $\Delta\phi$, along adjacent antenna radiating elements, will lead to a RF beam with a steering angle determined by

$$\Delta\phi = k_{rf}d \sin \theta = \frac{2\pi\Delta V}{3V_\pi}, \quad (5.7)$$

in which d is the antenna element spacing, k_{rf} is the RF wave vector, and θ is the beam pointing direction.

5.4 Excess Noise

Several optical components in the proposed scheme are polarization sensitive devices, such as polarization combiners, EO phase modulators, and linear polarizer. Practically, the state of polarization (SoP) of input optical signals carried in PM fibers is not perfectly aligned with the axes of these optical devices. As an example, the orthogonally polarized two-tone optical signal incident into the phase modulator can have misalignment angles. In addition, the output signals of a polarization combiner are not exactly orthogonally polarized either. The similar issues can lead to excess noises, responsible for power variation in the time domain and spurious beams in the frequency domain. In order to analyze these noises, I first modify the model of the single channel shown in Figure 5.3 by introducing misalignment angles. As shown in Figure 5.4, the x - (TM-mode) and y -axis (TE-mode) are aligned respectively with the

electric field, E_1 and E_2 , of the incident light into the EO modulator. E_1 and E_2 may have the angles of ϕ_1 and ϕ_2 with the x - and y -axis. In addition, the polarization of the electric field in the EO phase modulator and the linear polarizer may have an angle of γ that is probably not exactly equal to 45° . The analysis performed below disregards SM fibers. The photocurrent at the point P_3 is expressed as:

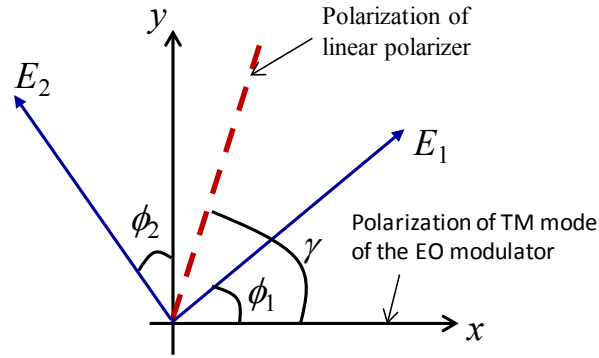


Figure 5.4 Schematic of polarization misalignment of the linear polarizer and the EO phase modulator. The electric field of TM mode in the cross plane are polarized along the x axis. The two tones of the incident optical signal are polarized along E_1 and E_2 , with the angles of ϕ_1 and ϕ_2 with respect to the x and y axis. The linear polarization is off the 45° and has the angle of γ with respect to the x axis.

$$\begin{aligned}
 i_{pd} \propto \Re E_{P_3} E_{P_3}^* = \Re & \left[E_1 \cos \phi_1 \cos \gamma e^{j(\omega_1 t + \theta + \phi_1)} - E_2 \sin \phi_2 \cos \gamma e^{j(\omega_2 t + \theta + \phi_2)} + \right. \\
 & \left. E_1 \sin \phi_1 \sin \gamma e^{j(\omega_1 t + \phi_1)} + E_2 \cos \phi_2 \sin \gamma e^{j(\omega_2 t + \phi_2)} \right] \\
 & \left[E_1 \cos \phi_1 \cos \gamma e^{-j(\omega_1 t + \theta + \phi_1)} - E_2 \sin \phi_2 \cos \gamma e^{-j(\omega_2 t + \theta + \phi_2)} + \right. \\
 & \left. E_1 \sin \phi_1 \sin \gamma e^{-j(\omega_1 t + \phi_1)} + E_2 \cos \phi_2 \sin \gamma e^{-j(\omega_2 t + \phi_2)} \right] \quad (5.8)
 \end{aligned}$$

Equivalently, Eq. (5.8) can be written into five terms with arrangement:

$$i_{PD} = I_{DC} + I_{AM} + i_{RFN} + i_{PMN} + i_{PMS} \quad (5.9)$$

in which:

$$I_{DC} = E_1^2 \cos^2 \phi_1 \cos^2 \gamma + E_2^2 \sin^2 \phi_2 \cos^2 \gamma + E_1^2 \sin^2 \phi_1 \sin^2 \gamma + E_2^2 \cos^2 \phi_2 \sin^2 \gamma \quad (5.10)$$

$$I_{AM} = \frac{1}{2} E_1^2 \sin 2\phi_1 \sin 2\gamma \cos \theta(t) - \frac{1}{2} E_2^2 \sin 2\phi_2 \sin 2\gamma \cos \theta(t) \quad (5.11)$$

$$i_{RFN} = 2E_1E_2 \sin \phi_1 \cos \phi_2 \sin^2 \gamma \cos(\omega_{rf}t + \phi_1 - \phi_2) - 2E_1E_2 \cos \phi_1 \sin \phi_2 \cos^2 \gamma \cos(\omega_{rf}t + \phi_1 - \phi_2) \quad (5.12)$$

$$i_{PMN} = -2E_1E_2 \sin \phi_1 \sin \phi_2 \cos 2\gamma \cos(\omega_{rf}t - \theta(t) - \phi_1 + \phi_2) \quad (5.13)$$

$$i_{PMS} = E_1E_2 \cos \phi_1 \cos \phi_2 \sin 2\gamma \cos(\omega_{rf}t + \theta(t) + \phi_1 - \phi_2) \quad (5.14)$$

in which ω_{rf} equals $\omega_1 - \omega_2$, $\theta(t)$ is the net phase change of the two polarized signals incurred by the EO phase modulators, i.e., $\theta(t) = 2\pi V(t)/3V_\pi$, in which $V(t)$ is the voltage applied to the modulators.

It is noted from Eq. (5.10) – Eq. (5.14) that i_{PMS} is the desired signal, I_{DC} is the DC current, I_{AM} is the current whose amplitude slowly drifts with the modulation phase of $\theta(t)$, i_{RFN} is the noise with the frequency of ω_{rf} , and i_{PMN} is the noise with the frequency of ω_{rf} as well as the phase opposite to i_{PMS} . I_{DC} and I_{AM} can be easily removed using high-pass filters or antennas; however, i_{PMN} and i_{RFN} cannot be filtered out and thus become the excess noise in the system in addition to intrinsic thermal and shot noises. If RF signals corrupted by these excess noises are transmitted, a main beam as well as two spurious beams forms. As shown in Figure 5.5, i_{RFN} produces a spurious beam pointing at the broadside of an array that does not vary with the imposed phase. Meanwhile, another spurious beam due to i_{PMN} is at the opposite direction of the steered main beam. From Eq. (5.12) and Eq. (5.13), i_{RFN} is noticed to be much stronger than i_{PMN} for small values of ϕ_1 and ϕ_2 . Therefore, the system

sensitivity is determined by the beam power generated by i_{RFN} which thereby need to be mitigated.

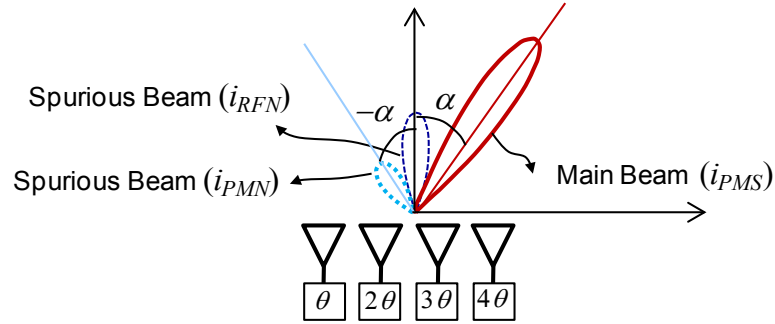


Figure 5.5 The main and spurious radiation beams formed by the signal and excess noises. The two spurious beams are generated by the noise terms of i_{RFN} and i_{PMN} , respectively.

There are two ways to observe the strength of i_{RFN} . First, when an identical phase of $\theta(t)$ is applied to all of the array elements, an amplitude modulated (AM) signal in the far-field, as a result of the interference of i_{PMS} and i_{RFN} , can be observed. Second, the strength of i_{RFN} is correlated with that of i_{AM} as observed from Eq. (5.11) and Eq. (5.12). The swing range of I_{AM} is proportional to that of i_{RFN} , and i_{RFN} reduces to zero as i_{AM} approaches zero. Figure 5.6 shows the simulated results of the generated RF signal from a single channel when $\phi_1 = 5^\circ$, $\phi_2 = 10^\circ$, $\gamma = 45^\circ$, $E_x = E_y = 1$ V/m, and no conversion loss is assumed. Notably, the RF signal has strong amplitude modulation. In fact, the main factor which leads to the generation of i_{RFN} comes from undesired polarization or mode misalignment between adjacent optical components.

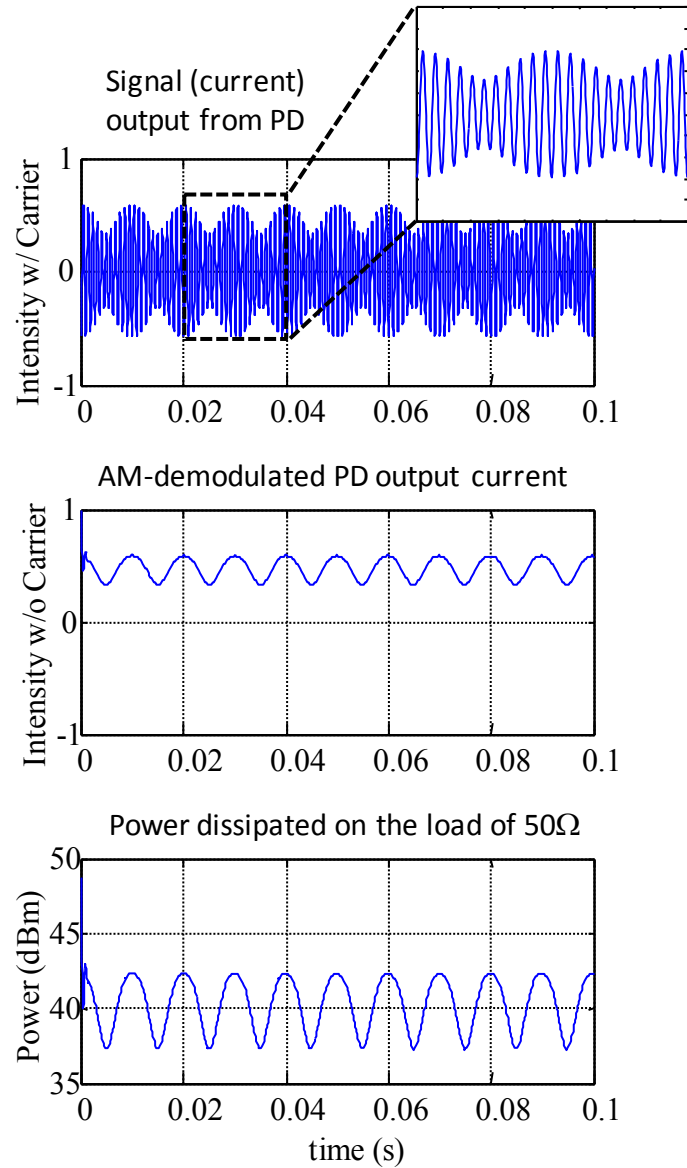


Figure 5.6 The simulation results of output signals with excess noises. (Top: an optical carrier corrupted by the noises incident into a photodiode. Middle: the intensity or envelop of the optical carrier. Bottom: the photodiode output.)

Figure 5.7 shows how the RF power variation is related to the SoP. In the simulation, ϕ_1 is fixed to be 5° , and ϕ_2 varies from -20° to 20° , and $\gamma = 45^\circ$. The

analytical results are obtained from using from Eq. (5.9) to Eq. (5.14). Transmission matrix method (TMM) is also used for comparison and the results obtained from both methods are in good agreement. It should be noted that the minimum value occurs at $\phi_1 = \phi_2$, i.e., when the polarizations of two optical signals are orthogonal.

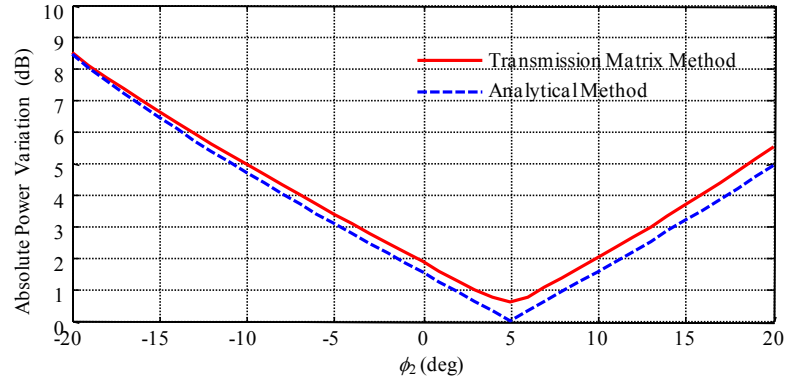


Figure 5.7 Excess noises versus the polarization angle ϕ_2 of an incident optical signal (assumes $\phi_1 = 5^\circ$ and $\gamma = 45^\circ$). The results are obtained from a transmission matrix and an analytical method for comparison.

More importantly, it is found that even five degree misalignment between components can lead to a 1.8 dB power variation of the RF signal. For example, a commercial off-the-shelf polarization combiner with typical extinction ratio of 20 dB can produce two combined optical signals with five degree deviation from the orthogonal polarization [72]. Therefore, it is necessary to control the SoP of input signals in each channel. To this end, commercial polarization controllers (PCs) added before the phase modulator as shown in Figure 5.8 to control SOP [69]. The SoP of an input signal can be optimized by tuning the PC to decrease the level of AM of either the far-field RF power or i_{AM} detected from the photodiode.

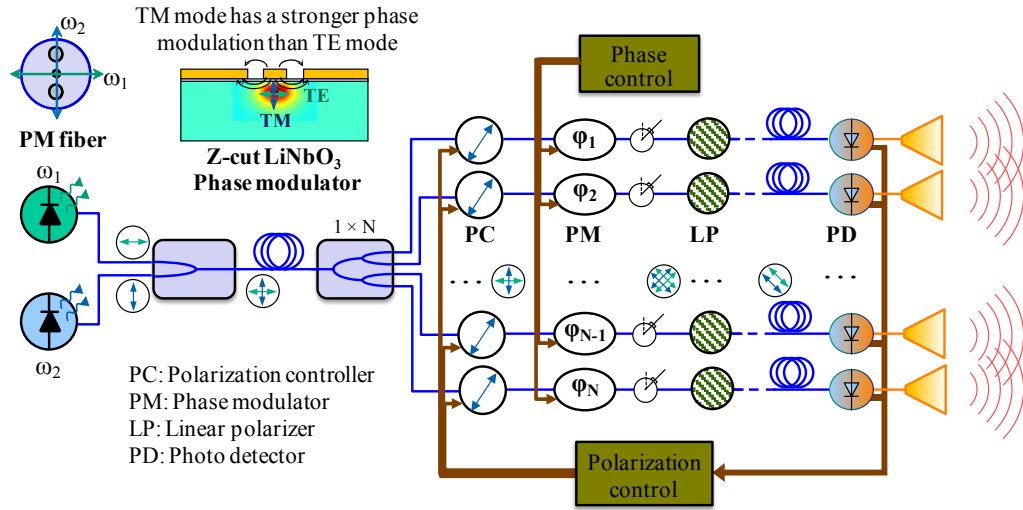


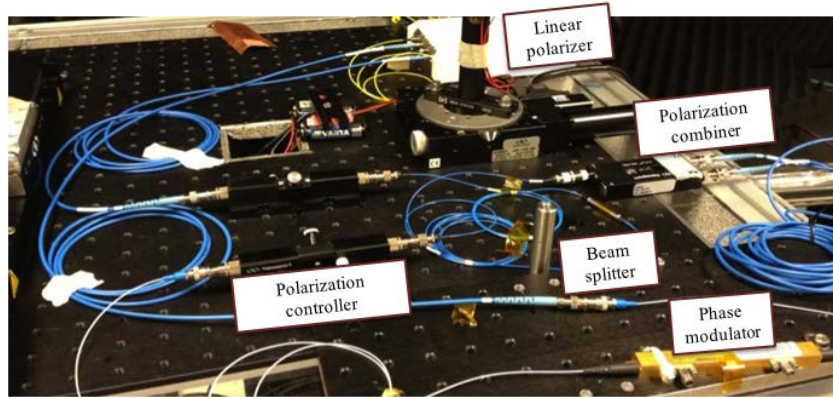
Figure 5.8 Schematic of an improved optical feed network with polarization controls to suppress excess noises.

5.5 Experimental Demonstrations

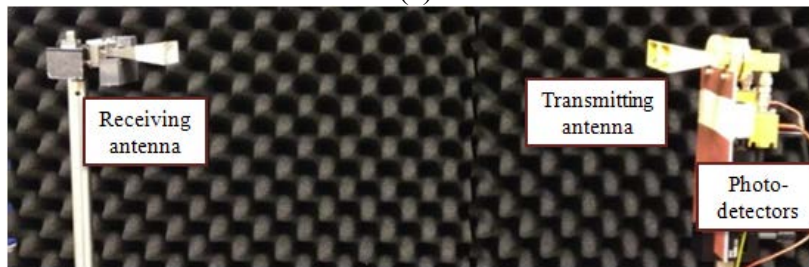
5.5.1 Two-Channel Network with Manual SoP Controls

Based on the proposed scheme, a 1×2 optical feed network is developed as shown in Figure 5.9. Two manually adjustable polarization controllers are used to tune the SoP of the optical signals incident into the LiNbO₃ phase modulators. The two tones have the frequency offset of 35 GHz, and mix at the photodiodes with 3-dB bandwidth of 40 GHz. The produced RF signals are transmitted with two Ka-band standard horn antennas. The array is mounted on a rotation stage for far-field radiation pattern measurement by using another Ka-band rectangular horn as a receiver. The RF power is measured by an Agilent PNA Network Analyzer (E8361C). To characterize the noise of the system, an identical saw-tooth voltage with a period of 0.75 seconds and a magnitude of 15 volts, i.e. $2V_{\pi}$, is used to independently drive the phase

modulator of each channel. A repeatable and steady RF response can be observed in Figure 5.10.



(a)



(b)

Figure 5.9 The measurement setup consisting of (a) 1×2 optical fiber feed network and (b) a transmitting horn antenna and two receiving horn antennas.

As seen from the figure, without the polarization controller, the RF power swing range is as large as 3.5 dB. As discussed, this is due to the interference between the main beam and the spurious beam generated by i_{RFN} . It is worth pointing out that the spurious beam due to i_{RFN} can significantly decrease the sensitivity of the receiver. For example, when the first null of an array factor is steered to the broadside, the radiating power at the broadside is not close to the noise floor, e.g. thermal noise, but the power of the spurious beam instead. The use of the polarization controller, as

shown in Figure 5.10, is able to significantly reduce the power swing from 3.5 dB to 0.6 dB. In other words, the percentage of the power of the spurious beams with respect to that of the main beam decreases from 17% to 3%. Therefore, applying the polarization controller can dramatically reduce the excess noise of the system and therefore suppress the spurious beam.

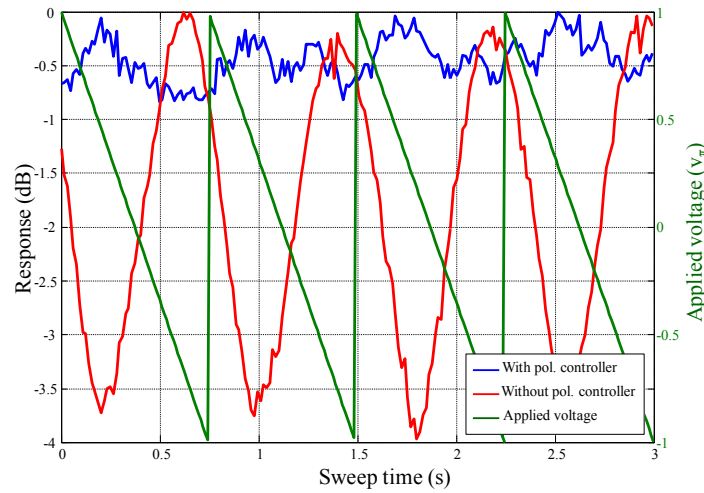


Figure 5.10 The experimental far-field response of the single channel under a periodic saw-tooth voltage signal applied to the phase modulator.

To demonstrate the capability of phase scanning, balanced RF power is transmitted from the two antennas, one of which is with a phase tuned by the phase modulator, while the other one has a constant phase. Both of the channels have the polarization controller to suppress the excess noise. When the phase is changed from 0° to 177.5° , the main beam of the array sweeps from 0° to 4° until the grating lobe appears. Notably, when the signals of the two channels are out of phase ($\sim 180^\circ$), their broadside is a null of the radiation pattern of the array. Also, the received power is only from the spurious beam. As seen from Figure 5.11, the power is 25 dB lower than

that of the main beam, which is in good agreement with the previous estimation. This demonstrates that the excess noise has been dramatically suppressed.

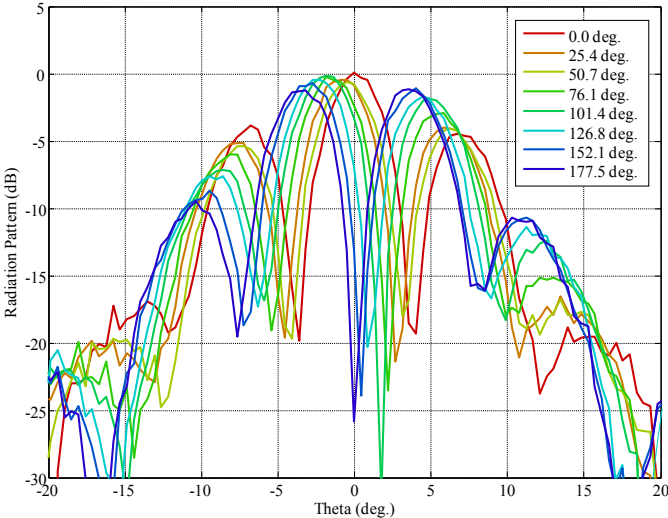


Figure 5.11 The measured radiation patterns of the 1×2 phased array under electric beam scanning.

5.5.2 Four-Channel Network with Adaptive SoP Controls

In the previous sections, manually controlled PCs are used to demonstrate the ability to suppress the excess noises. Practically, the feed networks are required to optimize the SoP in an adaptive way. To this end, thermal PCs are used, which can control the SoP based on the DC photocurrent feedback from the photodiodes. Figure 5.12 (a) shows the developed four-channel optical feed network. As seen from the figure, the four PCs and PMs are mounted on a printed circuit board (PCB) for electronic controls and communications with LabView programs. An optimum SoP occurs when the feedback DC photocurrents that are feedback from the photodiodes and acquired by a NI DAQ have minimum amplitude variations. This is because the

DC current I_{AM} in Eq. (5.11) is correlated with amplitude of excess noise i_{PMN} in Eq. (5.13). The produced RF signal is transmitted by two ultra-wideband Vivaldi antennas as shown in Figure 5.12 (b). The antennas are mounted on a rotation stage for far-field radiation pattern measurements.

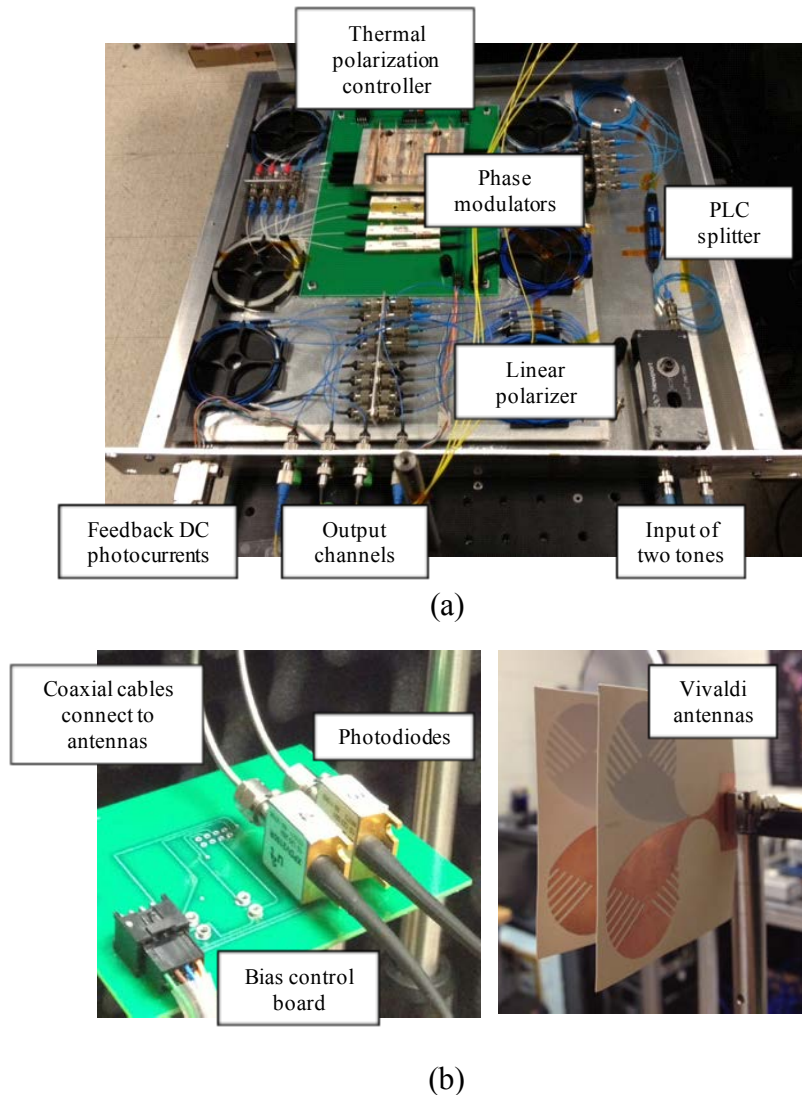


Figure 5.12 (a) The four-channel optical feed network, and (b) a 1×2 Vivaldi antenna array and far-field measurement setup

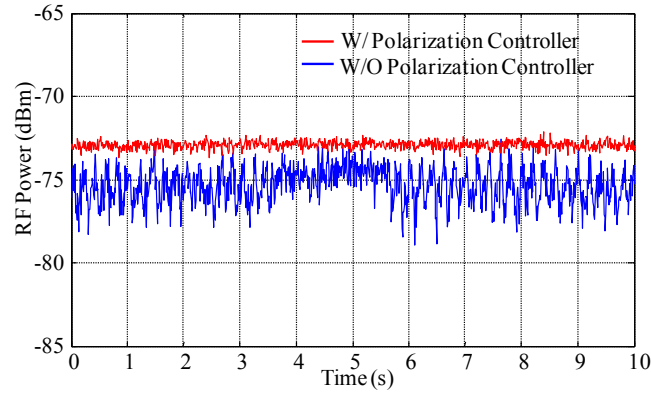


Figure 5.13 The experimental far-field response of a single channel when a periodic saw-tooth voltage signal is applied to the EO phase modulators.

To characterize the noise of the system, an identical saw-tooth voltage with a frequency of 5 Hz and a magnitude of 15 volts, i.e. $2V_{\pi}$, is used to independently drive the phase modulator of each channel. The DC current generated from each photodiode is extracted to correlate with the excess noise of RF signals. Figure 5.13 shows the measured far-field RF signal of one channel without the PC and with the PC at an optimum state.

In addition, Figure 5.14 shows measured DC current of the same channel, respectively with and without the PC. For comparison, the excess noise of the generated RF signal is found to become lowest when the DC current also has a minimum variation. Therefore, this observation confirms the analysis in Section 5.5.1. Based on this observation, the DC photocurrent can be used as a feedback signal to form a feedback loop, allowing an optimum SoP that results in minimum excess noises to be adaptively obtained by monitoring the feedback. As shown in Figure 5.13, without the PC, the RF power swing range is as large as 3 dB. Again, this is due to the interference between the main beam and the spurious beam generated by i_{RFN} .

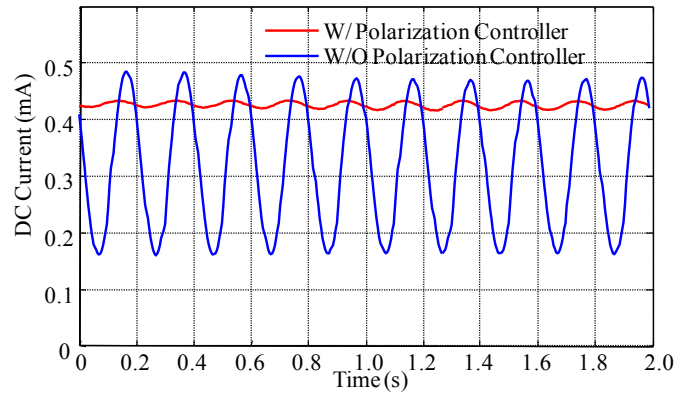


Figure 5.14 The output DC current of the photodiode when a periodic saw-tooth voltage signal is the EO phase modulator with and without polarization control.

To demonstrate the capability of phase scanning, balanced RF powers are transmitted by the two Vivaldi antennas. One of them has the phase to be tuned by the phase modulator while another has a constant phase. Two channels utilize the PC to minimize the excess phase noise by optimizing the polarization. When a voltage varying from 0 to V_π is applied to the EO phase modulator, the main beam of the phased array can sweep from 0° to 10° . The power of the main beam will significantly decrease when the angle is steered more than 10° . The narrow steering angle is due to the high antenna gains. When the signals fed into the two antennas are exactly out of phase, the broadside has a minimum radiation power, and the received power is expected to be from the spurious beam or measurement thermal noise floor. As seen from Figure 5.15, the power is 20 dB lower than that of the main beam and the result is in a good agreement with the estimation given in the last section. In addition, since the optical feed network is completely decoupled with RF devices, this phased array have an operational bandwidth as long as the antenna and RF source can provide.

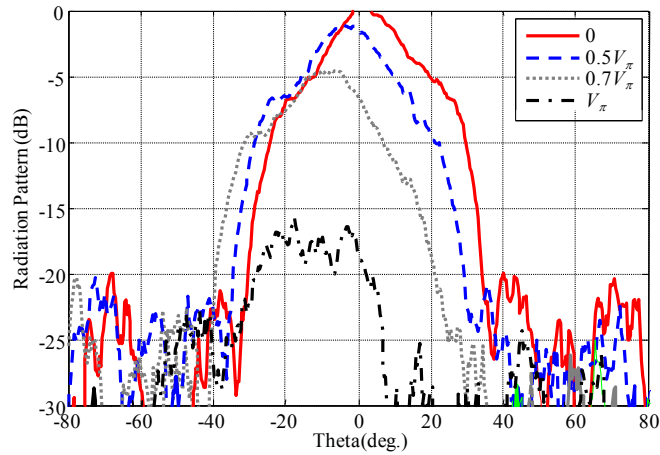


Figure 5.15 The measured radiation patterns at 20 GHz with different bias voltages on the EO phase modulator.

5.6 Summary

A novel optical feed network is demonstrated, which distributes a two-tone coherent optical signal for mixing at the frontends of an active RF aperture with low phase noise via orthogonal polarizations of an optical fiber. Beam steering is also demonstrated using electro-optic (EO) phase modulators. In addition, the excess phase noise introduced by the misalignment between the polarization states of the optical signals and EO phase modulator is overcome using polarization controllers and feedback DC photocurrent. The beam steering is demonstrated using narrowband standard horn and ultra-wideband Vivaldi antennas.

Technical and practical advantages include low transmission loss, minimum phase noise, light weight and flexible distribution to a conformal two-dimensional array, ultra-wideband operation, and easy implementation and large scalability.

Chapter 6

SYSTEM DEVELOPMENT AND DEMONSTRATION

6.1 Optically Addressed Phased Array Transmitter Architecture

The optically addressed phased array transmitter architecture, briefly described in Section 1.1, will be detailed in this chapter. As shown in Figure 6.1, the proposed architecture is primarily comprised of the optical RF synthesizer, optical phased feed network, and active RF aperture in addition to electronic control. These key subsystems have been demonstrated individually and can be brought together to develop a system prototype. The optical RF source has an ultra-wideband tuning range from S band (2 - 4 GHz) to W band (75 - 110 GHz) [3]. The highest frequency of the generated RF signal is restricted by the photodiode speed. The signal distribution is via optical fibers, offering abundant bandwidth that can cover the entire RF spectrum. In the proposed architecture, the system bandwidth is primarily limited by the RF aperture.

Each frontend of a RF aperture is ideally comprised of a high-power high-speed photodiode and an ultra-wideband radiator. This frontend can be realized by assembling a packaged photodiode with an antenna via RF coaxial cables. In this way, the antenna and photodiode can be independently designed and characterized. The operational bandwidth of this frontend is primarily determined by antennas, when the photodiode has a sufficiently high speed. The Vivaldi antennas (see Chapter 2) with over 25:1 impedance bandwidth is applicable to this frontend for an ultra-wide bandwidth. However, the Vivaldi antennas that have high gains particularly at high

frequencies can only achieve narrow scanning volumes. In addition, the ESA antenna (see Chapter 3) with a low gain can achieve a large scanning volume, but only possesses a narrow operational bandwidth.

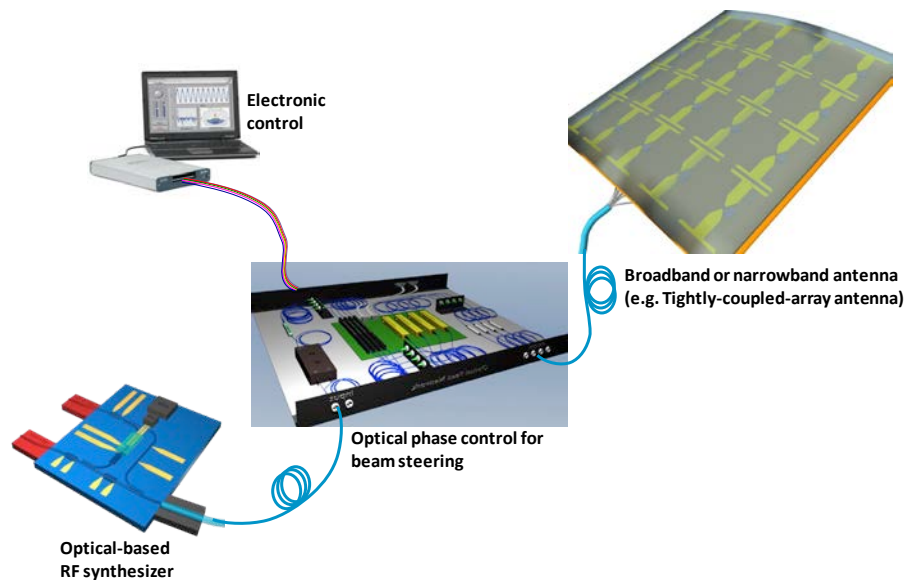


Figure 6.1 Functional modules of an optically addressed phased array: RF synthesizer, optical phase control, electronic control, and active frontends.

TCA antennas (see Chapter 4) are an ideal candidate, which provide ultra-wide bandwidth and large scanning volume in addition to low profile and cross-polarization. These advantages inherent in TCA antennas, however, are compromised by many practical and technical challenges introduced by various electrical feeding schemes. The use of assembled photodiodes and TCA antennas suffers from the issues similar to the electrical feeding schemes. To address these problems, an optical feeding scheme is proposed in Chapter 4. In this scheme, light is coupled into the photodiodes that are directly integrated with a TCA antenna. Hence, the problems resulted from RF transmission lines can be eliminated. Two challenges still remain to

implement the optical feeding scheme. The photodiodes and their integration can affect the performance of a TCA antenna, which needs to be considered when a TCA antenna is designed. In addition, these integrated frontends are more difficult to characterize than the assembled, since the performance of the antenna and photodiode is coupled. This chapter will discuss the fabrication and integration of photodiode-coupled TCA antennas.

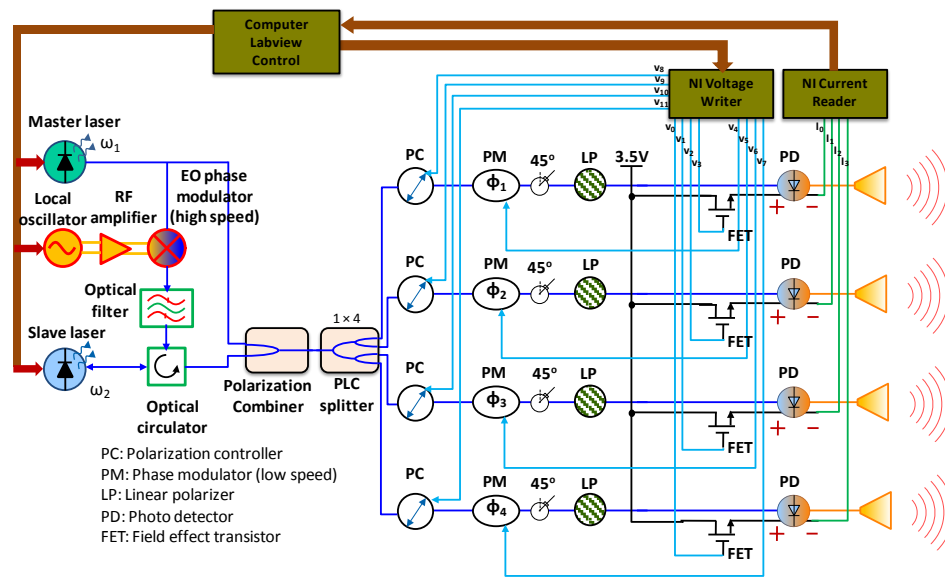


Figure 6.2 Schematic of a four-channel optically addressed phased array transmitter.

In addition, a system prototype is developed to demonstrate the proposed architecture. In the demonstration, two kinds of the frontends will be employed, an assembled photodiode-fed patch antenna array and a photodiode-coupled TCA antenna integrated with optical fibers. The prototype schematic is as shown in Figure 6.2, and its operating principle will be discussed in the following sections.

6.2 Ultra-wideband Tunable RF Synthesizer

A high quality and widely tunable RF source, as shown in Figure 6.2, which has a similar operating principle as described in Chapter 5, is demonstrated. Figure 6.3 shows the developed compact optical RF synthesizer built with two distributed feedback (DFB) lasers, a high-speed modulator, and optical fibers, assembled into a rack mount chassis. The two DFB lasers have operational wavelength around 1548.5 nm, and maximum output power of 10 dBm. Agilent PSG source is employed as a tunable local oscillator.

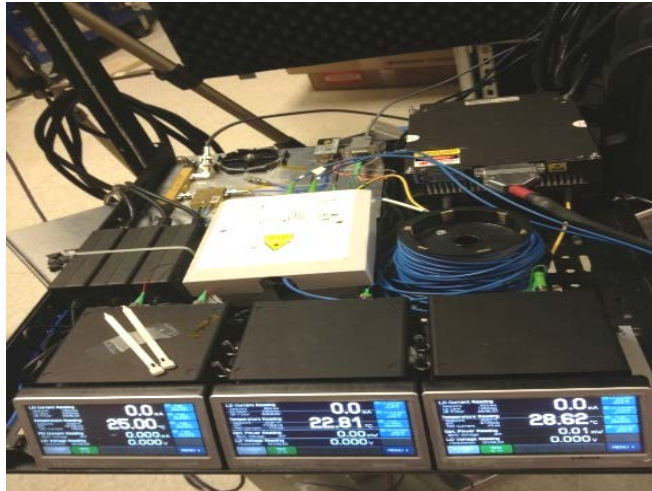


Figure 6.3 The developed optically tunable RF synthesizer. The devices shown in the figure are two optical lasers, an optical semiconductor amplifier, an EDFA, optical filter, EO phase modulator, and RF local oscillator.

In this implementation, a local oscillator frequency range from 4 to 5 GHz is chosen. Thus, to attain a scaled RF frequency range of 4 – 50 GHz modulation harmonics from 1 – 13 are used. To keep up with the frequency of the changed injected optical signal, the injection-locking laser may also require a slight tuning to ensure phase locking. To this end, an integrated thermo-electric cooler (TEC) is

employed to thermally tune the free-running frequency of the injected laser. The compact laser diode driver (Thorlabs) provide an integrated closed-loop temperature controller, enabling precise thermal control and thus wavelength tuning. In conjunction with the remote controlled local oscillator (with Labview program on the computer), we are able to continuously tune the RF frequency of the synthesizer.

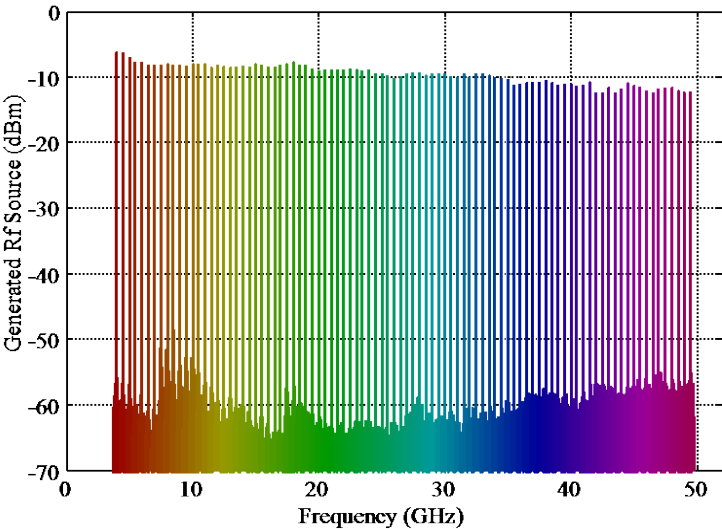


Figure 6.4 Measured power of the RF source tunable from 4 – 50 GHz with a step frequency of 0.5 GHz.

Figure 6.4 shows the measured RF power spectra at selected RF frequencies with an increment of 0.5 GHz over a frequency span of 4 – 50 GHz, obtained with an electrical spectrum analyzer (ESA), Agilent N9030A. As seen from the figure, the RF synthesizer can be continuously tuned from 4 to 50 GHz. It has been shown to operate at even higher RF. Over the band, the generated RF power maintains good response with a minimal roll-off at higher frequencies. The reduced power at high frequency is attributed from RF loss and reduced frequency response of the high-speed photodiode.

To examine the purity of the generated source, both linewidth and phase noise are measured at each frequency. The spectral linewidth is measured to be ≤ 1 Hz, which is the resolution limit of the ESA. Figure 6.5 shows the measured phase noise spectrum of a generated RF signal at 36 GHz as a function of the offset frequency from the generated RF. As one can see from the figure, the phase noise follows that of the local oscillator (scaled to the output frequency with additive noise of $20\log_{10}(m)$). The additive phase noise induced in the fiber due to acoustics vibration can be further suppressed by using chip-level integration approach.

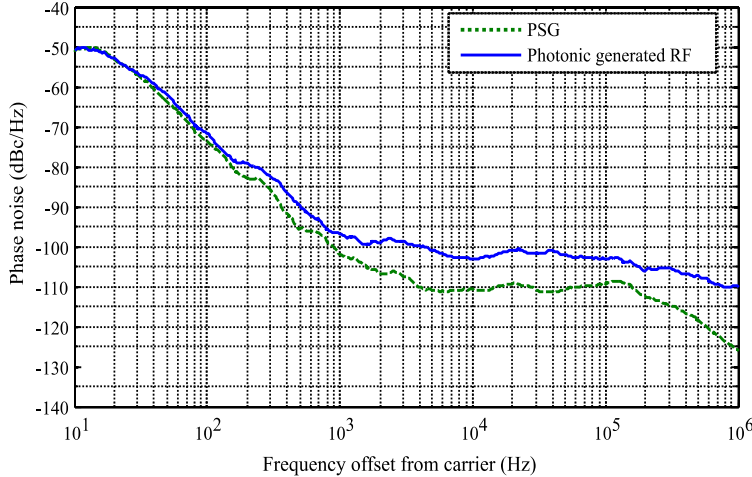


Figure 6.5 Measured phase noise spectrum of the generated RF source at 35 GHz as function of offset frequency.

6.3 Optical Feed Network and Phase Control

An optical feed network as shown Figure 6.6 is developed. Since the operating principle has been detailed in Chapter 5, this section is focused on the remote electronic controls for the beam steering. As shown in Figure 6.2, the PC and PM are respectively controlled by the voltage signals from the ports of V4 – V7 and V8 – V11

in the National Instrument Digital Acquisition (NI DAQ). Particularly, the voltage signals from the ports of V8 – V11 are to adjust the polarization controllers for minimizing the excess noises. Meanwhile, to estimate the excess noises, the DC photocurrent of each channel is acquired by the ports I0 – I3 of another NI DAQ. Each channel has a field-effect-transistor (FET) switch that can be turned on by a 3.5-V voltage from the ports of V0 – V3. An automatic calibration routine is developed to constantly perform this calibration in which the pair-wire phase measurement is conducted by controlling the FET switches to calibrate the phase front at the antenna elements.

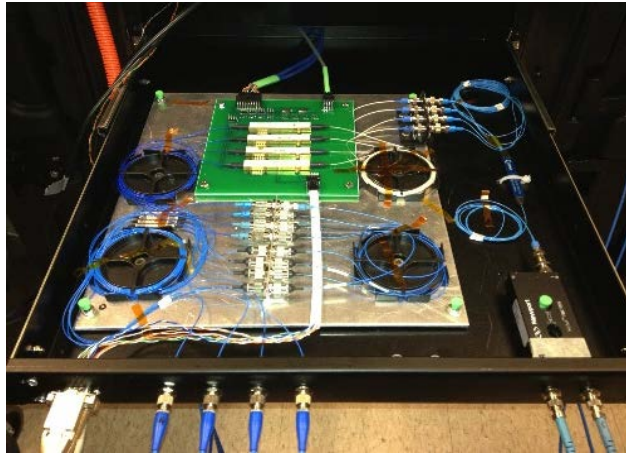


Figure 6.6 The developed optical phased feed network and phase control module.

6.4 High-Sensitivity Photonic RF Receiver

In order to establish a complete photonic based RF link, a photonic receiver is required. Over the years, significant efforts have been focused in the development of radio-over-fiber links in order to efficiently transport high frequency RF signals. The intensity-modulation/direct-detection (IMDD) has been well studied [73]-[75].

However, it suffers from limited spur free dynamic range (SFDR) due to its inherent nonlinear transfer function characteristics. As another alternative, recently, a phase modulated approach has been proposed to improve system linearity [76], [77]. To this end, based on an optical up-conversion approach [78], [79], I developed a photonic receiver to demonstrate all-optical transmitting and receiving. This approach is to leverage high-speed Lithium Niobate (LiNbO_3) EO phase modulator for more efficient RF detection. The electro-optic modulators serve to upconvert received RF fields onto an optical carrier, such fields can be readily captured, routed, and processed using optical techniques, thereby providing significant advantages over traditional heterodyne detection system, particularly at mm-wave frequencies.

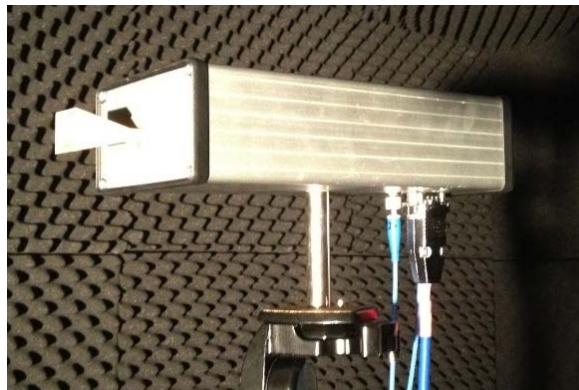


Figure 6.7 Developed photonic receiver.

The developed photonic receiver is shown in Figure 6.7 [80] and its schematic is illustrated in Figure 6.8. Incident RF radiation from the transmitting array antenna is collected by a Ka-band horn antenna, amplified, and up-converted to a telecom frequency via an EO phase modulator, leading to an upper and a lower optical sideband around the optical carrier frequency. The amount of energy in the sidebands, I_{sb} , can be quantified as:

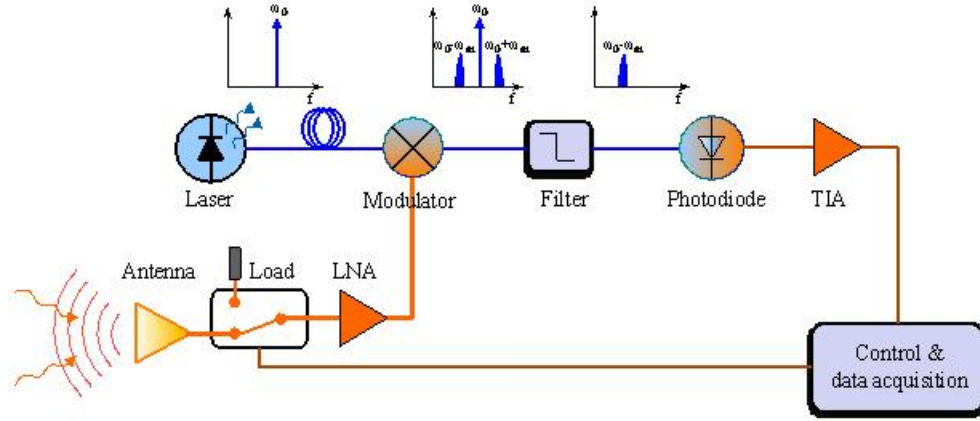


Figure 6.8 Photonic receiver based on optical up-conversion technique.

$$I_{sb} = \eta_{\text{mod}} g_{LNA} P_{rf} I_{opt} \quad (6.1)$$

where I_{opt} is the optical power into the modulator, P_{rf} is the RF power received at the antenna, g_{LNA} is the gain of low-noise amplifier, η_{mod} is the modulation efficiency of the modulator that may be predicted as a function of the electrical properties of the modulator, such as dielectric losses and conduction losses of the electrodes, index mismatch between the optical and millimeter-wave traveling modes, the DC half-wave voltage of the device, and the RF impedance of the electrodes. The conversion efficiency can be also derived as:

$$\eta_{\text{mod}} = \frac{\pi^2 Z}{2V_{\pi}^2} \quad (6.2)$$

in which Z is the impedance of the modulator and V_{π} is the half-wave modulation voltage. The modulated signals can be further fed into an optical filter to suppress the carrier signal while passing one of the sidebands. A square-law detector (photodiode) is used to convert this sideband into a voltage that can be easily measured. The weak

current produced at the photodiode can be further amplified using a transimpedance amplifier (TIA). As a result, the voltage generated at the output of TIA can be derived as:

$$I_{sb} = g_{TIA} \mathfrak{R}_{reciv} \eta_{mod} g_{LNA} P_{rf} I_{opt} \quad (6.3)$$

The use of a low-noise amplifier (LNA), as well as incomplete suppression of the optical carrier, may lead to an increased noise floor. To measure the intensity of the radiated RF field in the far field, a Dicke switching is used. The signal is chopped by a set of SPDT PIN switch before the signal hits the modulator at a known frequency of 1 KHz. Dicke switching results in a signal after modulation that is periodic with its amplitude related to the difference between a known load temperature and the temperature of the scene. As an improvement to digital lock-in, the system utilizes a novel least squares estimator (LSE) method to derive the amplitude, phase and offset of the signal at the chop frequency [81]. The LSE method eliminates the need for a costly and bulky lock-in amplifier and can be done in real time using software instead of hardware.

The developed sensor technology offers extreme sensitivity, i.e., noise-equivalent temperature difference (NETD) < 1 K. In the system implementation, a LNA with a gain of 35 dB over the frequency range from 33.5 to 38 GHz is used. An EM4 DFB laser operated at a wavelength of 1546.8 nm is used. The laser output power is 9 dBm, and fed into a phase modulator. The modulation efficiency at the frequency of 35 GHz is measured to be 1.2 W⁻¹. Three stages of DWDM optical filters are used to suppress the optical carrier with a suppression ratio of 45 dB. The photodiode has an operational bandwidth of 1 GHz, and the TIA has a gain of 1 GV/A

and bandwidth of 4 kHz. The produced voltage is measured by using NI DAQ system. Due to the limited bandwidth of the TIA, the developed photonic receiver functions as a photonically based power detector.

6.5 Experimental Demonstration: 4 × 4 Ka-Band Patch Antenna Array

6.5.1 Patch Antenna Design

The configuration and dimensions of an aperture-coupled patch antenna are shown in Figure 6.9 (a), wherein the feeding microstrip is coupled through a slot etched on the ground plane to excite the patch for radiation [82], [83]. The microstrip lines are designed on a flexible liquid crystal polymer (LCP) substrate with a thickness of 0.101 mm and a dielectric constant of 2.9. The LCP substrate is a good choice for the antenna and RF circuit designs owing to its low dielectric constant and low dielectric loss at high RF frequencies. The width of the microstrip line is 0.35 mm to yield an impedance of 50 Ohms. The antenna patch, with its size of 2.1 mm by 2.3 mm, is fabricated on RT/duroid 5880 substrate with a thickness of 0.787 mm and a dielectric constant of 2.2. The choice of such a thick patch substrate is to reduce the capacitance between the patch and ground plane, thereby increasing antenna impedance bandwidth and improving radiation efficiency. In the array configuration, to minimize the grating lobes without significantly introducing mutual coupling, a spacing of $d = 4$ mm between array elements is chosen.

A 3D finite element method (FEM) electromagnetic solver, ANSYS HFSS, is used to design and optimize the patch antenna. The proposed antenna has an impedance bandwidth of 23%, ranging from 31 to 39 GHz, as shown in Figure 6.9 (c). The 3-dB beam width of a single patch antenna in both the E- and H-planes are as

wide as $\pm 50^\circ$, which allows us to realize wide angle steering for the phased array application. To improve the antenna array gain, four patch elements designed along the vertical direction (H-plane) are used to form a 1×4 subarray. Two stages of power splitting are used to produce equal amplitude and phase at each antenna element. The beam width in the H-plane is reduced to $\pm 15^\circ$. The simulated and measured S parameters are shown in Figure 6.9 (b), in which the discrepancies in the S-parameters are caused by fabrication tolerance and loss in the RF connector.

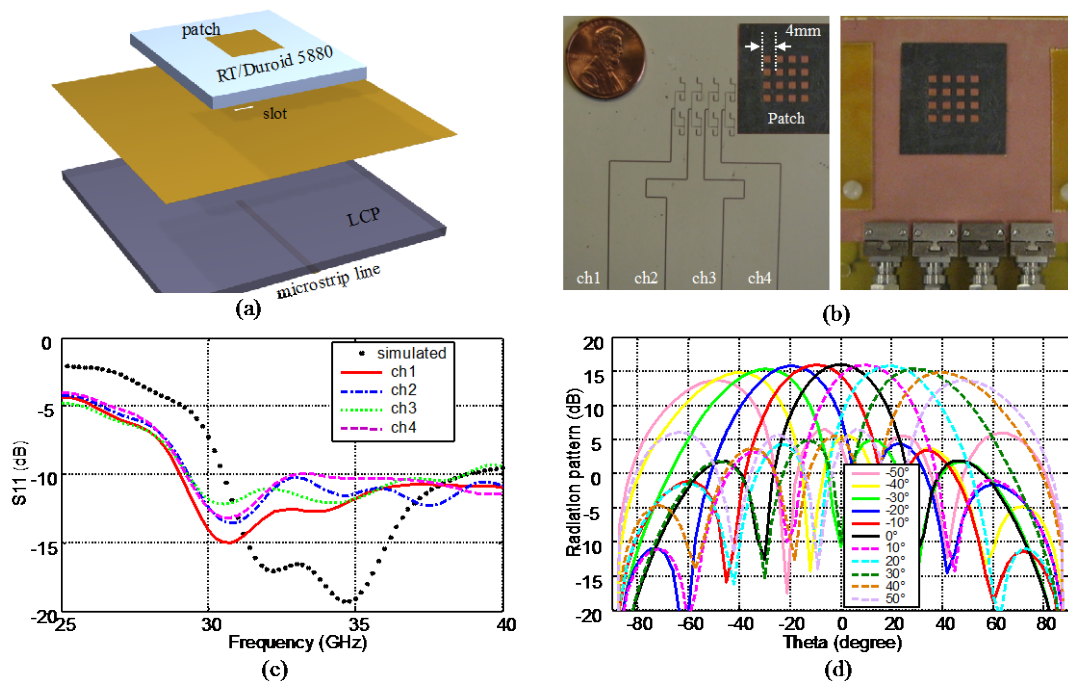


Figure 6.9 (a) The configuration of a microstrip-fed slot-coupled patch antenna. (b) Fabricated 4×4 patch array antenna, in which every four elements in the vertical direction are fed in-phase with power splitter to form a subarray, and four of such subarrays are fed by the optically addressed feed network to attain a phased array. (c) Simulated and measured S parameters of four subarrays. (d) Simulated radiation patterns at 36 GHz over the active beam scanning angles of $\pm 50^\circ$ in the E-plane.

Finally, four 1×4 subarrays are used to make up a 4×4 array, as shown in Figure 6.9 (b). The winding microstrip lines have equal electric lengths to ensure the same phase in each channel. They are designed to match the dimensions of the wideband connectors, which are used to connect the antenna array and optical phase feed network. The 4×4 array attains a gain of 15.6 dB and a beamwidth of $\pm 15^\circ$ in both E- and H-planes. Figure 6.9 (d) shows the simulated radiation patterns of 4×4 array by electrically scanning along the horizontal direction (E-plane).

6.5.2 Experimental Results

To phase the array, an embedded control system is used to actively adjust the DC bias of each phase modulator. Progressive phase distribution can be determined based on the desired steering angle, the operational RF frequency, and antenna element spacing, given by:

$$\Delta\varphi = k_{rf}d \sin \theta = \frac{2\pi\Delta V}{3V_\pi} \quad (6.4)$$

in which d is the antenna element spacing, k_{rf} is the RF wave vector, and θ is the beam pointing direction.

An angular range from -90° to 90° is set to demonstrate the beam steering. The far-field measurement system is illustrated in Figure 6.10 (a), in which the transmitting phased array antenna and photonic RF receiver are arranged to face each other. The receiving antenna is set to be 2 meters away from the transmitting phased array antenna. A progressive phase distribution is applied at each channel in the optical phase feed network to form a linear phase front at the patch array, thereby producing an electrical beam steering without any mechanical movement involved.

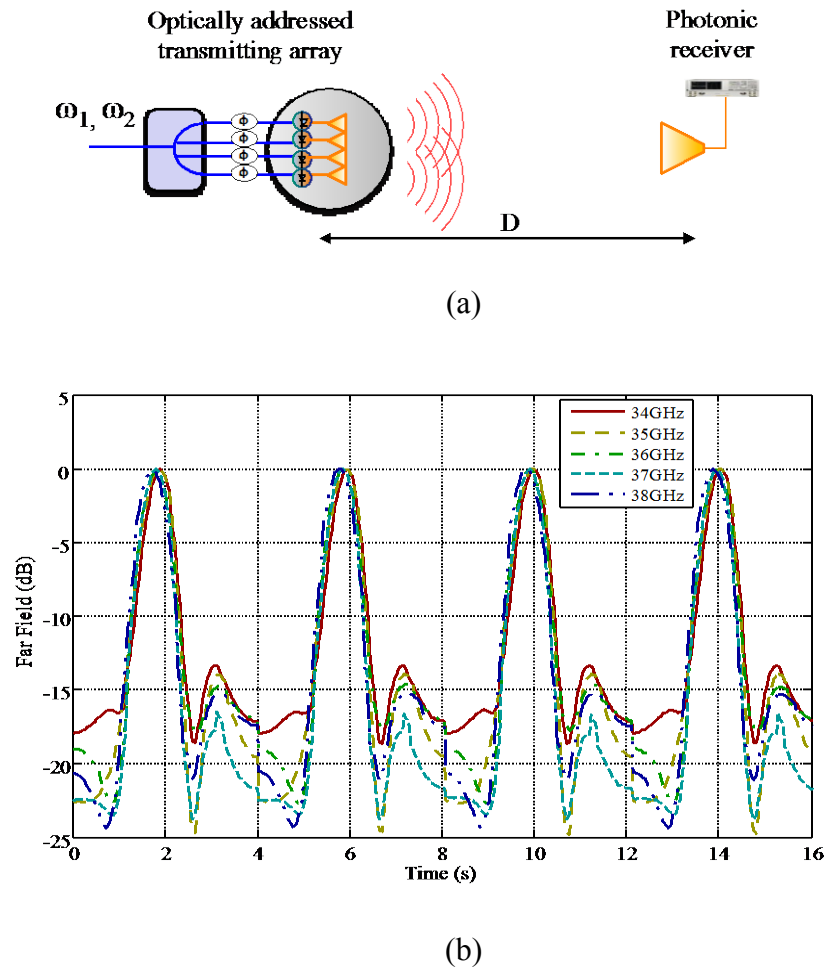
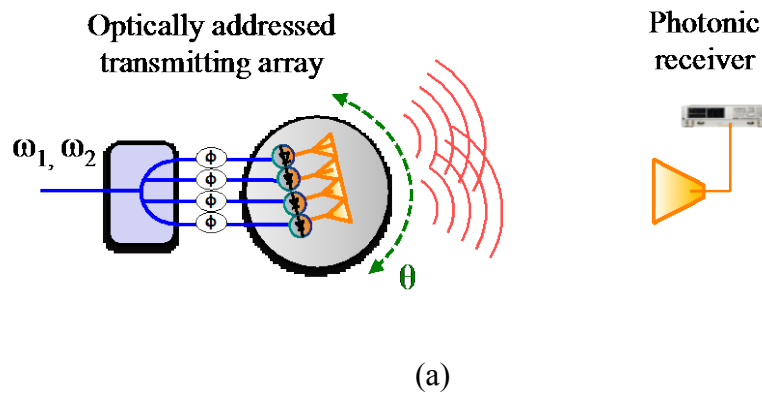
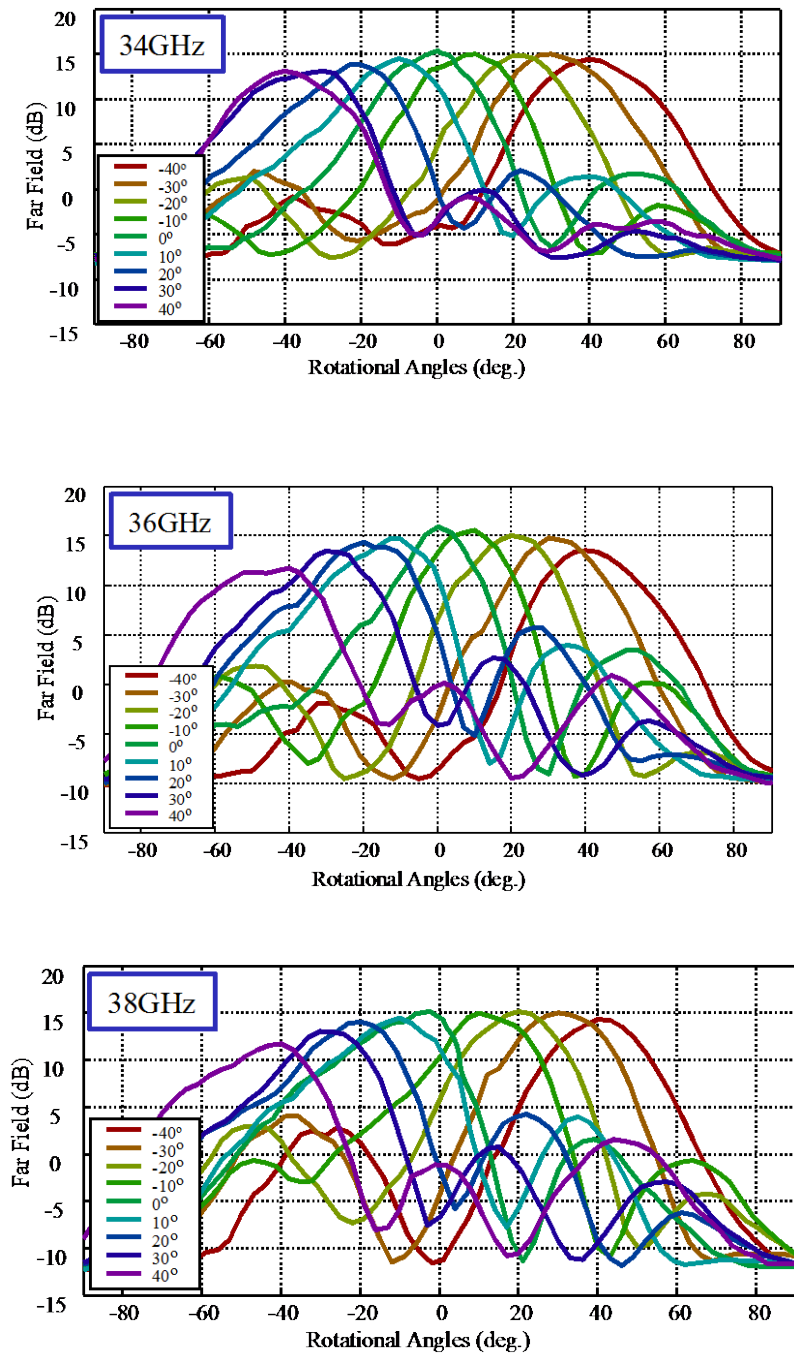


Figure 6.10 (a) Far-field measurement system, in which a progressive phase distribution is applied to the array elements to illustrate the beam scanning capability over an angular range from -90° to 90° . (b) Measured far-field pattern as a function of time over four repeating scans at different frequencies between 34 – 38GHz.

Figure 6.10 (b) shows four repeating electrical scans over a beam angle range swept from -90° to 90° . The integration time for each data point is set to be 40 ms and a total of 101 points with a beam steering step size of 1.8° are used for each scan. The peak far field corresponds to the broadside radiation of the phased array with equal phase distribution at all channels. Five different frequencies between 34 – 38 GHz are measured, all showing the maximum side lobes below -13 dB.

In order to further demonstrate the beam scanning capability, the system is improved by adding an additional rotational stage to measure the far-field radiation patterns of the developed phased array system. As shown in Figure 6.11 (a), a rotational stage is added to the RF beam steering setup, shown in Figure 6.10 (a), in which the transmitting array antenna can be scanned over -90° to $+90^\circ$. In so doing, we are able to physically measure the radiation pattern for a given beam steering. Nine electrical beam scans over a range of -40° to $+40^\circ$ with a step of 10° are conducted over the rotational angular range measured from the broadside of the transmitting array. Figure 6.11 (b) shows measured far fields at 34 GHz for all nine beams. From the figure, the peak positions of the steering beams are 10° apart. The maximum sidelobes are measured to be about -13 dB for all electrical beam steering. In addition, larger sidelobes may be observed at the larger steering angles due to the finite number of radiation elements and finite ground plane. The measured results are in good agreement with the simulation results over the active beam scanning range, as presented in Figure 6.9 (d).





(b)

Figure 6.11 (a) Far-field radiation pattern measurement setup for a given electrical beam steering direction. (b) Far-field radiation pattern measurements of the 4×4 phased array antenna with fixed phase assignment at each channels at different frequencies of 34, 36, and 38 GHz, respectively.

As discussed previously, the patch antenna is designed at Ka band, covering frequency band from 31 – 38 GHz. However, our photonic RF receiver has a limited operational bandwidth from 34 – 38 GHz, determined by the finite bandwidth of the low noise amplifier, which is 33.5 to 38 GHz. Figure 6.11 (b) shows the radiation patterns of the electrically steered beams at the frequencies of 36 and 38 GHz. Compared with 34 GHz, consistent results of electrical beam steering can be observed from the rotational measurement at all the frequencies.

The radiated RF power by the antenna is strongly dependent on the antenna, photodiode, and input powers of two optical signals, i.e., P_1 and P_2 . In order to produce sufficient RF radiation from the optically addressed phased array antenna, the conversion efficiency evaluated from optical-to-RF down-conversion plays a very important role. To this end, the conversion efficiency in the high-speed photodiode is defined as the ratio of the generated RF signal to the input power of the optical power, given by:

$$\eta = \frac{\left(\Re\sqrt{P_1P_2}\right)^2 Z}{P_1 + P_2} = \frac{\Re^2 P_1 P_2 Z}{P_1 + P_2} \quad (6.4)$$

in which $Z = 50$ Ohms is the impedance of the patch antenna. As we can see from the above equation, the conversion efficiency is proportional to the input optical power. In the case of evenly distributed power of the optical wavelengths before being fed into the photodiode, $P_1 = P_2 = P$, a maximum RF generated signal is achieved. The conversion efficiency is simplified to be $\eta = 0.5 \Re^2 PZ$. The u²t photodiode used in the array has responsivity of $\Re = 0.7$ A/W and maximum accepted input optical power of 13 dBm. The total RF power from each photodiode is 2.5 mW. The conversion

efficiency is then determined to be 12.5%. The efficiency can be further improved by using higher-power, high-speed photodiodes [65].

6.6 Experimental Demonstration: 1×4 Photodiode-Coupled TCA

6.6.1 Development of a 1×4 Photodiode-Coupled TCA

An 8×8 TCA dipole antenna fabricated on 20-mil Rogers 4350 with dielectric constant of 3.48 [84] employs the design as described in Section 4.3.4. This section is focused on its fabrication, integration, and measurement. The dipoles reside on the topside of the PCB, as shown in Figure 6.12 (a).

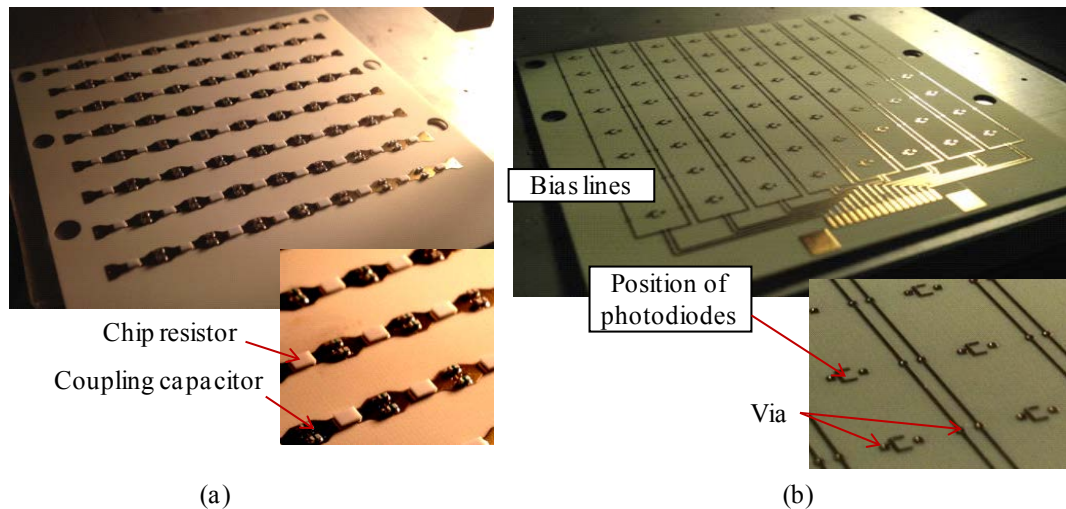


Figure 6.12 The developed 12-GHz TCA board. (a) The dipoles, 221-Ω chip resistors, and 0.1-μF wideband capacitors reside on the topside. (b) The bias network and photodiodes are on the backside.

To increase capacitive coupling, two 0.1-μF wideband (100 KHz – 40 GHz) capacitors are placed across the neighboring arms of two dipoles. As such, this TCA antenna is equivalent to a connected-dipole array. A 221-Ω chip resistor that can

operate up to 20 GHz is flip-chip bonded across the gap between the two arms of each dipole. As a result, the input resistance of the TCA antenna is decreased and thereby the operational bandwidth is increased. The bias network resides on the backside of the PCB as shown in Figure 6.12 (b). The photodiode position is marked as well. The bias lines use the narrowest wires allowed by fabrication technology in order to minimize the loading impact on each dipole. Meanwhile, the contacts of the bias lines are located at the center of dipole arms, wherein RF current is usually weaker than the other positions. In addition, the cross-polarization increases as the strength of RF current coupled into the bias lines. The bias lines set up this way can offer the cross-polarization more than 10 dB lower than the co-polarization.

6.6.2 Integration of Photodiodes with the TCA

This section will introduce a procedure of integrating photodiodes and optical fibers with the fabricated TCA antenna. The used photodiode, Albis PDCS24L, has G-S-G pads with a pitch of 50 μm . As the first step of the procedure, the photodiode is flip-chip bonded with a 4-mil ceramic substrate that has large bonding pads suitable for performing wire bonding. After that, an optical fiber is required to feed each photodiode that has been secured at a position on the TCA substrate illustrated in Figure 6.12 (b). To this end, a 900- μm single-mode (SM) optical fiber is threaded through a ceramic ferrule. After that, the optical fiber and ferrule are glued together, and then are carefully polished to ensure low transmission loss. Then, a piece of square quartz chip is attached to the polished ferrule, offering $4 \times 4 \text{ mm}^2$ contact area. Four pieces of $1 \times 1 \text{ mm}^2$ square quartz chips that acts as spacers are also glued around each corner of the photodiode. Next, the optical fiber is aligned with the photodiode on a *xyz* stage. The optimal alignment is achieved when the photocurrent is maximum

when an optical signal is incident into the photodiode. Lastly, the quartz chip attached to the ferrule is bonded with the spacer quartz chips. The above procedure is illustrated by Figure 6.13. In this way, a 1×4 array is integrated with four optical fibers, as shown in Figure 6.14. Table 6.1 lists measured photodiode responsivities.

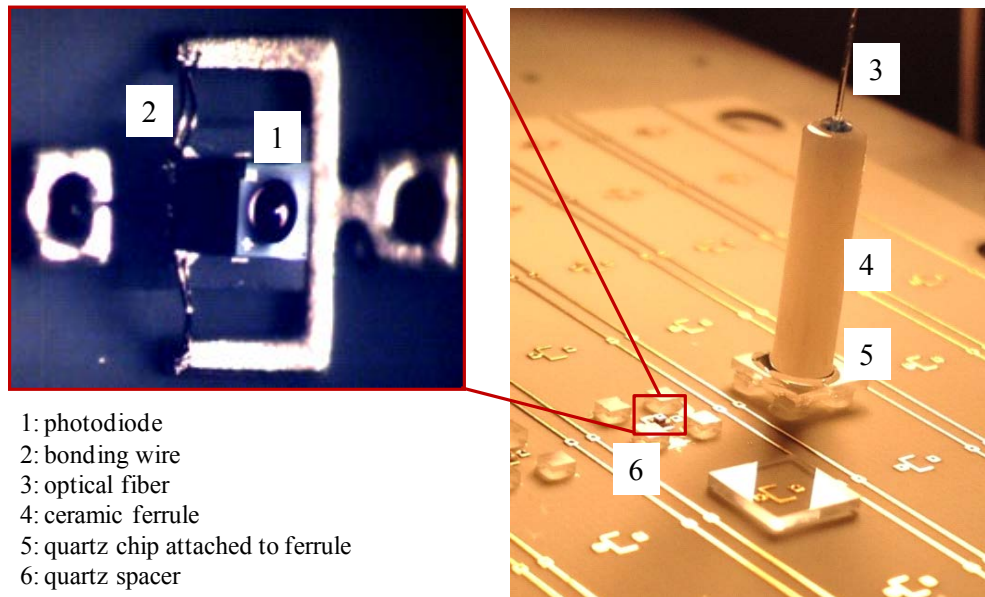


Figure 6.13 Integration procedure: (a) the photodiode is flip-chip bonded on the ceramic submount, (b) the photodiode is glued with the TCA substrate and is wire bonded with the antenna, (c) an optical fiber is glued with a ferrule and is polished, (d) a quartz chip is attached to the polished ferrule, (e) several quartz spacer are placed around the photodiode, (f) the optical fiber is aligned and bonded with the photodiode.

Table 6.1 Measured photodiode responsivities

Element	Responsivity
#1	0.35
#2	0.35
#3	0.39
#4	0.33

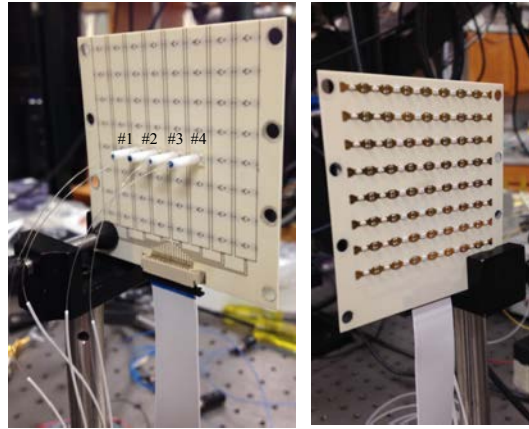


Figure 6.14 Fabricated 1×4 active antennas with integrated optical fibers.

6.6.3 Far-Field Measurement

The fabricated TCA under a test serving as a transmitter is fed by the developed four-channel optical feed network. An UWB double-ridge horn with a bandwidth of 4 – 40 GHz is used as a receiver. The measurement is performed in an in-house anechoic chamber, as shown in Figure 6.15.

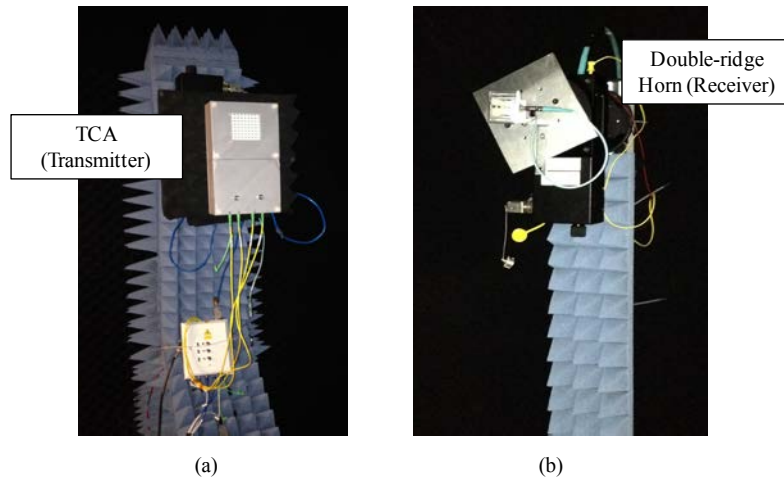


Figure 6.15 Far-field measurement in an anechoic chamber. (a) TCA under test as a transmitter, (b) double-ridge horn as a receiver.

The radiation power of each dipole is measured individually. The broadside and maximum radiation power at different frequencies are measured, as shown in Figure 6.16. It is observed from the figure that the radiation power of #1 and #2 dipole are equal to that of #3 and #4 dipole, respectively, due to their symmetric locations. In addition, at frequencies lower than 8 GHz, the radiation power of the inner dipoles (#2 and #3) are higher than those of the outer dipoles (#1 and #4) by about 3 dB, probably because of the additional loss incurred by the resistors loaded on the dummy element.

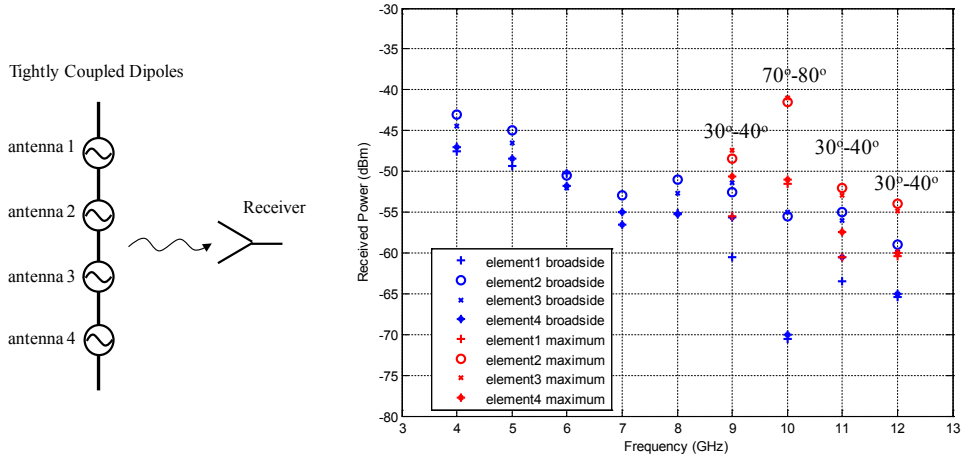


Figure 6.16 The received radiation power of each element excited individually at a time. The maximum power is off the broadside particularly at the high frequencies.

Furthermore, the maximum radiation power is not at the broadside, particularly notable at the high frequencies. This phenomenon can be understood as follows. At the high frequencies, the connected dipoles behave as a long-wire antenna that can have maximum gains off the broadside. This offset is not obvious at the low frequencies since the array has low gains and wide beamwidths. The measurement implies that each dipole has different radiation patterns. In comparison, the radiation patterns of a

loosely coupled array can be synthesized by the multiplication of single antenna pattern with an array factor. However, the similar method cannot apply to a tightly coupled array. The radiation patterns of the fabricated array is obtained by full-wave simulations and measurements.

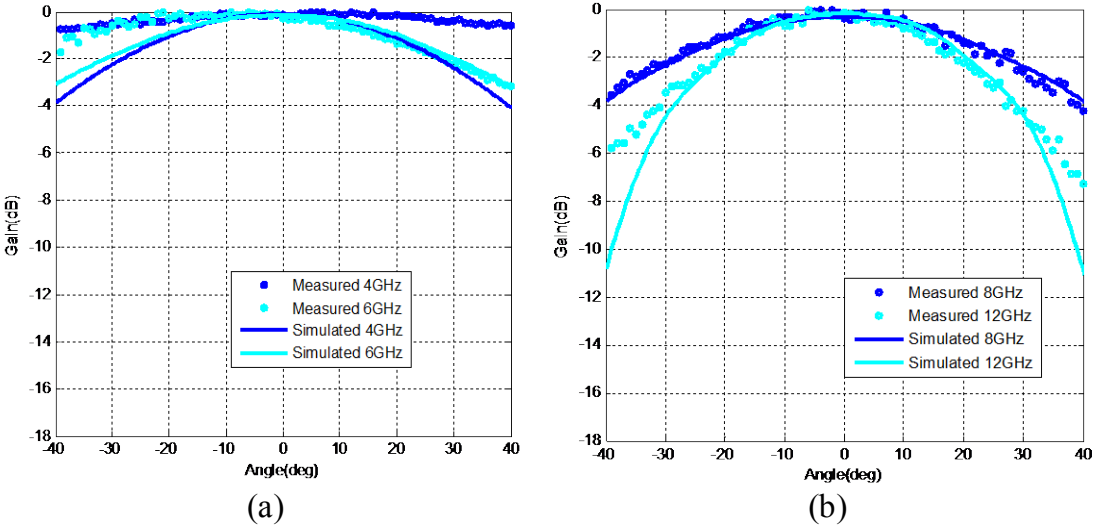


Figure 6.17 The measured versus the simulated radiation patterns: (a) 4 GHz and 6 GHz, and (b) 10 GHz and 12 GHz.

Figure 6.17 shows the measured and simulated radiation patterns at the frequency of 4 GHz, 6 GHz, 10 GHz, and 12 GHz, respectively. It is observed that the measurements are in a good agreement with the simulations at 10 GHz and 12 GHz. However, the measured radiation beams are wider than the simulated at 4 GHz and 6 GHz. This discrepancy might be attributed from the measurements that are performed close to anechoic chamber's cutoff frequency of 4 GHz. In addition, beam steering is demonstrated as shown in Figure 6.18. Since the array has quite low gains at the low

frequencies, the beam steering will be not notable. Hence, the beam steering is only plotted at 12 GHz, which demonstrates more than a 40-degree beam scanning.

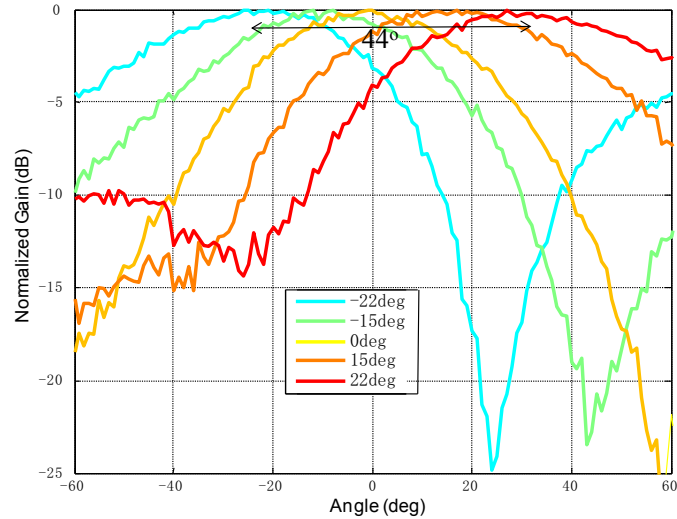


Figure 6.18 Measured beam scanning at the frequency of 12 GHz.

6.6.4 Near-Field Measurement

The frequency response of the radiation power will be analyzed in this section. The analysis needs to obtain total radiation powers at different frequencies. To this end, radiation patterns are required to be measured and integrated over the a large space range, which however cannot be performed based on current instrument capabilities. Instead, the frequency response of the radiation power can be estimated by near-field scanning patterns, since total radiation power should preserve from the near field to the far field. To perform the near-field measurement, the receiver and transmitter are separated with the distance of 14 inches. The radiation pattern as shown in Figure 6.19 is produced by sweeping the phase of the EO phase modulator in each channel. The near-field radiation pattern, compared with the far-field pattern, is

narrower, which implies the radiation power is mostly confined in a smaller volume. The measured power as demonstrated in the figure is after calibrating cable losses and receiver gains.

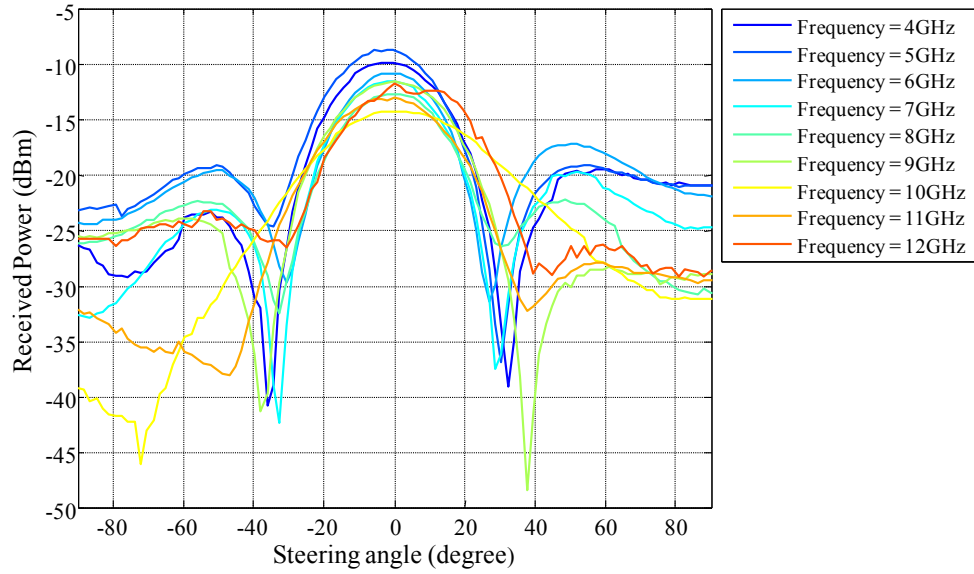


Figure 6.19 Near-field scanning patterns at the frequencies of 4 –12 GHz.

Since the antenna array is rotationally symmetric, the total radiation power can be approximated by integrating the measured power over entire space angles:

$$P_r(\omega) \approx 2\pi R \int_{-\pi/2}^{\pi/2} p_r(\theta, \omega) d\theta \quad (6.5)$$

in which p_r is the measured radiation power at a specific angle and R is the distance between the transmitter and receiver. By doing this, the frequency response is obtained as shown in Figure 6.20. It is noted from the figure that the bandwidth of the power variation less than 3 dB is from 4 to 12 GHz.

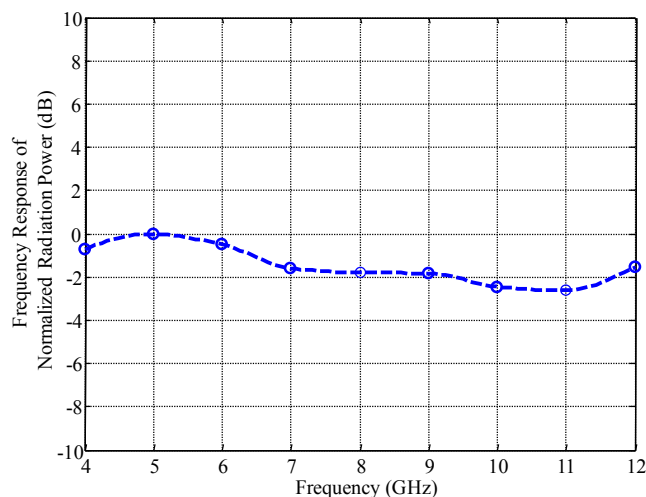


Figure 6.20 Normalized radiation power of the TCA versus frequencies.

6.7 Summary

A novel optically addressed phased array transmitter architecture is proposed and a prototype system is demonstrated. The system is mainly comprised of a photonic RF source, an optical phased feed network, and an active RF aperture in addition to an electronic control. The experiment results have demonstrated that the operational ultra-wide bandwidth as well as the beam steering.

The system bandwidth of the proposed architecture is primarily restricted by the RF aperture. To obtain an ultra-wideband RF aperture, the fabrication and integration of a photodiode-coupled TCA are explored. In the demonstration, a 1×4 connected-dipole array is integrated with photodiodes and optical fibers, which offers the 3-dB radiation bandwidth of more than 4 – 12 GHz.

Chapter 7

CONCLUSIONS AND FUTURE WORK

7.1 Summary and Conclusions

UWB phased arrays, as an alternative to narrow band technology, will be utilized in multifunctional systems. RF photonics technology has drawn considerable attention because of its advantage over traditional systems, including extreme power efficiency, information capacity, frequency agility, and spatial beam diversity. A hybrid RF photonics system, utilizing optical links and a RF transducer at the antenna, can potentially provide ultra-high bandwidth data transmission.

This dissertation was primarily focused on the construction of an optically addressed ultra-wideband phased array transmitter using RF photonic technology. A novel phased array transmitter architecture was developed, which leverages an ultra-wideband photonic RF source with a demonstrated tuning range of 110 GHz. Multiple novel techniques were demonstrated to attain a compact UWB antenna including loaded Vivaldi antennas, the D-ring resonator antenna, and the photodiode-coupled TCA antenna. An optical feed network, which distributes two-tone coherent optical signals for mixing in the frontend of an active RF aperture with low phase noise via orthogonal polarizations of an optical fiber, was established. Beam steering was also demonstrated within that feed network using electro-optic (EO) phase modulators. Finally, these components are brought together to demonstrate an optically addressed phased array transmitter architecture, which offers low transmission losses, low phase

noise, a light weight and flexible distribution network, a conformal structure, ultra-wideband operation, easy implementation, and large scalability.

In Chapter 1, the state-of-the-art UWB phased array technologies and compared their bandwidth and other performance metrics. In addition, the advantage of an optical approach was discussed and a novel optically addressed phased array architecture was proposed.

In Chapter 2, two different loading structures were introduced, a circular-shape-load and a slot-load, that yielded compact Vivaldi antennas with ultra-wide bandwidths of more than 46 GHz.

In Chapter 3, a wideband, electrically small, planar, coupled D-ring resonator antenna, driven by an interdigital monopole with an embedded matching network, was presented. This electrically small antenna achieved an impedance-matched bandwidth of 1 – 1.7 GHz, attributable to its dual-mode operation.

In Chapter 4, the operating principle of an optically fed TCA was explained in detail. In addition, an optically fed TCA with an operational bandwidth of 1 – 12 GHz was designed and simulated.

In Chapter 5, a novel optical feed network was demonstrated, which distributes a two-tone coherent optical signal for mixing in the frontend of an active RF aperture with low phase noise via orthogonal polarizations of an optical fiber. Beam steering was also demonstrated using electro-optic (EO) phase modulators. In addition, the excess phase noise introduced by the misaligned polarization states of the optical signal and EO modulator were overcome using a polarization controller and a DC feedback signal generated by the photodiodes.

Finally, in Chapter 6, an optically addressed phased array transmitter prototype was fabricated and each block in the system was described. The radiation pattern, beam steering range, and operational bandwidth of the prototype were measured and compared with simulation.

7.2 Future Work

In this dissertation an optically fed TCA transmitting antenna, which is comprised of four active elements with an operational frequency up to 12 GHz, was demonstrated. In the future, a fully populated TCA antenna, with 8×8 active elements, should be pursued in order to increase the operational bandwidth (from 4-12 GHz to 4 – 60 GHz) as well as the output power. It was also shown that the edge-truncation effect in a finite array has a significant impact on the performance. Further study is necessary to optimize the design of a finite TCA.

Furthermore, the migration of the TCA operating frequency to the mm-wave regime requires the development of photodiode-antenna coupling circuitry with a small parasitic reactance. The radiation efficiency can also be increased by adding a ground plane. In addition, a chip-scale optical feed network on LiNbO_3 is desired in order to further improve the phase stability. Lastly, optical true-time delay lines are an essential component required by a large-scale optical addressed phased array and additional development is called for in order to realize large delay times and low insertion losses.

REFERENCES

- [1] D. W. Corman, P. Moosbrugger, and G. M. Rebeiz, "The Industry's Next Tipping Point," *Microwave Journal*, vol.57, no. 5, pp. 26–38, 2014.
- [2] P. J. Callus, "Conformal load-bearing antenna structure for Australian Defence Force aircraft," 2007.
- [3] G. J. Schneider, J. A. Murakowski, C. A. Schuetz, S. Shi, and D. W. Prather, "Radiofrequency signal-generation system with over seven octaves of continuous tuning," *Nature Photonics*, vol. 7, no. 2, pp. 118–122, 2013.
- [4] J. J. Lee, R. Y. Loo, S. Livingston, V. I. Jones, J. B. Lewis, H. Yen, G. L. Tansonan, and M. Wechsberg, "Photonic wideband array antennas," *IEEE Transactions on Antennas and Propagation*, , vol. 43, no. 9, pp. 966–982, 1995.
- [5] C. Hemmi, R. T. Dover, F. German, and A. Vespa, "Multifunction wide-band array design," , *IEEE Transactions on Antennas and Propagation*, vol. 47, no. 3, pp. 425–431, 1999.
- [6] H. Holter, T.-H. Chio, and D. H. Schaubert, "Experimental results of 144-element dual-polarized endfire tapered-slot phased arrays," *IEEE Transactions on Antennas and Propagation*, vol. 48, no. 11, pp. 1707–1718, 2000.
- [7] J. J. Lee, S. Livingston, and R. Koenig, "A low-profile wide-band (5:1) dual-pol array," *IEEE Antennas and Wireless Propagation Letters*, vol. 2, no. 1, pp. 46–49, 2003.
- [8] J. J. Lee, S. Livingston, and R. Koenig, "Performance of a wideband (3-14 GHz) dual-pol array," in *Antennas and Propagation Society International Symposium, 2004. IEEE*, 2004, vol. 1, pp. 551–554.
- [9] J. J. Lee, S. Livingston, R. Koenig, D. Nagata, and L. L. Lai, "Compact Light Weight UHF Arrays Using Long Slot Apertures," *IEEE Transactions on Antennas and Propagation*, vol. 54, no. 7, pp. 2009–2015, Jul. 2006.
- [10] M. Jones and J. Rawnick, "A new approach to broadband array design using tightly coupled elements," in *Military Communications Conference, 2007. MILCOM 2007. IEEE*, 2007, pp. 1–7.

- [11] R. W. Kindt and W. R. Pickles, "All-Metal Flared-Notch Array Radiator for Ultrawideband Applications," DTIC Document, 2010.
- [12] J. G. Maloney, B. N. Baker, R. T. Lee, G. N. Kiesel, and J. J. Acree, "Wide scan, integrated printed circuit board, fragmented aperture array antennas," in *Antennas and Propagation (APSURSI), 2011 IEEE International Symposium on*, 2011, pp. 1965–1968.
- [13] W. F. Moulder, K. Sertel, and J. L. Volakis, "Superstrate-enhanced ultrawideband tightly coupled array with resistive FSS," *IEEE Transactions on Antennas and Propagation*, vol. 60, no. 9, pp. 4166–4172, Sep. 2012.
- [14] S. S. Holland, D. H. Schaubert, and M. N. Vouvakis, "A 7 – 21 GHz dual-polarized planar ultrawideband modular antenna (PUMA) array," *IEEE Transactions on Antennas and Propagation*, vol. 60, no. 10, pp. 4589–4600, Oct. 2012.
- [15] I. Tzanidis, K. Sertel, and J. L. Volakis, "Interwoven spiral array (ISPA) with a 10:1 bandwidth on a ground plane," *IEEE Antennas and Wireless Propagation Letters*, vol. 10, pp. 115–118, 2011.
- [16] J. A. Kasemodel, C.-C. Chen, and J. L. Volakis, "Wideband planar array with integrated feed and matching network for wide-angle scanning," *IEEE Transactions on Antennas and Propagation*, vol. 61, no. 9, pp. 4528–4537, Sep. 2013.
- [17] A. Neto and J. J. Lee, "“Infinite bandwidth” long slot array antenna," *IEEE Antennas and Wireless Propagation Letters*, vol. 4, no. 1, pp. 75–78, Dec. 2005.
- [18] P. J. Gibson, "The vivaldi aerial," in *Microwave Conference, 1979. 9th European*, 1979, pp. 101–105.
- [19] S. Sugawara, Y. Maita, K. Adachi, K. Mori, and K. Mizuno, "A mm-wave tapered slot antenna with improved radiation pattern," in *Microwave Symposium Digest, 1997., IEEE MTT-S International*, 1997, vol. 2, pp. 959–962.
- [20] E. Gazit, "Improved design of the Vivaldi antenna," in *Microwaves, Antennas and Propagation, IEE Proceedings*, 1988, vol. 135, pp. 89–92.
- [21] J. D. S. Langley, P. S. Hall, and P. Newham, "Balanced antipodal Vivaldi antenna for wide bandwidth phased arrays," in *Microwaves, Antennas and Propagation, IEE Proceedings*, 1996, vol. 143, pp. 97–102.

- [22] K. S. Yngvesson, T. L. Korzeniowski, Y.-S. Kim, E. L. Kollberg, and J. F. Johansson, "The tapered slot antenna-a new integrated element for millimeter-wave applications," *IEEE Transactions on Microwave Theory and Techniques*, vol. 37, no. 2, pp. 365–374, 1989.
- [23] K. S. Yngvesson, "Endfire tapered slot antennas on dielectric substrates," *IEEE Transactions on Antennas and Propagation*, vol. 33, no. 12, pp. 1392–1400, 1985.
- [24] J. Bai, S. Shi, D. W. Prather, "A Modified Antipodal Vivaldi Antenna with Improved Bandwidth and Radiation Pattern," *Abstract, Progress In Electromagnetics Research Symposium, Cambridge, 2010*.
- [25] E. Gullanton, J. Y. Dauvignac, C. Pichot, J. Cashman, "A new design tapered slot antenna for ultra-wideband applications," *Microwave Optical Technology Letters*, vol. 19, no. 4, pp. 286-289, 1998.
- [26] H. Oraizi, S. Jam, "Optimum design of tapered slot antenna profile," *IEEE Transactions on Antennas and Propagation*, vol. 51, no. 8, pp. 1987-1995, 2003.
- [27] A. Z. Hood, T. Karacolak, E. Topsakal, "A small antipodal Vivaldi antenna for ultrawide-band applications," *IEEE Antennas Wireless and Propagation Letter*, vol. 7, pp. 656-660, 2008.
- [28] J. Bai, S. Shi, and D. W. Prather, "Modified compact antipodal Vivaldi antenna for 4-50-GHz UWB application," *IEEE Transactions on Microwave Theory and Techniques*, vol. 59, no. 4, pp. 1051–1057, Apr. 2011.
- [29] H. Loui, J. P. Weem, Z. Popovic, "A dual-band dual-polarized nested Vivaldi slot array with multilevel ground Plane," *IEEE Transactions on Antennas and Propagation*, vol. 51, no. 9, pp. 2168-2175, 2003.
- [30] J. B. Rizk, G. M. Rebeiz, "Millimeter-wave Fermi tapered slot antennas on micromachined silicon substrates," *IEEE Transactions on Antennas and Propagation*, vol. 50, no. 3, pp. 379-383, 2002.
- [31] H. Y. Xu, H. Zhang, J. Wang, L. X. Ma, "A new tapered slot antenna with symmetrical and stable radiation pattern," *Progress In Electromagnetics Research Letters*, Vol. 5, pp. 35-43, 2008.
- [32] S. Sugawara, Y. Maita, K. Adachi, K. Mori, and K. Mizuno, "Characteristics of a mm-wave tapered slot antenna with corrugated edges," in *Microwave Symposium Digest, 1998 IEEE MTT-S International*, 1998, vol. 2, pp. 533–536.

- [33] J. Bai, S. Shi, and D. W. Prather, "Ultra-wideband slot-load antipodal Vivaldi antenna array," in *Antennas and Propagation (APSURSI), 2011 IEEE International Symposium on*, pp. 79–81, 2011.
- [34] K. Buell, H. Mosallaei, and K. Sarabandi, "A substrate for small patch antennas providing tunable miniaturization factors," *IEEE Transactions on Microwave Theory and Techniques*, vol. 54, pp. 135-146, 2006.
- [35] K. Buell, H. Mosallaei, and K. Sarabandi, "A substrate for small patch antennas providing tunable miniaturization factors," *IEEE Trans on Microw. Theory and Tech.*, vol. 54, pp. 135-146, 2006.
- [36] F. Bilotti, A. Alu', and L. Vegni, "Design of miniaturized metamaterial patch antennas with μ -negative loading," *IEEE Transactions on Antennas and Propagation*, vol. 56, no. 6, pp. 1640–1647, 2008.
- [37] G. Mumcu, K. Sertel, and J. L. Volakis, "Miniature antenna using printed coupled lines emulating degenerate band edge crystals," *IEEE Transactions on Antennas and Propagation*, vol. 57, no. 6, pp. 1618–1624, 2009.
- [38] M. A. Antoniadou and G. V. Eleftheriades, "A folded-monopole model for electrically small NRI-TL metamaterial antennas," *IEEE Antennas and Wireless Propagation Letter*, vol. 7, pp. 425–428, 2008.
- [39] A. Lai, K. M. K. H. Leong, and T. Itoh, "Infinite wavelength resonant antennas with monopolar radiation pattern based on periodic structure," *IEEE Transactions on Antennas and Propagation*, vol. 55, no. 3, pp. 868–876, 2007.
- [40] J.-H. Park, Y.-H. Ryu, J.-G. Lee, and J.-H. Lee, "Epsilon negative zeroth-order resonator antenna," *IEEE Transactions on Antennas and Propagation*, vol. 55, no. 12, pp. 3710–3712, 2007.
- [41] J. Park, Y. Ryu, and J. Lee, "Mu-zero resonance antenna," *IEEE Transactions on Antennas and Propagation*, vol. 58, no. 6, pp. 1865–1875, 2010.
- [42] M. Selvanayagam, G. V. Eleftheriades, "A compact printed antenna with an embedded double-tuned metamaterial matching network," *IEEE Transactions on Antennas and Propagation*, vol. 58, no. 7, pp. 2354–2361, 2010.
- [43] A. Erentok and R. W. Ziolkowski, "Metamaterial-inspired efficient electrically small antennas," *IEEE Transactions on Antennas and Propagation*, vol. 56, no. 3, pp. 691–707, 2008.

- [44] R. W. Ziolkowski, "Efficient electrically small antenna facilitated by a near-field resonant parasitic," *IEEE Antennas and Wireless Propagation Letter*, vol. 7, pp. 580–583, 2008.
- [45] O. S. Kim and O. Breinbjerg, "Miniaturized self-resonant split-ring resonator antenna," *Electronic Letter*, vol. 45, pp. 196–197, 2009.
- [46] J. Herraiz-Martnez, L. E. Garca-Muoz, D. Gonzlez-Ovejero, V. Gonzlez-Posadas, and D. Segovia-Vargas, "Dual-frequency printed dipole loaded with split ring resonators," *IEEE Antenna and Wireless Propagation Letter*, vol. 8, pp. 137–140, 2009.
- [47] M. A. Antoniadis and G. V. Eleftheriades, "A broadband dual-mode monopole antenna using nri-tl metamaterial loading," *IEEE Antenna and Wireless Propagation Letter*, vol. 8, pp. 258–261, 2009.
- [48] J. Zhu, M. A. Antoniadis, and G. V. Eleftheriades, "A compact tri-band monopole antenna with single-cell metamaterial loading," *IEEE Transaction on Antennas and Propagation*, vol. 58, no. 4, pp. 1031–1038, 2010.
- [49] P. Jin and R. W. Ziolkowski, "Multi-frequency, linear and circular polarized, metamaterial-inspired near-field resonant parasitic antennas," *IEEE Transactions on Antennas and Propagation*, vol. 59, no. 5, pp. 1446–1459, 2011.
- [50] C. C. Lin, P. Jin, and R. W. Ziolkowski, "Electrically small dual-band and circularly polarized magnetically-coupled near-field resonant parasitic wire antennas," *IEEE Transactions on Antennas and Propagation*, vol. 59, no. 3, pp. 714–724, 2011.
- [51] P. Jin and R. W. Ziolkowski, "Broadband, efficient, electrically small metamaterial-inspired antennas facilitated by active near-field resonant parasitic elements," *IEEE Transactions on Antennas and Propagation*, vol. 58, no. 2, pp. 318–327, 2010.
- [52] H. R. Stuart and C. Tran, "Subwavelength microwave resonators exhibiting strong coupling to radiation modes," *Applied Physics Letter*, vol. 87, 151108, 2005.
- [53] J. Bai, S. Shi, J. P. Wilson, R. Nelson, and D. W. Prather, "Wideband, electrically small, planar, coupled subwavelength resonator antenna with an embedded matching network," *IEEE Transactions on Antennas and Propagation*, vol. 61, no. 5, pp. 2388–2396, 2013.

- [54] L. J. Chu, "Physical limitations of omni-directional antennas," *Journal of Applied Physics*, vol. 19, pp. 1163-1175, 1948.
- [55] A. D. Yaghjian and S. R. Best, "Impedance, bandwidth, and Q of antennas," *IEEE Transactions on Antennas and Propagation*, vol. 53, no. 4, pp. 1298-1324, 2005.
- [56] B. Munk, *Frequency Selective Surfaces, Theory and Design*, New York: Wiley, 2000.
- [57] D. F. Sievenpiper, *et.al.*, "Experimental validation of performance limits and design guidelines for small antennas," *IEEE Transactions on Antennas Propagation*, vol. 60, no. 1, pp. 8-19, 2012.
- [58] J. Oh, K. Sarabandi, "Low profile, miniaturized, inductively coupled capacitively loaded monopole antenna," *IEEE Transactions on Antennas and Propagation*, vol. 60, no. 3, pp. 1206-1213, 2012.
- [59] J. Zhu and G. V. Eleftheriades, "A compact transmission-line metamaterial antenna with extended bandwidth," *IEEE Antenna and Wireless Propagation Letter*, vol. 8, pp. 295-298, 2009.
- [60] H. A. Wheeler, "Simple relation derived from a phased-array antenna made of an infinite current sheet," *IEEE Transactions on Antennas Propagation*, vol. 13, no. 4, pp. 506-514, 1965.
- [61] I. Tzanidis, K. Sertel, and J. L. Volakis, "UWB low-profile tightly coupled dipole array with integrated balun and edge terminations," *IEEE Transactions on Antennas and Propagation*, vol. 61, no. 6, pp. 3017-3025, 2013.
- [62] Tengfei Xia, Shiwen Yang, and Zaiping Nie, "Design of a Tapered Balun for Broadband Arrays With Closely Spaced Elements," *IEEE Antennas and Wireless Propagation Letters*, vol. 8, pp. 1291-1294, 2009.
- [63] S. S. Holland and M. N. Vouvakis, "The planar ultrawideband modular antenna (PUMA) array," *IEEE Transactions on Antennas and Propagation*, vol. 60, no. 1, pp. 130-140, Jan. 2012.
- [64] J.-P. Bayard, D. H. Schaubert, and M. E. Cooley, "E-plane scan performance of infinite arrays of dipoles printed on protruding dielectric substrates: coplanar feed line and E-plane metallic wall effects," *IEEE Transactions on Antennas and Propagation*, vol. 41, no. 6, pp. 837-841, 1993.

- [65] Xin Wang, Ning Duan, Hao Chen, and J. C. Campbell, "InGaAs-InP photodiodes with high responsivity and high saturation power," *IEEE Photonics Technology Letters*, vol. 19, no. 16, pp. 1272–1274, Aug. 2007.
- [66] D. M. Pozar, *Microwave Engineering*, New York: Wiley, 2011.
- [67] [Online] <http://www.albisopto.com/>
- [68] S. Shi, J. Bai, G. Schneider, and D. Prather, "Optical phase feed network and ultra-wideband phased array," in *Photonics Conference (IPC), 2012 IEEE*, pp. 372–373, 2012.
- [69] J. Bai, S. Shi, G. J. Schneider, J. P. Wilson, Y. Zhang, W. Pan, and D. W. Prather, "Optically driven ultrawideband phased array with an optical interleaving feed network," *IEEE Antennas and Wireless Propagation Letters*, vol. 13, pp. 47–50, 2014.
- [70] J. Macario, P. Yao, S. Shi, A. Zablock, C. E. Harrity, R. Martin, C. Scheutz, and D. W. Prather, "Full spectrum millimeter-wave modulation," *Optics Express*, vol. 20, no. 21, p. 23623, 2012.
- [71] T. Musha, J. Kamimura, and M. Nakazawa, "Optical phase fluctuations thermally induced in a single-mode optical fiber," *Applied Optics*, vol. 21, no. 4, pp. 694–698, 1982.
- [72] [Online] <http://www.thorlabs.com/>
- [73] A. J. Seeds and K. J. Williams, "Microwave photonics," *IEEE/OSA Journal of Lightwave Technology*, vol. 24, no. 12, pp. 4628–4641, 2006.
- [74] S.C. Chang, *RF photonic technology in optical fiber links*, Cambridge, 2002.
- [75] J. Yao, "Microwave photonics," *IEEE/OSA Journal of Lightwave Technology*, vol. 27, no. 3, pp. 314–335, Feb. 2009.
- [76] T. R. Clark and M. L. Dennis, "Coherent optical phase-modulation link," *IEEE Photonics Technology Letter*, vol. 19, no. 16, pp. 1206–1208, Aug. 2007.
- [77] B. M. Haas and T. E. Murphy, "Linearized downconverting microwave photonic link using dual-wavelength phase modulation and optical filtering," *IEEE Photonics Journal*, vol. 3, no. 1, pp. 1–12, 2011.
- [78] C. A. Schuetz, J. Murakowski, G. J. Schneider, and D. W. Prather, "Radiometric millimeter-wave detection via optical upconversion and carrier suppression,"

IEEE Transactions Microwave Theory and Techniques, vol. 53, no. 5, pp. 1732–1738, 2005.

- [79] C. Schuetz and D. W. Prather, “Optical upconversion techniques for high-sensitivity millimetre-wave detection,” *SPIE*, vol. 5619, pp. 166–174, 2004.
- [80] J. P. Wilson, C. A. Schuetz, T. E. Dillon, P. Yao, C. E. Harrity, and D. W. Prather, “Passive 77 GHz millimeter-wave sensor based on optical upconversion,” *Applied Optics*, vol. 51, no. 18, pp. 4157–4167, 2012.
- [81] Lee Stein, “Design and development of passive millimeterwave imaging systems,” *Master Thesis, University of Delaware, 2009*.
- [82] Y. Zhang, J. Bai, S. Shi, and D. W. Prather, “Ka-band phased patch antenna array,” in *Antennas and Propagation (APSURSI), 2012 IEEE International Symposium on*, Jul. 2012.
- [83] P. Sullivan and D. Schaubert, “Analysis of an aperture coupled microstrip antenna,” *IEEE Transactions on Antennas and Propagation*, vol. 34, no. 8, pp. 977–984, 1986.
- [84] J. Bai, S. Shi, G. Schneider, and D. W. Prather, “All-optical ultra-wideband tightly coupled phased antenna array,” *Antennas and Propagation (APSURSI), 2014 IEEE International Symposium on*, Jul. 2014.

Appendix

LIST OF PUBLICATIONS

Journal Publications

S. Shi, **J. Bai**, G. Schneider, Y. Zhang, R. Nelson, J. Wilson, C. Schuetz, and D. Prather, “Conformal wideband optically addressed transmitting phased array with photonic receiver,” accepted for publication in *IEEE/OSA Journal of Lightwave Technology*, Sept, 2014.

J. Bai, S. Shi, G. J. Schneider, J. P. Wilson, Y. Zhang, W. Pan, and D. W. Prather, “Optically driven ultrawideband phased array with an optical interleaving feed network,” *IEEE Antennas and Wireless Propagation Letters*, vol. 13, pp. 47–50, 2014.

J. Bai, S. Shi, J. P. Wilson, R. Nelson, and D. W. Prather, “Wideband, electrically small, planar, coupled subwavelength resonator antenna with an embedded matching network,” *IEEE Transactions on Antennas and Propagation*, vol. 61, no. 5, pp. 2388–2396, 2013.

J. Bai, S. Shi, and D. W. Prather, “Modified compact antipodal Vivaldi antenna for 4-50-GHz UWB application,” *IEEE Transactions on Microwave Theory and Techniques*, vol. 59, no. 4, pp. 1051–1057, Apr. 2011.

J. Bai, S. Shi, and D. W. Prather, “Analysis of epsilon-near-zero metamaterial super-tunneling using cascaded ultra-narrow waveguide channels,” *Progress In Electromagnetics Research M*, vol. 14, pp. 113–121, 2010.

Conference Publications

J. Bai, S. Shi, G. Schneider, and D. W. Prather, “All-optical ultra-wideband tightly coupled phased antenna array,” accepted for publication in *Antennas and Propagation Society International Symposium (APSURSI)*, 2014.

S. Shi, **J. Bai**, G. Schneider, Y. Zhang, and D. Prather, “Ultra-wideband optically addressed transmitting phased array,” in *Antennas and Propagation Society International Symposium (APSURSI), 2013 IEEE*, pp. 2237–2238, 2013.

S. Shi, **J. Bai**, G. Schneider, Y. Zhang, R. Nelson, J. Wilson, C. Schuetz, and D. Prather, “Conformal ultra-wideband optically addressed transmitting phased array and photonic receiver systems,” in *Microwave Photonics (MWP), 2013 International Topical Meeting on*, pp. 221–224, 2013.

J. Bai, S. Shi, and D. W. Prather, “Photodiode-coupled active metamaterial antenna with boosted radiation efficiency,” in *Antennas and Propagation Society International Symposium (APSURSI), 2013 IEEE*, pp. 1276–1277, 2013.

J. Bai, S. Shi, G. Schneider, and D. W. Prather, “Optically driven ultra-wideband phased array with a novel optical feed network,” in *Microwave Symposium Digest (IMS), 2013 IEEE MTT-S International*, pp. 1–3, 2013.

S. Shi, **J. Bai**, G. Schneider, and D. Prather, “Optical phase feed network and ultra-wideband phased array,” in *Photonics Conference (IPC), 2012 IEEE*, pp. 372–373, 2012.

J. Bai, S. Shi, G. Schneider, and D. Prather, “Development of optical-RF transmitter modules for an optically addressed 2-40-GHz phased array,” in *Photonics Conference (IPC), 2012 IEEE*, pp. 376–377, 2012.

Y. Zhang, **J. Bai**, S. Shi, and D. W. Prather, “Ka-band phased patch antenna array,” in *Antennas and Propagation Society International Symposium (APSURSI), 2012 IEEE*, pp. 1–2, 2012.

J. Bai, S. Shi, D. W. Prather, and R. Nelson, “Wideband, electrically small, planar, coupled subwavelength resonator antenna with an embedded matching network,” in *Antennas and Propagation Society International Symposium (APSURSI), 2012 IEEE*, pp. 1–2, 2012.

J. Bai, S. Shi, and D. W. Prather, “Ultra-wideband slot-load antipodal Vivaldi antenna array,” in *Antennas and Propagation Society International Symposium (APSURSI), 2011 IEEE*, pp. 79–81, 2011.